National Aeronautics and Space Administration

A Heliophysics Solar Terrestrial Probes-class Mission Concept Study for the
2024-2033 Solar and Space Physics Decadal Survey

COMPASS

Comprehensive Observations of Magnetospheric Particle Acceleration, Sources, and Sinks

First Dedicated Radiation Belt Mission
to Explore the Extremes of Jupiter's Magnetosphere

George Clark
Principal Investigator
Johns Hopkins Applied Physics Laboratory
george.clark@jhuapl.edu

Jim Kinnison & Dan Kelly
Design Study Leads
Johns Hopkins Applied Physics Laboratory
jim.kinnison@jhuapl.edu / daniel.kelly@jhuapl.edu

APL JOHNS HOPKINS
APPLIED PHYSICS LABORATORY

COMPASS

A Mission to the Solar System's Greatest Particle Accelerator

JOHNS HOPKINS APPLIED PHYSICS LABORATORY

Science Objectives

Origins

1. Discover how moon and ring material in the Jovian space environment contribute to radiation belts
2. Reveal the additional particle sources of the Jovian radiation belts

Acceleration

3. Discover how Jupiter accelerates charged particles to such exceptionally high energies

Loss

4. Reveal the loss processes of energetic charged particles in Jupiter's magnetosphere and resulting X-ray emissions

Mission Overview

- Jupiter orbiter with several deep dives into the core radiation belt and synchrotron regions
- Powered by 72m² roll out solar arrays
- Nine science instruments with unprecedented charged particle energy coverage, full spectrum of plasma waves, and first-ever dedicated X-ray imager at Jupiter
- A visual camera for public outreach
- Continuous burst data acquisition
- Monopropellant hydrazine system provides 1,500 m/s delta-V
- X-band direct-to-Earth communications
- Close flybys of Io & Callisto enable potential enhancing opportunities for moon science
- Mission duration: 514 days, 15 orbits
- Planetary Protection: Impact with Jupiter
- Cost: $FY22 1.2B—Phases A-F, 50% reserves, including launch vehicle

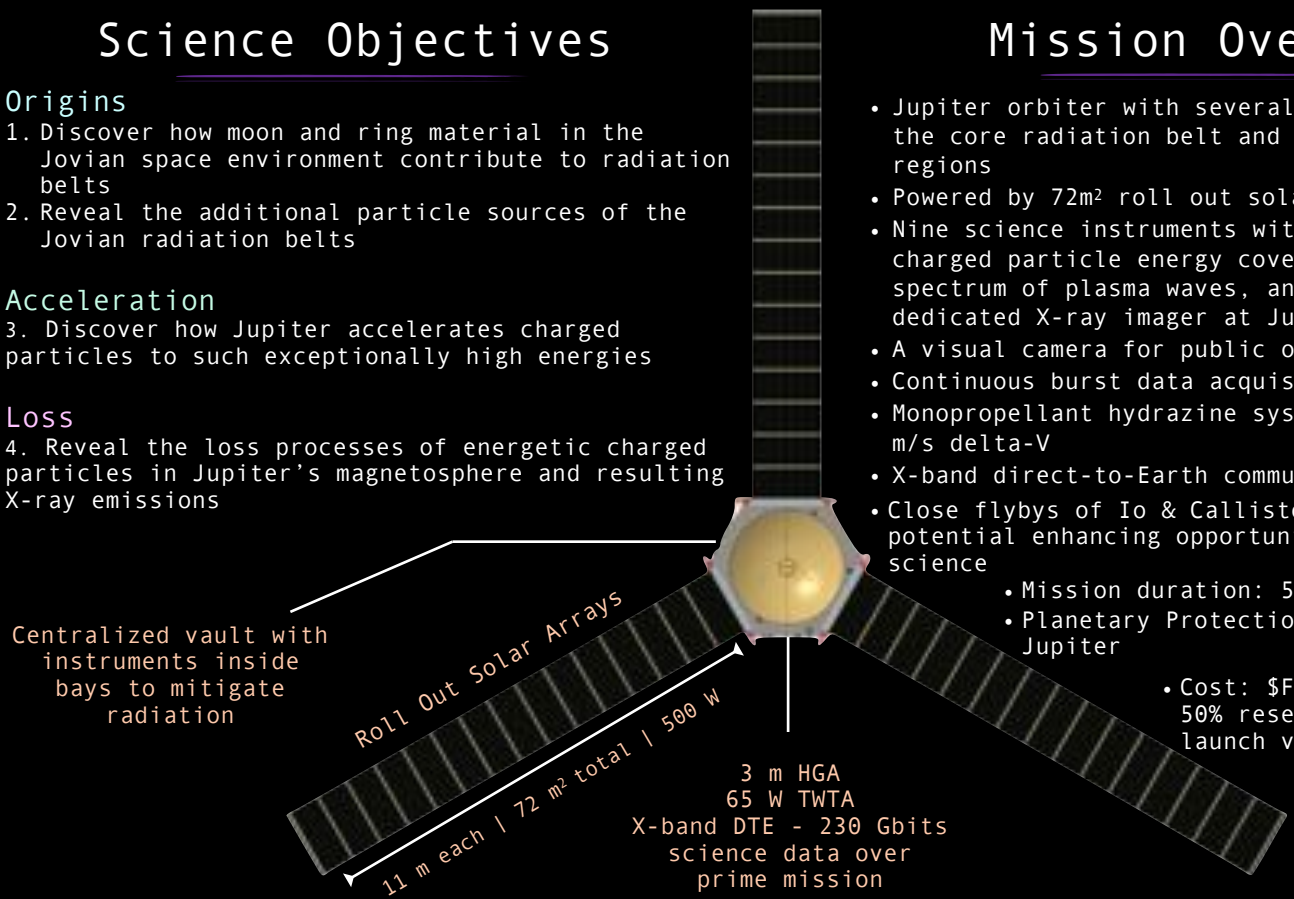

Mission Timeline*

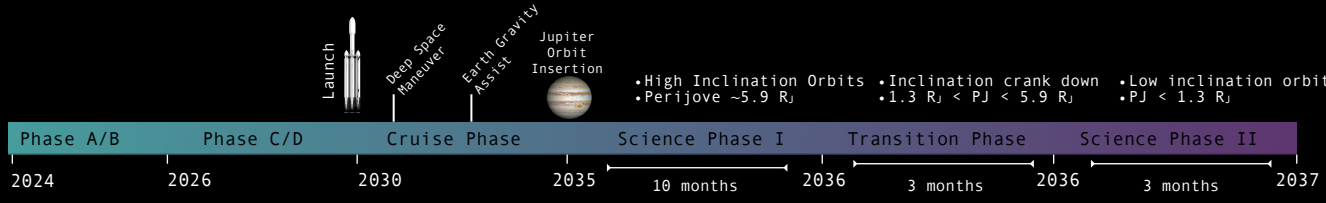

** representative timeline: mission design is extremely flexible with multiple launch windows*

Concept of Operations

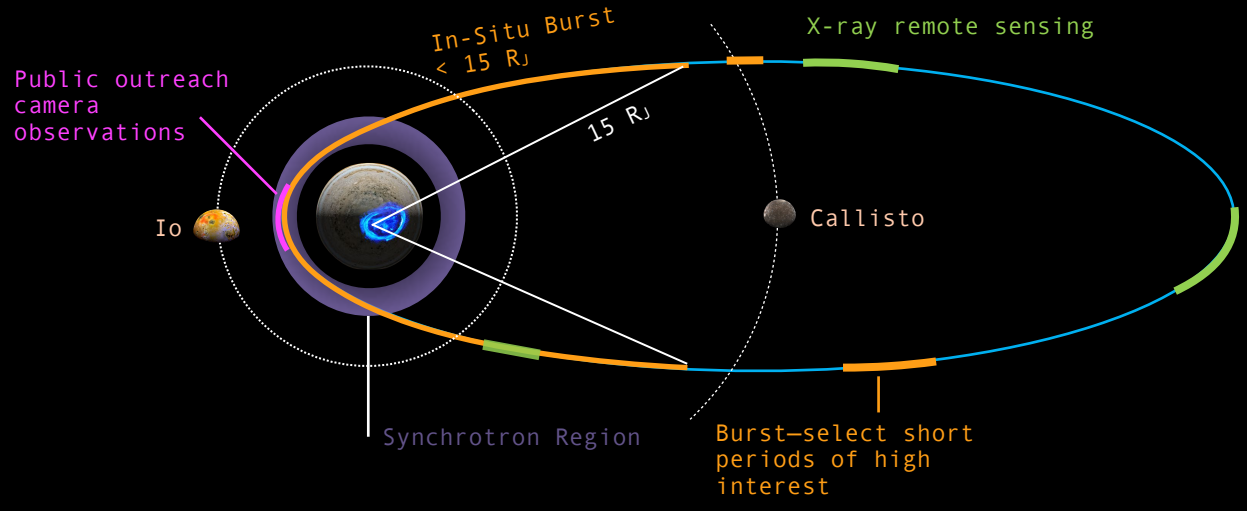

COMPASS

Science Payload

Instruments		Mass* (MEV)	Power
TPD:	Thermal Plasma Detector	7.7 kg x2	6 W x2
SPD:	Suprathermal Particle Detector	19.0 kg	11.0 W
EPD:	Energetic Particle Detector	10.3 kg	3.6 W
RPD:	Relativistic Particle Detector	17.8 kg	7.1 W
UPD:	Ultra-relativistic Particle Detector	13.3 kg	16.5 W
FGM:	Fluxgate Magnetometer	1.8 kg x2	4.8 W x2
SCM:	Search Coil Magnetometer	7.9 kg	1.2 W
EFW:	Electric Field Waves	14.6 kg	17.7 W
XRI:	X-Ray Imager	16.5 kg	6.9 W
EPOC:	Education & Public Outreach Camera	6.5 kg	2.7 W

** includes shielding mass*

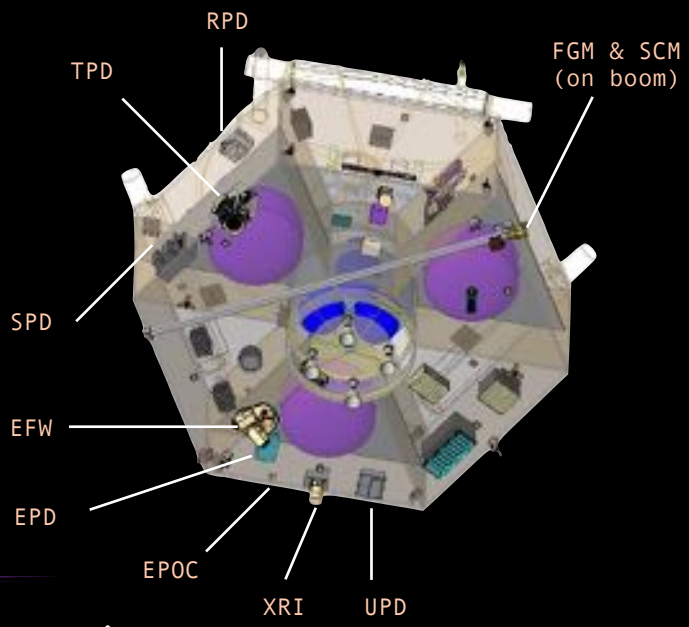

Science Phases & Radiation Mitigation

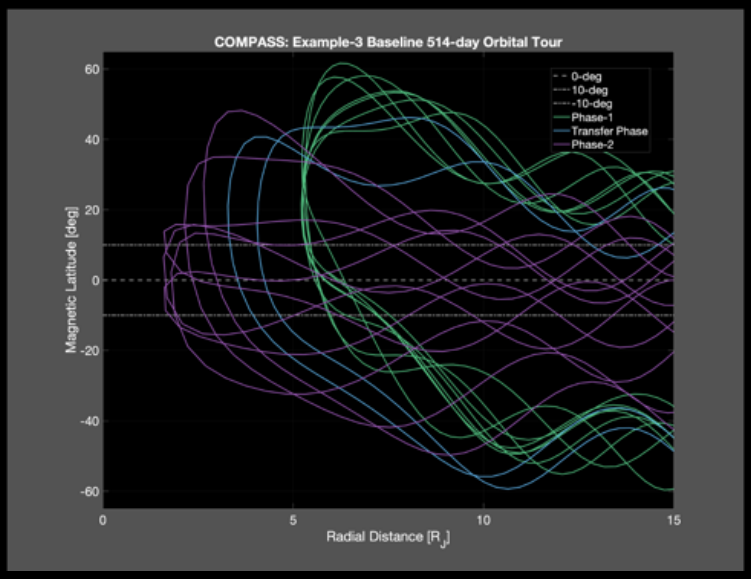

Total Dose (krad, RDMx2)

< 300 krad after Io pump down

~900 krad at end of phase I

~1.8 Mrad at end of mission

NASA's Clipper Mission ~2.7 Mrad

Science Phase I

Address particle origins & losses (through remote X-ray imaging and in situ) and acceleration beyond Io

Multi-phased approach that addresses closure while mitigating radiation risks

Address particle origins & losses (focusing on in situ) as well as the acceleration in the "heart" of the radiation belts

Science Phase II

Cross-Disciplinary Science Approach

Jupiter's trapped radiation & X-ray emissions make it an ideal stepping stone for using fundamental plasma physics to bridge the gaps between planetary magnetospheres and astrophysical systems.

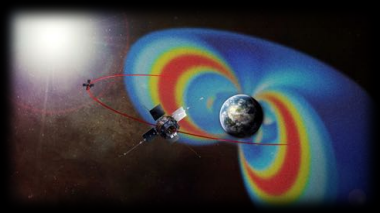

Heliophysics

COMPASS will extend what Van Allen Probes has accomplished at Earth to Jupiter's extreme environment.

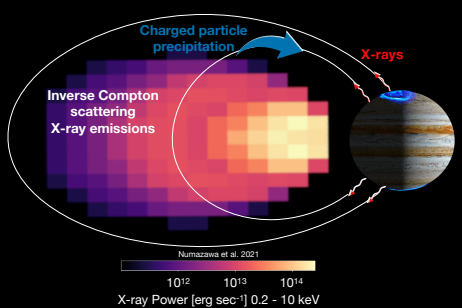

Astrophysics

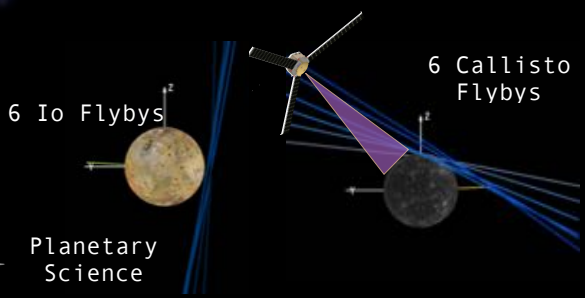

Planetary Science

COMPASS can probe elemental and chemically specific X-ray fluorescence lines with its X-ray imager.

COMPASS

Concept Study Team

Name	Role	Affiliation
George Clark	Principal Investigator	Johns Hopkins Applied Physics Laboratory (APL)
Jim Kinnison	Study Design Lead	APL
Dan Kelly	Study Design Lead	APL
Peter Kollmann	Topic Lead: Acceleration	APL
Wen Li		Boston University
Allison Jaynes	Topic Lead: Origins	University of Iowa
Lauren Blum	Topic Lead: Loss	University of Colorado Boulder
Robert Marshall		University of Colorado Boulder
Drew Turner	Project Science	APL
Ian Cohen		APL
Sasha Ukhorskiy	Science Mentorship	APL
Barry Mauk		APL
Elias Roussos	Jupiter & Earth Radiation Belt Expertise	Max Planck Institute for Solar System Research
Quentin Nénon		Research Institute in Astrophysics and Planetology
Sasha Drozdov		University of California Los Angeles
Xinlin Li		University of Colorado Boulder
Emma Woodfield		British Antarctic Survey
Will Dunn	X-ray Science & Astrophysics Expertise	University of College London
Grant Berland		University of Colorado Boulder
Ralph Kraft		Harvard University
Peter Williams		Harvard University
Todd Smith	Theory & Modeling Expertise	APL
Kareem Sorathia		APL
Anthony Sciola		APL
George Hospodarsky	Particle & Field Instrumentation Leads	University of Iowa
Xin Wu		University of Geneva
Paul O'Brian		The Aerospace Corporation
Mark Looper		The Aerospace Corporation
Angelica Sicard	Salammbô Simulation Support	The French Aerospace Lab (ONERA)
Andy Santo	Project Management	APL
Meagan Leary	Design Study Team	APL
Amanda Haapala	Design Study Team	APL
Fazle Siddique	Design Study Team	APL
Michelle Donegan	Design Study Team	APL
Ben Clare	Design Study Team	APL
Derek Emmell	Design Study Team	APL
Kim Slack	Design Study Team	APL
John Wirzburger	Design Study Team	APL
Daniel Sepulveda	Design Study Team	APL
Lew Roufberg	Design Study Team	APL
Jackie Perry	Design Study Team	APL
John Schellhase	Design Study Team	APL
Darrius Pergosky	Design Study Team	APL
Liz Able	Design Study Team	APL
Mike O'Neill	Design Study Team	APL
Cris Fernandes	Design Study Team	APL
Deb Chattopadhyay	Design Study Team	APL
Samuel Bibelhauser	Design Study Team	APL
Seth Kijewski	Design Study Team	APL
Joe Pulkowski	Design Study Team	APL
Mike Furrow	Design Study Team	APL

Executive Summary

Radiation belts are regions of trapped high energy charged particles and are found at all of the sufficiently magnetized planets in the Solar System. **This fact is quite remarkable, since it implies that particle trapping and acceleration in magnetospheric systems is potentially a universal process in planetary magnetospheres and likely beyond to other astrophysical systems.** Of these known radiation belt systems around the Sun, Jupiter reigns supreme by accelerating particles to ultrarelativistic energies. Such high energy thresholds and intensities of trapped radiation render Jupiter more in line with astrophysical systems, like the magnetospheres of pulsars and brown dwarfs, where electron synchrotron emissions represent a significant loss process that can be observed remotely from Earth. **Therefore, Jupiter is an ideal stepping stone for using fundamental magnetospheric and plasma physics to bridge the gaps between Earth (advanced so profoundly by Van Allen Probes), planetary magnetospheres, and astrophysical systems.** Despite several missions having been dedicated to studying different aspects of the Jovian planetary system, **no observatory has yet been fully dedicated—or sufficiently instrumented—to understanding why exactly Jupiter in many ways acts as the Solar System's greatest particle accelerator.** Planned missions, such as JUICE and Europa Clipper, will also avoid the core region of the radiation belts—and are also insufficiently instrumented, thus leaving many fundamental questions and discoveries open. Therefore, to make great strides in understanding particle acceleration more generally we must first understand the distinctive and universal processes that drive the most intense radiation belts in the Solar System by addressing the following objectives: (1) *origins*: revealing how moon and ring materials contribute to the radiation belts even though they simultaneously limit them; (2) *acceleration:* discover how Jupiter accelerates charged particles to exceptionally high energies; and (3) *loss*: reveal the loss processes of relativistic charged particles in Jupiter's magnetosphere and resulting X-ray emissions. **Comprehensive Observations of Magnetospheric Particle Acceleration, Sources, and Sinks (COMPASS) is a revolutionary concept that will be the first dedicated mission to the "heart" of Jupiter's radiation belt region to address the fundamental mysteries in Heliophysics outlined by the broader scientific community** (e.g., Roussos et al., 2021, Nénon et al., 2021) **and will extend what Van Allen Probes has accomplished at Earth to even more extreme environments.**

COMPASS is a Heliophysics Mission Concept Study (HMCS) conceptualized and developed for consideration by the 2024-2033 Solar and Space Physics Decadal Survey. This report provides a point design that represents a concept maturity level of 4 (CML-4), which demonstrates that COMPASS is technically feasible, fully addresses its science objectives, and minimizes risk and cost of implementation. In summary, COMPASS is a single, solar powered spinner outfitted with comprehensive charged particle instrumentation that spans an unprecedented species and energy range, a magnetometer, plasma waves instruments to diagnose the full wave spectrum with multidirectional antennas, and the first-ever dedicated X-ray imager. COMPASS can be delivered to the Jupiter system via an expendable Falcon Heavy launch vehicle with ΔV-Earth gravity assist (EGA) trajectory and an interplanetary cruise time of flight of 5.5 – 6 years. **The prime science mission consists of a multiple phased approach to mitigate the effects of Jupiter's intense radiation environment, while still enabling critical observations into the most-intense radiation belts in the Solar System.** Altogether, the prime mission comprises 15 orbits spanning ~1.5 years.

The full life cycle cost (Phases A-F; with 50% unencumbered reserves, including the launch vehicle) is ~$1.2B (FY22$).

1. Science Motivation

Analogous to Jupiter's Great Red Spot—the largest storm in the Solar System—the Jovian radiation belts are a distinguishing characteristic among planetary magnetospheres. Simply put, the **Jovian radiation belts are the most intense and energetic in the Solar System** (e.g., Mauk & Fox, 2010), and yet we know very little about them. And despite several missions having been dedicated to studying different aspects of the Jovian planetary system, which excluded the radiation belt regions, **no observatory has yet been fully dedicated—or sufficiently instrumented—to understanding why exactly Jupiter, in many ways, acts as the Solar System's greatest particle accelerator** (Exhibit 1-1). Planned missions, such as JUICE and Europa Clipper, will entirely avoid the core region of Jupiter's radiation belts and are also insufficiently instrumented to cover and resolve its highest energies, thus leaving many fundamental questions and discoveries open for exploration (e.g., Roussos et al., 2021).

The basic motivation to explore such a hazardous region is to expand the frontiers of Heliophysics in the next decade by investigating extreme radiation environments that allow us to bridge the gaps between radiation belt physics at Earth, planetary magnetospheres, and the cosmos (e.g., Roussos et al., 2021, Kollmann et al., 2022, Turner et al., 2022, Nénon et al., 2022). In pursuit of distinct and universal processes that ultimately sculpt space environments, not only will COMPASS make great strides in understanding acceleration processes more generally, but it will also inform our ability to diagnose habitability across diverse systems. Jupiter, for many reasons, is the natural stepping stone because it sets itself apart by the *strongest* magnetic field, *largest* magnetosphere, the *most active* moon, Io, (which is the primary plasma source), the *fastest* rotation, and the *most powerful aurora and radiation belts* (e.g., Mauk & Fox, 2010, Bolton et al., 2004). Additionally, Jupiter's environment continuously exists in a state that cannot be emulated elsewhere in the Solar System—not even during extreme space weather

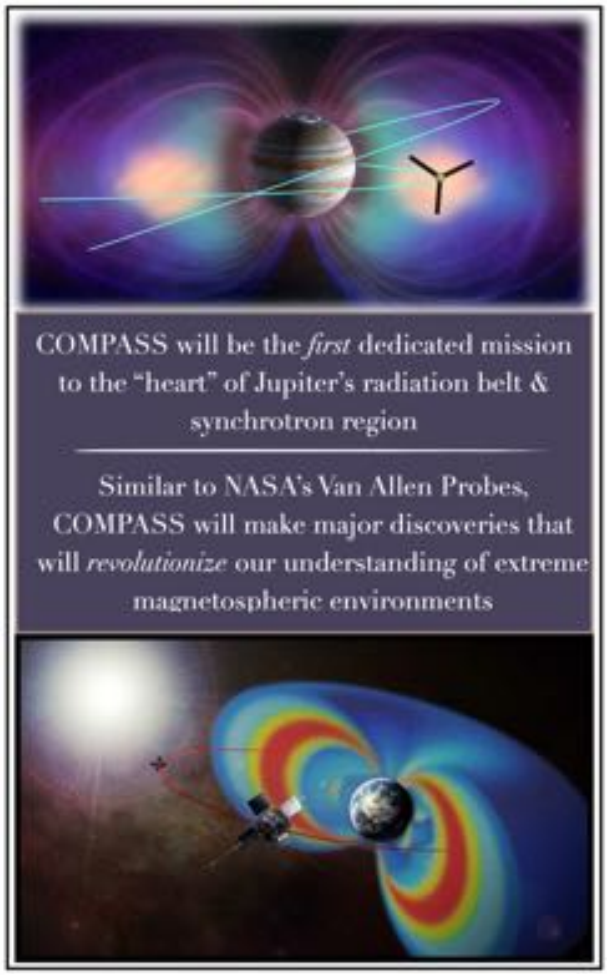

Exhibit 1-1: COMPASS will extend and apply what Van Allen Probes has revealed at Earth to Jupiter's extreme environment.

events at Earth. For example, Jupiter's magnetic field is ~20,000 times stronger than Earth's, which easily sustains the observed > 1 GeV ions (e.g., Roussos et al., 2021) and > 30 MeV electrons (e.g., Kollmann et al., 2018) and is expected to trap and accelerate particles far beyond those energies, i.e., >100 GeV ions and > 50-70 MeV electrons. For reasons currently unknown, particles are accelerated and accumulated to those high energies, thus forming the most intense radiation belts in the Solar System. The electrons are so energetic and intense that they produce two unique attributes: 1) strong synchrotron radiation that is detectable with radio telescopes (e.g., de Pater, 2003; Bolton et al., 2002, Santos-Costa et al., 2001; Santos-Costa & Bolton, 2008), and 2) Jovian electrons that leak out of the system overwhelm Galactic

Cosmic Rays (GCRs) throughout the solar system inside of ~10 AU (e.g., Baker et al., 1979; Millan & Baker, 2012; Roussos et al., 2021, Nénon et al., 2021 and references therein).

How does Jupiter accelerate electrons to these ultra-relativistic energies? Gyro-resonant acceleration by whistler waves is likely the prevailing mechanism responsible for Earth's outer radiation belt (e.g., Horne & Thorne, 1998; Summers et al., 1998) and it has been proposed as a viable hypothesis in forming Jupiter's ultra-relativistic electrons (Horne et al., 2008; Woodfield et al., 2014) However, it remains unknown if this is indeed the prevalent process at Jupiter—and therefore possibly all planetary systems—or if other mechanisms play a more dominant role. For example, Jupiter's enormous, material-laden magnetosphere and strong magnetic field may change our fundamental picture of radiation belt physics as we discover how these extreme magnetospheres are governed. High impact results from Juno have revealed that electrons over the auroral regions of Jupiter are routinely accelerated to multi-MeV energies and may play an important role in seeding Jupiter's radiation belts (Mauk et al., 2017; Paranicas et al., 2018; Clark et al., 2017).

Recent results underscore that the high energies found at Jupiter open the window to observe physics that is otherwise only accessible indirectly. Heavy ion distributions deep in the radiation belts reveal a local source of >50 MeV/nucleon oxygen (Roussos et al., 2022)—the physics of which cannot be studied in the Terrestrial magnetosphere but appear to have stronger parallels to stellar or astrophysical acceleration processes (e.g., Doyle et al., 2021). Finally, Jupiter is so massive that of all planets within our reach it is thought to accumulate the highest amounts of dark matter. Another theory suggests that this matter decays into >10MeV electrons, providing an additional source process to the radiation belts that holds signatures of the mass of the dark matter particles – a parameter that to date is a complete mystery (Li and Fan 2022). Therefore, studying Jupiter may even inform on the forces that literally hold our galaxy and the universe together.

Another striking difference between Earth and Jupiter is the source of plasma. Earth's primary source is external, i.e., from the solar wind, with a lesser contribution from the ionosphere; however, at Jupiter the dominant source is from its geologically-active moon, Io. Io provides roughly 1 ton/s of SO_2 into the system via interactions between Io's atmosphere and Jupiter's plasma environment. SO_2 dissociates rapidly and becomes ionized via the hot magnetospheric electron population, which results in a multi-species, multi-charge-state plasma (e.g., Mauk et al., 2004; Hamilton et al., 2005; Clark et al., 2016; Clark et al., 2020). The wealth of different particle masses and charge states offers great opportunities to study candidate acceleration processes that respond differently to these quantities (Exhibit 1-2), if future missions are appropriately instrumented to make composition and charge-state measurements (e.g., Artemyev et al., 2020). The global circulation of these energetic ions and electrons through a combination of various candidate transport, acceleration, and loss processes brings them through regions of neutral gas, moons, ring/dust materials and areas of intense plasma waves that scatter particles into the atmosphere. Although many of these mechanisms can act as sinks, the energetic charged particles are able to persevere and form the most intense and energetic radiation belts in the Solar System. Given how strong both particle supply and losses are, it is a mystery why their balances lead to extreme radiation. While several ideas have been developed over the past, all fall far short of appreciating the relative roles of all the competing processes, let alone achieving a predictive understanding.

The examples above form the underlying science theme of this mission concept:

Exploring the distinctive and universal acceleration, source, transport, and loss processes that drive the most intense radiation belts in the Solar System.

The Comprehensive Observations of Magnetospheric Particle Acceleration, Sources, and Sinks (COMPASS) mission is a revolutionary concept that will be the **first dedicated mission to the "heart" of Jupiter's radiation belt region to address the fundamental mysteries in Heliophysics outlined by the broader scientific community** (e.g., Roussos et al., 2021; Kollmann et al., 2022; Nénon et al., 2021; Li & Hudson et al., 2019). COMPASS stands on the shoulders of recent missions such as the Van Allen Probes and Parker Solar Probe (Exhibit 1-1) by **providing direct measurements of the most extreme and complex space environments, previously deemed beyond the reach of *in situ* probes**, to unveil the mysteries of plasma, wave, and particle physics that sculpt particle radiation belt systems across the universe.

1.1 Scientific Objectives & Traceability

To make significant progress toward understanding the distinctive and universal processes at play across complex space environments, focused science objectives supported by key questions are critical. This is especially true for Jupiter's space environment since its large, material-laden magnetosphere with active moons hosts numerous processes that simultaneously facilitate in the production, but also sculpt losses in particle distributions. Therefore, it is necessary to understand how particle *origins*, *acceleration*, and *loss* processes compete across a multi-dimensional parameter space that includes space, time, energy, composition and charge state (Exhibit 1-3). The high-level COMPASS science objectives and fundamental mysteries in Jupiter's magnetosphere are depicted in Exhibit 1-3. These

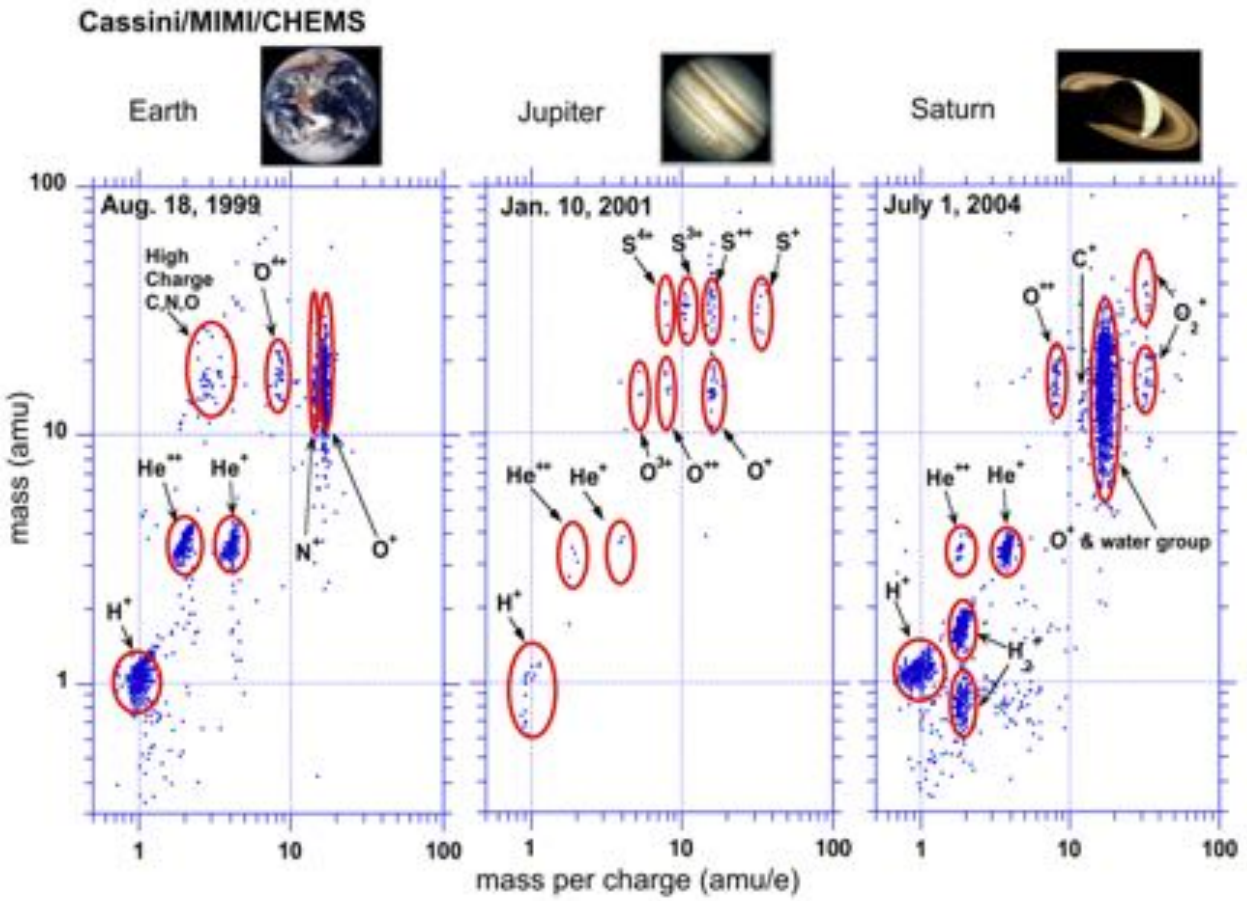

Exhibit 1-2: Jupiter's magnetosphere contains the largest range of ion masses and charge states—making it easier to probe fundamental processes that also exist Earth, i.e., mass vs. charge dependent acceleration (from Hamilton et al., 2005).

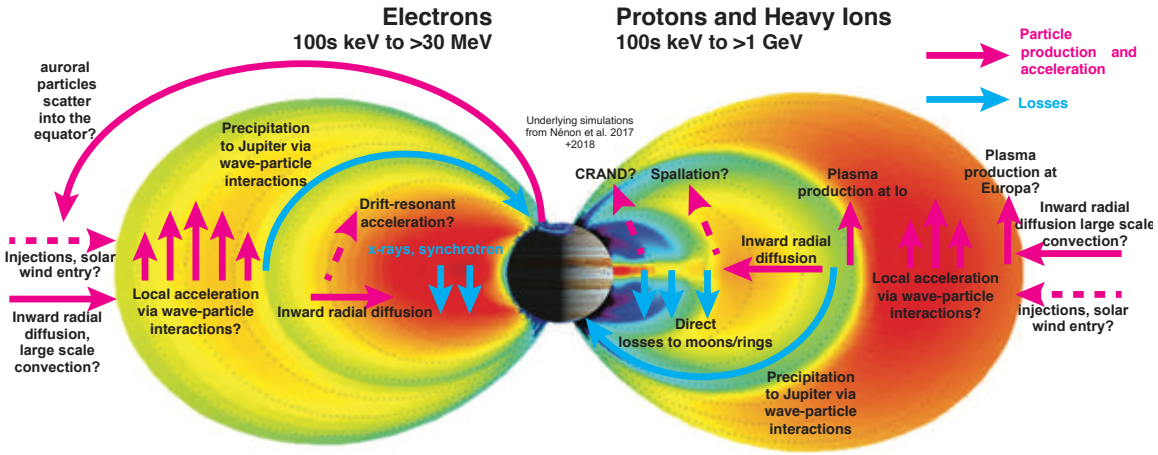

High-level Science Objectives

Particle Origins 1. Discover how moon and ring material in the Jovian space environment contribute to the radiation belts 2. Reveal the additional particle sources of the Jovian radiation belts
Acceleration 3. Discover how Jupiter accelerates charged particles to such exceptionally high energies
Loss 4. Reveal the loss processes of energetic charged particles in Jupiter's magnetosphere and resulting X-ray emissions

Exhibit 1-3: COMPASS will unravel the fundamental mysteries of Jupiter's radiation belts by addressing several high-level science objectives of significant relevance to the Heliophysics community.

science objectives lead to the following main observational drivers mapped in the Science Traceability Matrix (STM) shown in Exhibit 1-4: 1) high-fidelity energy- and angular-resolved measurements of the electron and ion populations ranging from thermal energies to > 70 MeV for electrons and to ~1 GeV for ions; 2) compositional and charge state determination of suprathermal (> 10 keV/Q) ions; 3) AC electric and magnetic plasma wave vectors as well as DC vector magnetic field; 4) novel X-ray imaging of Jupiter's electron radiation belts and signatures of the interaction of electrons and ions with Jupiter's atmosphere, plasma and neutral tori, and moon surfaces. More details on these objectives can be found in the Appendix.

Particle Origins. ***Is sourcing from active moons (e.g., Io & Europa) sufficient to provide seed electron and ion populations to produce and sustain Jupiter's radiation belts?*** Jupiter is known for its magnetosphere filled with ions originating from its geologically active moons, where oxygen and sulfur intensities rival those of protons (Mauk et. al 2004; Smyth and Marconi 2006; Smith et al. 2019). Yet, major questions remain even on the origin of the heavy ions. Both Io and Europa exhibit geologic activity (e.g., Roth et al., 2014), but it is unclear which of them is the major oxygen source for the radiation belts. In addition to the moons, the rings in Jupiter's system might also be a source of heavy ions due to fragments of atomic nuclei being liberated via high-energy particle interactions (Roussos et al., 2021). COMPASS is tailored to measure the species and charge states of ions, which can be compared to physical ion chemistry models to disentangle the roles of Io and Europa from atmospheric processes (e.g., Smith et al., 2019). (Further details on how COMPASS will close its science questions are provided in the Appendix.) While moons, their associated neutral gas tori, and rings provide particles to the radiation belts, these objects also simultaneously remove particles through absorption or cooling from Coulomb collisions (Clark et al., 2014, Nénon et al., 2018). Understanding the balance of sources and losses is absolutely critical in understanding the dynamics of radiation belts (*see loss objective*).

Exhibit 1-4. COMPASS Science Traceability Matrix

Topic	Science Goal	Science Objective	Measurement Approach	Measurement Requirements		Relevant Instrument	Mission Requirements	Phase
Particle Origins	Discover how moon and ring material in the Jovian space environment contribute to the radiation belts	Discover whether nuclear collision processes may be a significant particle origin for ion radiation belts	Radial profiles of species-resolved ion phase space density as a function of first and second adiabatic invariants	Energy Range: 0.1-100 MeV/nuc Energy Res: ≤ 10% Species Res: H, He, Li-B, C, N, O, F-P, S Time Res: ≤ 10 min Angular Res: ≤ 30 deg		EPD RPD UPD	L-shell: inward of 10; inclination <20deg; ensure 180° PA coverage each spin	II
				Dimensions/Components: 3 Dynamic Range: 100nT-4G; Res: 1 nT Time Res: ≤ 10 min		FGM	EM clean s/c	
		Determine the relative roles of Io and Europa in providing the seed population of the radiation belts	Energy distribution of ion composition and charge state and electrons between Io and Europa	MR1	Energy Range: 10eV/q-1keV/q OR 10-100 keV/q Energy Res: 20% Species Res: e-, H, He, C, N, O, S (incl. q, particularly O+ vs. S++) Time Res: ≤ 10 min Angular Res: ≤ 30deg	SPD	5 < L < 20; inclination <20deg	I & II
			Electron energy spectrum and pitch angle distribution	MR2	Energy Range: 0.01-10 keV Energy Res: 10% Species Res: e- Time Res: ≤ 10 min Angular Coverage: pitch angle coverage Angular Res: ≤ 30deg	TPD	5 < L < 20; inclination <20deg	
				Dimensions/Components: 3 Dynamic Range: 100nT-4G Res: 1 nT Time Res: ≤ 10 min		FGM		
	Reveal additional particle sources of the Jovian radiation belts	Determine the fraction of solar wind ions in the radiation belts and quantify contribution from solar wind electrons	Radial profiles of electron phase space density as a function of first and second adiabatic invariants	Magnetic field: Dynamic Range: 1nT-4G Res: 1%		FGM	≥60 R_J (Delamere & Bagenal, 2010); EM clean s/c	I
				Energy range: 10 eV-10 MeV Species: e- Energy Res: 10% Time Res: 10 min Angular Res: ≤ 30deg		EPD RPD UPD		
			Ion composition and charge state	See MR1		SPD	Measurements in the solar wind region (can be during cruise)	
		Determine the role of the atmosphere in seeding the radiation belts	Energy spectrum and pitch angle distributions of electrons and ions in regions mapping to the Jovian auroral zones	Energy Range: 0.001-10 MeV/nuc Energy Res: 20% Species Res: H, C, N, O, S, e- Time Res: 10 s (spectra); 60 s (PAD) Angular Res: 15deg, Cover the field aligned direction		EPD & RPD	Ensure 180deg PA coverage each spin; 20<L<50	

Topic	Science Goal	Science Objective	Measurement Approach	Measurement Requirements		Relevant Instrument	Mission Requirements	Phase
Acceleration	Discover how Jupiter accelerates charged particles to such exceptionally high energies	How are particles accelerated to <1MeV energies and transported to L<30?	Ion and electron energy spectrum, pitch angle, and ion composition and charge-state	Dynamic Range: 1-100 nT Res: 1% Time Res: 0.02 s		FGM	Coverage L < 30; Instrument looking into corotation direction and covering all pitch angles	II
				Energy Range: ~0.01-~1MeV/nuc Energy Res: 10%	Species Res: H, C, N, O, S, e- Time Res: 10 s (spectra) Angular Res: 30deg	SPD, EPD		
			3D, high resolution wave activity and plasma density from upper hybrid line	MR3	Dimensions/Components: 3 Frequency Range: 50 Hz - 3 MHz Res: 10% Time Res: ≤2 min	EFW	EM clean spacecraft	
				MR4	Dimensions/Components: 3 Frequency Range: 50 Hz-30 kHz Res: 10% Time Res: ≤2 min	SCM		
		Determine where and via which processes, > 1 MeV radiation belt particles of different species are accelerated locally	Radial profiles of species-resolved ion and electron phase space density as a function of first and second adiabatic invariants	MR5	Dimensions/Components: 3 Time Res: ≤ 12 s	FGM	FR1: L < 30 <20 deg inclination >= 3 passes over one solar rotation (~27 days)	II
				MR6	Energy Range: 0.01 - ≥50 MeV/nuc Energy Res: ≤ 30% Species Res: e-, H, He, O, S Time Res: ≤ 10 min Angular Res: ≤ 20 deg	SPD, EPD, RPD, UPD	Ensure 180 deg PA coverage each spin	
			Plasma density for acceleration evaluation	MR2 & MR3		TPD & EFW	Ensure coverage of freq. range in EFW/SCM and co-rotation direction each spin for TP; L<30; latitude coverage	I & II
			Waveforms and spectral matrices of relevant plasma waves relative to Jupiter	MR3, MR4, MR5		EFW, SCM, FGM		
		Uncover the drivers responsible for radial transport of ≳1 MeV energy particles with different species	Ion & electron radial distributions of particle phase space density	MR5		FGM	FR1	II
				MR6		SPD, EPD, RPD, UPD		
			ULF Waves	Dimensions/Components: 3 Dynamic Range: 0.1nT-4G	Res: 1% Time Res: <1 s	FGM	EM clean s/c	
			Zebra stripes, moon microsignatures, flow anisotropies, injections	Energy Range: 1-100 MeV Energy Res: 5%	Species Res: e- Time Res: 1 min Angular Res: 30deg	EPD, RPD, UPD	Orbital coverage 2 < L < 30	
			Dynamics of MeV electrons in the radiation belts and MeV ions in the Io plasma torus	X-ray Energy: 0.2 - 5 keV (0.2-1.5 keV for MeV H, O, S; 2-5 keV for MeV electrons);	Energy resolution = ~150 eV FWHM FoV = 22deg +/- 5deg Spatial Res: 1 RJ resolution; 1 s at PJ, 10 s elsewhere.	XRI	Point XRI at inner magnetosphere for > 1 ks each orbit; inner magnetosphere during high inclination orbits	I & II
			Local time asymmetries in energetic particle intensities	Energy Range: 100keV - 50 MeV/nuc Energy Res: 10%	Species Res: e-, H, O, S Time Res: 10 min Angular Res: 30deg	TPD, EPD, RPD, UPD	Line of apsides ±3 hr to dawn-dusk axis	

Topic	Science Goal	Science Objective	Measurement Approach	Measurement Requirements	Relevant Instrument	Mission Requirements	Phase
Loss	Reveal the loss processes of energetic charged particles in Jupiter's magnetosphere and resulting X-ray emissions	Determine the contribution of atmospheric precipitation to radiation belt dynamics	Waveforms and spectral matrices of relevant plasma waves relative to Jupiter	Dimensions/Components: ≥2 Frequency Range: ~1kHz to 400 kHz Time Resolution: 2 min	EFW	EM clean s/c	I & II
				Dimensions/Components: 3 Frequency Range: DC to 20 kHz Time Resolution: 1 nT	FGM & SCM		
			Plasma density for scattering evaluation	MR2 & MR3	TPD, EFW	EM clean s/c	
			Particle energy and pitch angle distributions and phase space density as a function of radial distance from Jupiter	Energy Range: ~10 keV/nuc to ≥10MeV/nuc Energy Res: 20% Species Res: H, C, N, O, S, e- Time Res: 10 s (spectra); 60 s (PAD)	SPD, EPD, RPD, UPD	~1.5< L< 10; inclination <20 deg; ensure 180 deg PA coverage each spin	
				Angular Res: 15 deg Magnitude Accuracy: 1 nT Magnitude Range: +/-100,000 nT Direction Accuracy: <30 deg Time resolution: <1 min	FGM	EM clean s/c	
			Precipitation flux and energy distribution of energetic electrons and ions incident on the atmosphere across L and MLT	X-ray Energy: 0.2 -~10 keV Energy resolution: 20% Sensitivity (min flux): 0.1 (cm^2 s keV)^-1 Latitude resolution: 0.1L Cadence (Time Resolution): 1 sec	XRI	Point instrument at Jupiter 30<LAT<45deg; periapsis: 4 < L < 6	
		Determine the contribution of the moons and ring orbits to radiation belt losses	Particle energy and pitch angle distributions as a function of radial distance from Jupiter	Energy Range: 0.01 to 1 MeV/nuc Energy Res: 10% Species Res: e-, H, He, C, N, O, S Time Res: 10 min Angular Res: 10deg	EPD, RPD, UPD	ensure 180deg PA coverage each spin; 5 < L < 12	
				MR5 and in addition: Direction Accuracy: <30 deg Time resolution: <1 min	FGM	EM clean s/c	
			Loss rate and energy spectrum of particles impacting moons	X-ray Energy: 0.2 -~20 keV Energy resolution: 10% Sensitivity (min flux): 0.1 (cm^2 s keV)^-1 Angular Resolution: 1 deg Cadence (Time Resolution): 5 sec	XRI	Point instrument at moons each orbit; Instrument boresight in spin plane; Moons in spacecraft spin plane to increase observation duration	

Can the aurora, solar wind, or atmosphere provide significant particles to the radiation belts? While a lot of attention in the planetary community was focusing on particle origins related to moons and rings, there is observational evidence that additional processes are at play. For example, the solar wind may gain access to the magnetosphere—a process important at Earth (e.g., Paschmann et al., 1979; Russell, 2000; Hasegawa et al., 2004; Wing et al., 2014; Sorathia et al., 2019)— and supply the population of protons and electrons (e.g., Hamilton et al., 1981; Delamere et al., 2010). Moreover, auroral regions of both Earth and Jupiter are known to be sources of energetic ions and electrons. Possibly unique to Jupiter, auroral populations are routinely accelerated to energies > several MeV (e.g., Mauk et al., 2017; Paranicas et al., 2018; Clark et al., 2017). Jupiter's magnetosphere is also filled with MeV electrons out to the magnetopause region (e.g., Van Allen et al., 1974; Kollmann et al., 2018) suggesting that the original field-aligned particles accelerated in the auroral region may be scattered and end up supplying the equatorial radiation belts (e.g., Speiser, 1965; Young et al., 2008; Roussos et al., 2021; Exhibit 1-5). Finally, Jupiter's atmosphere can also produce charged particles via the Cosmic Ray Albedo Neutron Decay (CRAND) process, where protons and electrons are produced from interactions between Galactic Cosmic Rays (GCRs) and Jupiter's mostly hydrogen atmosphere (Blake & Schulz, 1980; Nénon et al., 2018). This process is observed at Earth (e.g., Selesnick et al., 2014; Li et al., 2017) and Saturn (e.g., Cooper, 1980; Blake et al., 1983; Cooper, 1983; Kollmann et al., 2022), but its significance at Jupiter has not been proven. COMPASS can distinguish these processes by observing the angular distribution of ions and electrons mapping to Jupiter's auroral zone. Additionally, COMPASS is tailored to measure the species and charge states of ions which can be compared to physical ion chemistry models to disentangle the roles of Io and Europa from atmospheric processes (e.g., Smith et al., 2019).

Acceleration. ***What processes are responsible for accelerating ions and electrons to such exceptionally high energies in Jupiter's radiation belts and magnetosphere?*** The acceleration processes at Earth are also operating at Jupiter, i.e., radial transport & wave-particle interactions, but their relative significance may be very different. The fact that particle production and acceleration can overcome Jupiter's material-laden magnetosphere that absorbs and cools charged particles, and still greatly exceed the energies and intensities found in any other planetary environment is one of the biggest mysteries in Heliophysics. What makes Jupiter so compelling as a natural laboratory is that it is likely easier to disentangle the interplay between the different acceleration processes found at Earth, even though Earth's space environment is easier to access and less risky in terms of radiation effects. That is because at Earth, local acceleration occurs over a broad range of radiation belt L-shells (e.g., Horne et al., 2005; Thorne et al., 2013; Baker et al., 2014; Shprits et al., 2008; Reeves et al., 2013; Ma et al., 2018; Boyd et al., 2018); however, strong wave activity in Jupiter's magnetosphere is found near the Galilean moons (Exhibit 1-5) (e.g., Menietti et al., 2021). Note that our picture of plasma waves elsewhere is incomplete due to limited coverage, especially inside of Io's orbit. Acceleration from radial transport may prove to be a dominant process, which arises from inward radial diffusion (e.g., Kollmann et al., 2018) driven by: random field fluctuations in the magnetosphere or the ionosphere (e.g., Lejosne & Kollmann, 2020), centrifugally driven interchange (e.g., Mauk et al., 2002), or large-scale coherent transport (e.g., Hao et al., 2020). Non-adiabatic transport may occur during reconnection in the Jovian magnetodisk and/or magnetotail (e.g., Vogt et al., 2020) or at low altitudes (Masters et al., 2021), leading to acceleration processes that are in principle similar to those found in Earth's magnetotail (e.g., Turner et al., 2021; Cohen et al., 2021). One of the major thrusts of COMPASS is to *cleanly*—meaning high signal to noise through whatever means necessary—measure energy- and pitch-

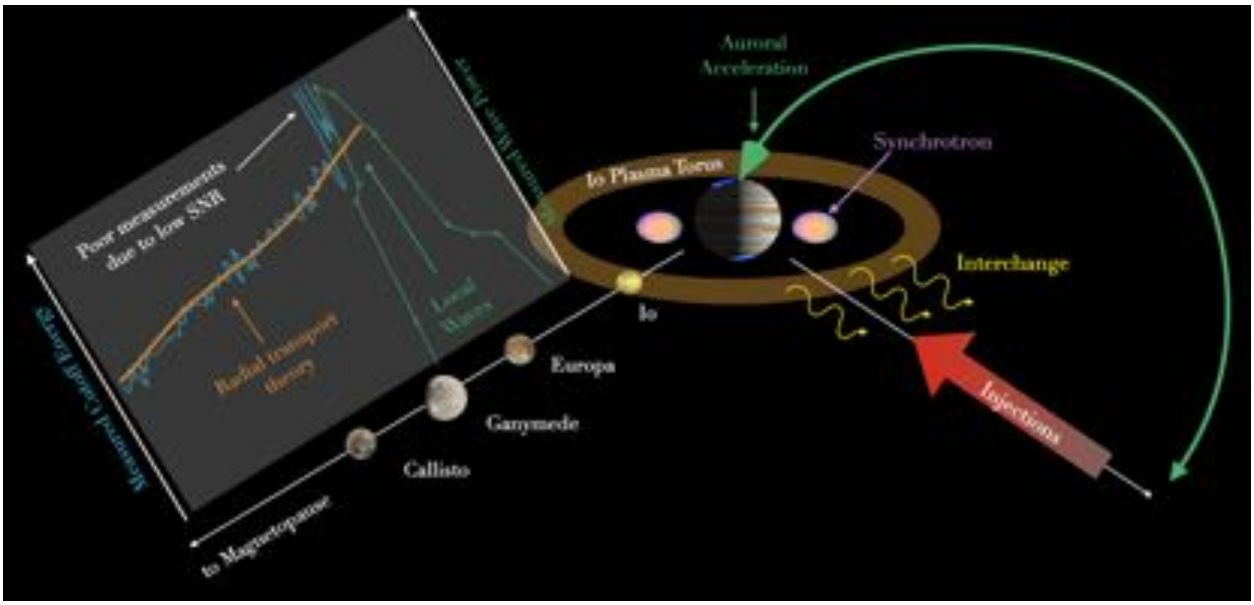

Exhibit 1-5: COMPASS will uncover the processes accelerating charged particles to exceptionally high energies in Jupiter's magnetosphere.

angle-resolved differential 1 MeV to > 50 MeV electron fluxes, 1 MeV to 1 GeV proton fluxes, and 1 MeV/nuc to > 1 GeV/nuc heavier ion fluxes in conjunction with a full spectrum of plasma wave measurements. This is absolutely essential to the success of understanding Jupiter's mysterious radiation belts.

Loss. ***Do precipitation losses to the Jovian atmosphere and collisional losses to moons and ring materials balance and ultimately limit Jovian radiation belt intensities?*** While acceleration and source processes get a lot of attention in radiation belt physics, losses are similarly important because without them, intensities would accumulate indefinitely. As at Earth, Jupiter loses particles via precipitation to the atmosphere, but unlike Earth where losses to the magnetopause are important, Jupiter's standoff distance is located too far away (60-100 RJ) for this to play an important role. Therefore, losses in the inner magnetosphere are likely the critical factors in sculpting the particle distributions. The radiation belt regions along with the 3 innermost Galilean moons, neutral & plasma tori, and rings are all embedded deep within Jupiter's inner magnetosphere (L ≤ 15 RJ). Sparse observations and simulations have shown that wave-particle interactions near Io (e.g., Nénon et al., 2017; Nénon et al., 2018) can locally pitch angle scatter ions into the atmospheric loss cone. Moons can also directly absorb charged particles, which in turn also weather the moons' surfaces, but the efficiency of the process is dependent on where the moon is located at any given time as well as the pitch angle distributions of electron and ions (e.g., Paranicas et al., 2012; Nordeim et al., 2018). Therefore, material-laden magnetospheres such as Jupiter's provide us with a natural laboratory to probe competing processes acting both as sources and sinks. These loss mechanisms (Exhibit 1-6) are expected to have corresponding signatures in both charged particle distribution functions and in the intensity and spectra of remotely sensed X-rays (e.g., Millan et al., 2002; Marshall et al., 2020; Ezoe et al., 2010; Numazawa et al., 2021), but limitations in the existing in-situ energetic particle measurements from Jupiter's inner radiation belts and the lack of close-proximity X-ray observations of the Jovian system, prevent us from reaching concrete interpretations about the significance of different radiation belt loss processes. Additionally, electron and ion losses to Jupiter's atmosphere and moons produce hard (> ~2 keV) and soft (< ~2 keV) X-rays (e.g., Gladestone et al., 2002; Branduardi-Raymont et al., 2010; Bhardwaj et al., 2007; Elsner et al., 2002; Dunn et al., 2017). A major design consideration

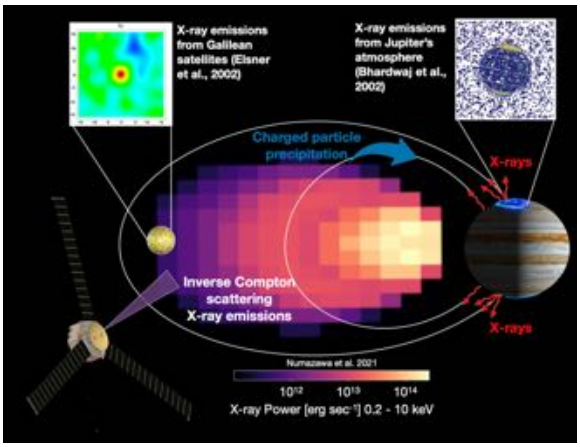

Exhibit 1-6: COMPASS will reveal the loss processes of energetic charged particles in Jupiter's magnetosphere via a combination of in situ and X-ray observations.

for COMPASS is to enable—*for the first time ever*—an unprecedented view of Jupiter's magnetosphere via X-rays. An X-ray imager configured on a Jupiter orbiting spacecraft can achieve ~10^7 more photons over Earth-orbiting assets with unprecedented angular resolution. Jupiter's intense radiation belts necessitate a mission design with long orbital periods; however, remote observing campaigns with X-rays can monitor the dynamics of the magnetosphere via interactions with moons, neutral tori, photons (via inverse Compton scattering), atmosphere, and rings and thus probe timescales unattainable otherwise (Exhibit 1-5). X-ray observations in Jupiter's material-laden environment will reveal the dynamics of high-energy electrons and ions much like energetic neutral atoms have been used to probe the global dynamics of Earth's magnetosphere via ion-only interactions with neutral materials. COMPASS's first science phase is also tailored to enable near-simultaneous X-ray observations of Jupiter's atmosphere connected to COMPASS's magnetic footprint to probe not only correlations, but also causality.

Enabling unknown discoveries. Missions to deep space are typically severely downlink limited and therefore heroic efforts are required to reduce data volume while also ensuring mission success. As a result, high resolution data products are either not employed or severely limited in scope (i.e., region or duration), but we know, all too well, the success stories and discoveries enabled from Earth missions downlinking high-resolution burst data. NASA's Magnetospheric Multiscale (MMS) mission is a prime example of a mission making revolutionary discoveries associated with magnetic reconnection in part because of its combined burst data acquisition and scientist in the loop (SITL) function, where selections are made by experts on the ground based on various parameters of interest. To enable the same discovery-level science that is unprecedented in deep space missions, COMPASS made design considerations (i.e., power, communication, and dedicated downlink phases; see Section 3 and Appendix for more details) that will enable continuous downlink of burst data inside of Ganymede's orbit and selective regions outside. Simulations of Jupiter's magnetosphere (Hao, Sun, Roussos, 2020, see Exhibit 1-7) suggest fine structure within the radiation belts is likely and

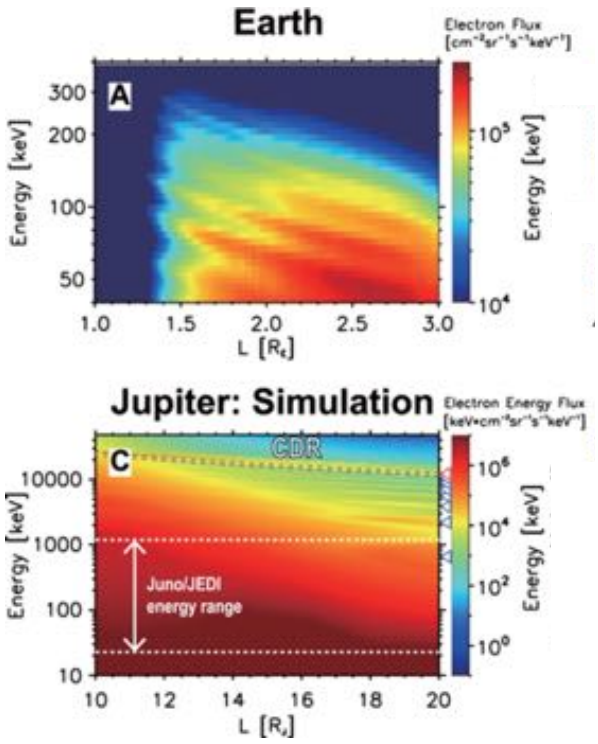

Exhibit 1-7: COMPASS will reveal unknown discoveries by enabling a novel burst data acquisition and downlink plan. Meso-to-micro scale structure can be resolved in Jupiter's radiation belts. In particular, a "zebra-stripe" pattern was revealed by high-resolution measurements in Earth's inner magnetosphere (Hao, Sun, Roussos, et al, 2021).

may be analogous to the so-called Zebra stripes discovered in Earth's radiation belt (Ukhorskiy et al., 2014). **Therefore, by enabling very high-energy data collection and downlink, COMPASS will reveal unknown mesoscale to microscopic processes and physics of the Jovian magnetosphere**. Mission success *does not depend* on downlinking of burst data and as a result this is one descope option that provides cost (i.e., smaller high-gain antenna, lower utilization of power) and complexity (i.e., SITL and operations) savings.

Expanding the frontiers of Heliophysics in the next decade. NASA's Heliophysics community has demonstrated increasing interest in comparative magnetospheric systems. Magnetospheric results from MESSENGER at Mercury, MAVEN at Mars, Galileo and Juno at Jupiter, and Cassini at Saturn have been increasingly in demand and present at magnetospheric conferences and workshops. For the past several years, AGU sessions dedicated to comparative magnetospheric systems have been appearing routinely. The NSF GEM program has a dedicated grant opportunity this year for comparative magnetospheric systems studies. Additionally, NASA Heliophysics has funded multiple studies dedicated to exploring the possibility of a dedicated Uranian orbiter to study the extremely offset and fast rotating magnetosphere embedded in the tenuous but very high Mach solar wind surrounding the outermost planets. Furthermore, the "space weather" of exoplanetary systems and impacts of exoplanetary magnetospheres on habitability of planets orbiting alien stars is trending as a cutting-edge field of cross-divisional, interdisciplinary research. Comparative planetary magnetospheres represent not only a truly cross-divisional field of study entirely centered around fundamental space plasma physics but also an opportune pathway to expand the boundaries of NASA's Heliophysics toward largely unexplored new systems within the Heliosphere (and beyond). COMPASS addresses the long-term science strategy and core STP goal to understand the fundamental physical processes of complex space environments throughout our solar system. To do this we employ a "Cross-disciplinary science strategy that incorporates aspects of heliophysics-planetary and heliophysics-astrophysics goals" (Decadal Midterm Assessment; see finding 6.10). **Therefore, COMPASS will push the frontiers of the entire Heliophysics field by expanding our knowledge beyond Earth and addressing key gaps in our knowledge regarding fundamental space physics processes.**

2. High-Level Mission Concept

2.1 Overview

In support of the Solar and Space Physics (Heliophysics) 2024-2033 Decadal Survey, an experienced team of engineers and scientists led by The Johns Hopkins University Applied Physics Laboratory (APL) have developed a mission concept that implements the science objectives discussed in Section 1. APL utilizes a concurrent engineering laboratory, which fosters real-time interaction between scientists, instrument developers, and flight system engineers. This interaction allows the team to: i) focus quickly on trades and critical factors in the design to arrive at a concept representing a mission point design at Concept Maturity Level (CML) 4, ii) understand trades and development to be conducted in subsequent mission phases, and iii) identification of mission-level risks and mitigations. The result of this process is a well-defined, feasible mission that accomplishes science goals at reasonable cost and with low schedule risk. The mission concept presented here is the result of trade studies that optimized the mission with regard to factors such as science objectives, concept study requirements, Jupiter's space environment and engineering constraints, and risk. **The end result is a CML 4 point solution that demonstrates COMPASS as the recommended STP-class mission concept for exploring Jupiter's extreme magnetosphere.**

The main mission and spacecraft design features include:

- A single spacecraft launched as early as 2030 (2031 chosen as baseline), with alternate launch dates occurring every year, on a ΔV-EGA trajectory to Jupiter with launch energy C3 $\leq$ 52 km^2/s^2

- Earth-pointed, spin-stabilized spacecraft with 1456 kg dry mass, 3086 wet mass at launch, including a 123kg science payload
- Powered through 72 m^2 Roll-Out Solar Arrays (ROSAs) arranged in three wings to provide 500 W (EOL including margin) at Jupiter
- Blowdown monopropellant chemical propulsion system to provide 1500 m/s for a Deep Space Maneuver (DSM) that enables transfer to Jupiter, Jupiter Orbit Insertion (JOI) maneuver, Perijove Raise Maneuver (PRM), and science tour ΔV, as well as propellant for statistical trajectory correction, attitude control of the spacecraft, and deorbit maneuver
- X-band uplink and downlink to provide 230 Gbits of total mission science data return
- Mission Operations Center/Science Operation Center ground systems to perform all functions needs to operate the mission, return data through the Deep Space Network, distribute science and engineering data to the science teams, facilitate SITL, and analyze and archive mission data
- The major mission phases are: 1) launch and interplanetary cruise, 2) capture into the Jovian system, and 3) multi-phased science tour that includes disposal via Jupiter impact. More details are found in section 3.
- Science phases to mitigate radiation risks and maximize science return:
- Science Phase I: A high-inclination phase with perijove (PJ) near Io's orbital distance (5.9 R_J) critical for addressing the science objectives pertaining to particle origins and losses and optimal for novel remote sensing payloads
- Science Phase II: A low-inclination phase with PJ ~ 1.5 R_J. The primary objective in this phase is to make several deep dives into the heart of the radiation belt and synchrotron region near the magnetic equator. This phase is optimal for in situ payloads and akin to NASA's Parker Solar Probe mission, where several deep dives are used to unlock the Sun's mysteries.
- Total Integrated Dose (TID) < 100 krads behind 2.6 cm Al over the full course of the mission
- Cost: $FY22 1.2B including Phases A-F, 50% reserves, and Falcon Heavy Expendable launch vehicle

2.2 Jupiter's Intense Space Environment

COMPASS is intended to explore the extremes of Jupiter's magnetosphere. Along with the typical spacecraft thermal environment, any mission to Jupiter must consider the effects of trapped energetic charged particle radiation on spacecraft systems. This is particularly important for COMPASS as the spacecraft will be making in situ measurements of this environment in regions where the charged particle environment is most severe. Therefore, the COMPASS team prioritized understanding and mitigating radiation effects on the spacecraft and payloads as a major design factor in developing this concept. This consisted of several steps:

- Early linkage of mission design and the charged particle environment. Simplified models of radiation effects on the spacecraft were used as inputs into trajectory trades to optimize the mission return and impacts on spacecraft design.
- Use of surrogate spacecraft design in radiation analyses to optimize shielding mass estimates.
- Validation of standard charged particle models through comparison with more recent models to understand uncertainties and optimize margins to account for these uncertainties.
- Consideration of shielding trades in the spacecraft design to optimize constraints such as: required shielding mass, mitigations for charging effects, spot shielding, shield vaults, etc.
- Consideration for instrument placement to minimize radiation effects on payloads and data quality.

The result of this analysis is a design that assumes a 100 krad Total Ionizing Dose (TID) requirement for electronic components—with shielding used to reduce levels inside electronic enclosures. Shielding, defined here, can take the form of a vault(s) that contains nearly all electronics, with spot shielding implemented where necessary, i.e., for electronics that must reside outside the vault. In this concept, we provide conservative mass estimates for shielding that we expect will encompass not only the current design, but future designs as the concept matures. Note that many components are available that can withstand higher TIDs, e.g., ratings up to 300 krad, therefore it is reasonable to rely on spot shielding lower TID components to reduce the overall shielding mass. Exhibit 2-1 illustrates a surrogate spacecraft and data processing unit (DPU) used in a 3-dimensional radiation model. We designed the COMPASS shielding to the GIRE/Grid3 model - an industry standard for radiation analysis (e.g., de Soria-Santacruz et al., 2016) – under the standard assumption of shielding through spherical shells. Exhibit 2-1 shows how dose can be reduced through increased shielding. It can be seen that

1700 mil of Al are needed to keep 100krad parts within specification and 1000 mil for 300krad. Exhibit 2-1 also illustrates how the dose accumulates over the various orbits. Our assumptions are very conservative because there are various reasons why the actual dose can be expected to be lower. The state-of-the-art physic-based model JOSE/Salammbô model (Nénon et al., 2017, 2018) is predicting doses that are 60% and 50% lower at 100 and 600 mil of shielding, respectively. Also, the assumption of a spherical shell neglects shielding from the spacecraft body. When assuming a relatively exposed box with 100 mil Al shielding on an approximation of the COMPASS spacecraft (we used IVO in this case) on a COMPASS orbit, we find reductions of 30-50%, depending on the location within the box.

Further reductions are possible through selection of the shielding material. While Al yields the highest reduction behind 100 mil, tungsten can reduce dose by additional ~50% at a thickness equivalent to 1000 mil Al (see appendix). In combination, all these effects might reduce the dose by an order of magnitude, which provides ample margin.

There are a number of additional considerations for the Jovian environment. For example, the proton component of Jupiter's radiation belts is expected to require a thick cover-glass (500 um CMG) for the solar arrays in order to prevent unacceptable degradation to their performance. For Spectrolab XTJ Prime solar cells (that approximate the planned Redwire ROSAs) with 500 um CMG we expect a charged particle fluence equivalent to of 1.17×10^{15} (1 MeV electrons)/cm^2. This fluence will lead to roughly a 25% degradation for solar cell maximum power at end of life. Our solar cells were scaled accordingly.

All of these effects, while challenging, can be successfully mitigated with a rigorous systems engineering that includes: trajectory design, shielding mass allocation, electronic parts selection, design decisions, and test and analysis for verification.

2.3 Planetary Protection

Europa is of significant interest because of the processes that may lead to forms of chemical evolution or the origin of life, and any

Ray-tracing transport modeling for semi-realistic s/c

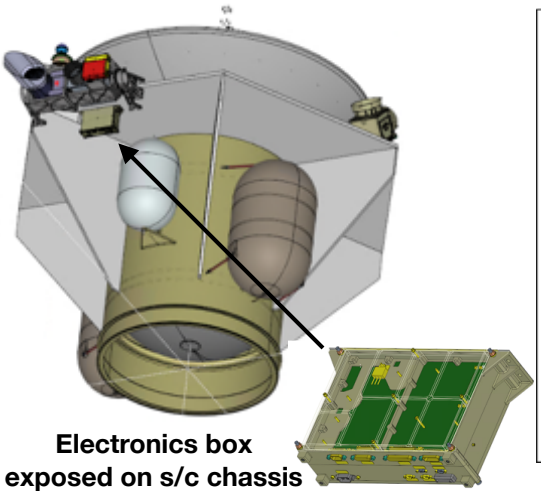

Electronics box exposed on s/c chassis

TID vs. Depth accumulation over COMPASS's Mission

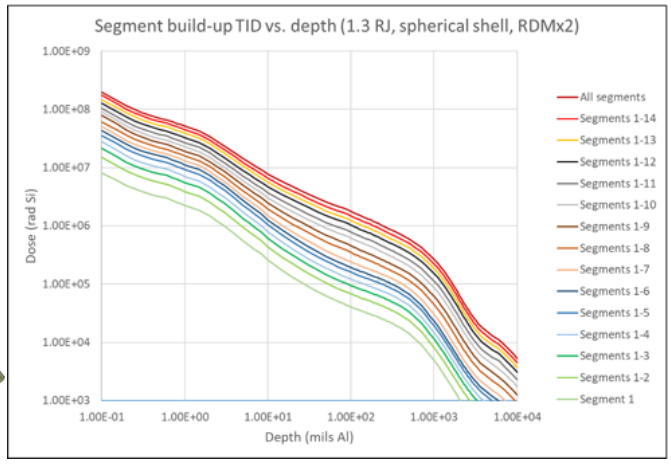

Exhibit 2-1: Ray-tracing transport modeling with semi-realistic surrogate s/c & electronics box (left panel). TID vs. Depth accumulation over the prime COMPASS mission for different shielding thicknesses. It can be seen that dose falls quickly at large thicknesses. "Segments" refer to ranges of orbit numbers. Total TID behind 100 mils Al over all orbit segments is ~1.8 Mrad, accounting for the standard radiation design margin (RDM) of a factor of 2. The actual shielding will be ~10 times thicker and reduce dose to ~100 krad at EOL.

contamination could severely compromise future investigations. For that reason, flyby and orbiter missions to the Jovian system much take the necessary precautions to avoid collision. We show in section 3.12, that the COMPASS tour design carefully considers planetary protection guidelines and disposes the spacecraft into Jupiter. Key aspects and conclusions: COMPASS poses little-to-no risk to Europa concerning planetary protection due to careful mission design ensuring no intersection between COMPASS and Europa orbits prior to Jovian atmospheric entry at end of mission (see further details in Section 3.11).

2.4 Technology Maturity

The team assessed Technology Readiness Levels (TRLs) for spacecraft subsystem elements and instruments in the development of the COMPASS concept and it was determined that **this mission can be executed with very little technology development since all components of the spacecraft included in the design are at TRL 6 or higher.** The instruments included in the concept payload all are based on previously flown instruments that may not represent the state-of-the-art at the time of mission development, but would allow the mission to be flown now without technology development. That being said, technology development areas that would enhance the science return of COMPASS are described in the Appendix. Instrument and subsystem TRL assessments are included in the detailed flight systems discussion in Section 3.

2.5 Key Trades

The study team assessed options for all major design decisions and selected the best approach for the mission concept using a combination of mission performance requirements and engineering judgement of the technical benefit, cost, schedule, and risk trade-offs. Major system and subsystem design decisions are described in Exhibit 2-2.

Area	Trade Study	Results/Rationale
Data Return	Antenna size, RF power, frequency band, data collection plan	• High data collection rate in Phase 2 of science mission drives required static, non-deployable HGA size and RF power. • Ka-band system requires tight pointing requirements that may not be achievable. X-band chosen to reduce propellant needed and burden on attitude control.
Attitude Control	3-axis vs spin stabilized control. Thruster control vs reaction wheels	• Spin stabilized control chosen to reduce system complexity. 3-axis mode not needed to complete science objectives. Spinning is required to complete science objectives. • Reaction wheels not needed for control as spin-stabilized system is passively controlled.
Solar Arrays	Rigid solar arrays vs Roll-Out Solar Arrays (ROSAs)	• ROSAs selected due to packaging constraints in launch vehicle fairing. • Three panel design chosen for ease in balancing the spinning spacecraft.
Trajectory	Multiple options for trajectory in primary science phases	• Trajectory chosen to minimize radiation exposure and meet science objectives and required measurement locations. • Highest radiation exposure moved to last orbits to maximize probably of success.
Launch Vehicle	Multiple options	• Only SpaceX Falcon Heavy Expendable meets requirements for spacecraft mass. • 5m fairing chosen to accommodate spacecraft design constraints.

Exhibit 2-2: COMPASS key mission design trade matrix

3. Technical Overview

3.1 Payload Description

The COMPASS payload design comprises ten instruments accommodated on the spacecraft. Each instrument is based on a high-heritage representative sensor from a previous mission such as Juno, Van Allen Probes, and Europa Clipper with substantial additional shielding mass allocated to the instruments, as necessary. Section 3.2 explores potential trades that could be implemented via development and/or augmentations to the representative heritage instruments that could mitigate radiation effects without the need for such significant shielding mass. Exhibit 3-1 gives the COMPASS payload

Exhibit 3-1: Payload Resource Table Summary

		Mass				Power		
Instrument	**#**	**CBE total (kg)**	**Addt'l Shielding (kg)**	**Cont.**	**MEV (kg)**	**CBE total (W)**	**Cont.**	**MEV (W)**
Thermal Plasma Detector (TPD) †	2	14.0	0.0	10%	15.4	10.0	10%	11.0
Suprathermal Particle Detector (SPD) ††	1	9.2	8.0	10%	19.0	9.5	15%	11.0
Energetic Particle Detector (EPD)	1	6.4	3.0	10%	10.3	3.1	15%	3.6
Relativistic Particle Detector (RPD)	1	13.4	2.7	20%	17.8	6.2	15%	7.1
Ultra-relativistic Particle Detector (UPD)	1	9.2	1.8	10%	13.3	13.2	25%	16.5
Fluxgate Magnetometer (FGM)	2	1.6*	0.0	10%	1.8*	4.2	15%	4.8
Search Coil Magnetometer (SCM)	1	7.1*	0.0	10%	7.9*	1.0	15%	1.2
Electric Field Waves (EFW)	1	13.2	0.0	10%	14.6	15.4	15%	17.7
X-Ray Imager (XRI)	1	10.0	5.0	10%	16.5	6.0	15%	6.9
E/PO Camera (EPOC) †††	1	3.7	2.2	10%	6.5	2.4	15%	2.7
Payload Totals		**87.8**	**22.7**		**123.1**	**71.0**		**82.5**

Footnote legend:
†Descope option: single sensor, little impact to science → trade: pitch angle vs. corotation flow coverage
††Descope option: remove sensor, impacts science tied mostly to particle origins (see MR1 in STM) & creates narrow energy gap of ~30 keV between TPD and EPD for electron & proton energies
†††Descope option: remove completely, no impact to science
**Not including shared 2.6 kg boom*

mass and power table and Exhibit 3-2 is a fold out containing the payload configuration on the spacecraft, FoVs, location inside bays with close out panels and representative heritage instruments. Instruments are grouped into particles, fields, and imaging suites. Next, we provide short descriptions on the various science instruments, but more details can be found in the Appendix.

Thermal Plasma Detector (TPD). The TPD instrument measures energy and angular distributions of thermal ion and electron plasma from ~10 eV/Q to ~10 keV/Q to help assess the origins, acceleration, and losses in the Jovian magnetosphere. The TPD sensors in the notional COMPASS payload are modeled after the PIMS instrument currently in development for the Europa Clipper mission (Grey et al., 2018). The PIMS instrument, a Faraday cup design, was chosen because of its high tolerance for extreme radiation environments and significant shielding as built for Europa Clipper. Two sensors, orthogonal to each other, are implemented in the baseline payload to help ensure observability of the co-rotation vector of the magnetospheric plasma is maximized throughout the COMPASS orbit.

Suprathermal Particle Detector (SPD). The SPD instrument measures the energy, angular, and compositional (mass and charge-state) distributions of suprathermal (few keV/Q to 100s keV/Q) ions to determine the origins and acceleration processes in the Jovian magnetosphere. The SPD sensor in the notional COMPASS payload is modeled after the CHEMS instrument, an electrostatic analyzer paired with a time-of-flight subsystem, flown on the Cassini mission to Saturn (Krimigis et al., 2004) and similar instruments have been used recently, e.g., Owen et al. (2020). For COMPASS, the CHEMS instrument, which was flown in a much less severe radiation environment at Saturn, will require substantial additional shielding mass to protect its radiation-sensitive microchannel plate detectors (Exhibit 3-1).

Energetic Charged Particle Detector (EPD). The EPD instrument measures the energy, angular, and mass composition distributions of energetic (10s keV to > few MeV, exact energy range is species dependent) ions and electrons to determine the acceleration and loss processes at play in the Jovian radiation environment. The EPD sensor in the notional COMPASS payload is modeled after the JEDI instruments, a time-of-flight-based design with solid-state energy

Exhibit 3-2: COMPASS Science Payload & Configuration

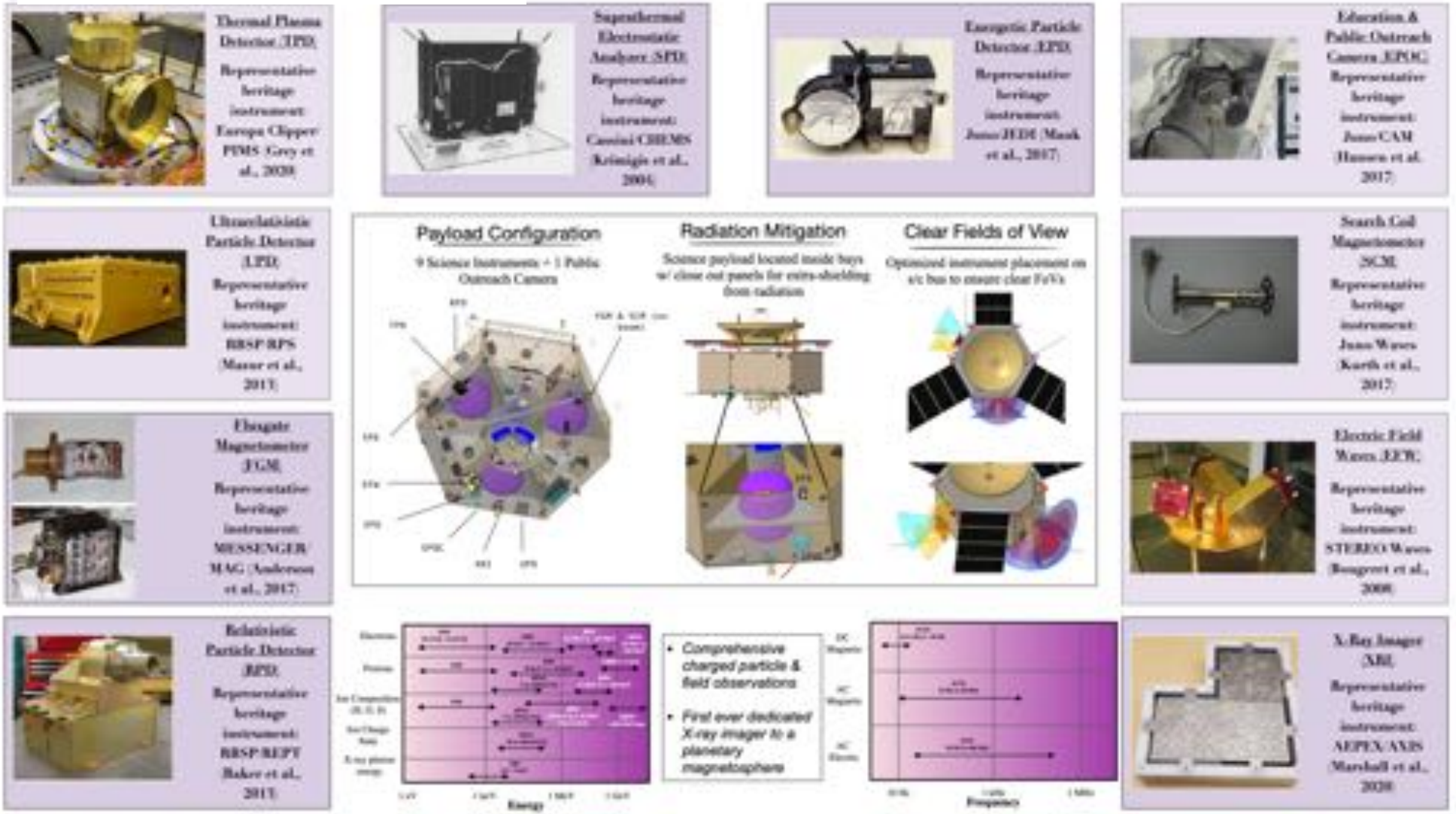

detectors, flown on the Juno mission currently orbiting Jupiter (Mauk et al., 2017). For COMPASS, the JEDI instrument will only require modest additional shielding mass.

Relativistic Particle Detector (RPD). The RPD instrument measures the energy and angular distributions of relativistic (~1 to 10s of MeV) ions and electrons to determine the acceleration and loss processes at play in the Jovian radiation belts. The RPD sensor in the notional COMPASS payload is modeled after the REPT instrument flown on the Van Allen Probes mission to explore the radiation belts at Earth (Baker et al., 2012). For COMPASS, the REPT instrument – a solid-state telescope with stacked SSDs - will only require modest additional shielding mass.

Ultra-relativistic Particle Detector (UPD). The UPD instrument measures the energy and angular distributions of ultra-relativistic (~10 to 10,000s MeV/nuc) protons & heavier ions and (~8 MeV to > 50 MeV) electrons to make the first in-situ comprehensive measurement of the highest-energy populations in the most extreme radiation environment in the solar system. The UPD sensor in the notional COMPASS payload is a slightly modified version of the RPS instrument flown on the Van Allen Probes mission to explore the radiation belts at Earth (Mazur et al., 2013). For COMPASS, the RPS instrument – a solid-state telescope paired with a Cherenkov radiator - will require minimal additional shielding mass.

X-Ray Imager (XRI). The XRI instrument measures the energy distribution of X-ray emissions (~0.5 to 10 keV) via line-of-sight images of the Jovian radiation belts as well as precipitation into the planet's atmosphere. The energy range is chosen to distinguish soft and hard X-rays. The XRI instrument in the notional COMPASS payload is based on the AXIS instrument currently in development for flight on the AEPEX mission at Earth (Marshall et al., 2020). For COMPASS, the XRI instrument – an array of solid-state detectors with coded and pinhole apertures – will require significant additional shielding mass.

Fluxgate Magnetometer (FGM). The FGM instrument measures the three-dimensional DC magnetic field, up to 128 Hz sampling, to help assess the loss processes, particle pitch angle, and plasma dynamics in the Jovian environment. The FGM instrument in the notional COMPASS payload is based on the MAG instrument flown on the MESSENGER mission to Mercury (Anderson et al., 2007). For COMPASS, the two MAG sensors – low-noise, tri-axial, fluxgate instruments – will be mounted in a "gradiometer" configuration on a single 2.6-m-long boom to ease engineering burden of magnetic cleanliness requirements. FGM requires no additional shielding mass, as the instrument electronics will be accommodated in the spacecraft's central vault.

Search Coil Magnetometer (SCM). The SCM instrument measures the three-dimensional AC magnetic field, up to 60 kHz sampling, to help assess the wave dynamics and loss processes at play in the Jovian magnetosphere. The SCM instrument in the notional COMPASS payload is based on three copies of the search coil antenna of the WAVES instrument flying currently on the Juno mission at Jupiter (Kurth et al., 2017). For COMPASS, the tri-axial SCM sensors – high-permeability cores within a bobbin holding thousands of turns of copper wire – will be mounted on the same 2.6-m-long boom as the FGM sensors and require no additional shielding mass, as the instrument electronics will be accommodated in the spacecraft's central vault.

Electric Field Waves (EFW). The EFW instrument measures the three-dimensional AC electric field to help assess the wave dynamics and loss processes at play in the Jovian magnetosphere. EFW will be sampled up to 6 MHz to resolve the upper hybrid line for accurate plasma density determination and down to lower Perijove altitude ($L < 1.02\ R_J$). The EFW instrument in the notional COMPASS payload is based on the WAVES instrument flying currently on the STEREO mission observing the Sun (Bougeret et al., 2008). For COMPASS, the three EFW antennae – 6-m beryllium-copper (BeCu) stacers – will require no additional shielding mass,

as the instrument electronics will be accommodated in the spacecraft's central vault.

3.2 Radiation Effects on Science Payload

Science instrumentation on previous Jupiter missions always struggled with low signal-to-noise (SNR) in the harshest regions of Jupiter's magnetosphere. For example, the high intensities of very energetic charged, i.e., penetrating backgrounds, found near and inside of Europa present challenges to charged particle instruments (e.g., Kollmann et al., 2022). Therefore, SNR will be a key design driver for the COMPASS payload. Here, we perform a preliminary analysis of SNR on a few representative instruments and demonstrate methods that can be easily implemented to reduce backgrounds. More details on SNR can be found in the Appendix.

SNR is calculated using worst-case spectra—L-shell of 2—in Jupiter's radiation belts based on the JOSE/Salammbô physical model (Nenon et al., 2017, 2018). The signal is calculated based on the input spectrum and the nominal instrument response. To estimate the noise, we used GEANT4 to determine how the input spectra of incident protons and electrons manifest as proton, electron, and, gamma spectra behind instrument shielding using tungsten with different thicknesses. To estimate the measured backgrounds, we perform a simple forward model that includes species and energy dependent measurement efficiencies based on heritage designs. Exhibit 3-3 shows detailed SNR results for two scenarios: i) ion measurements using a EPD-like instrument and 2) electrons measurements with a RPD-like instrument.

The results in Exhibit 3-3 illustrates there are somewhat straightforward techniques that can be implemented to increase SNR on heritage instruments without necessitating major design changes. These options can also present the basis for trade studies, e.g., mass (shielding) against complexity (adding additional coincident detectors). In general, the simplest solution is to increase the shielding mass. For example, we find that an equivalent of 6.7 mm of tungsten (W)—

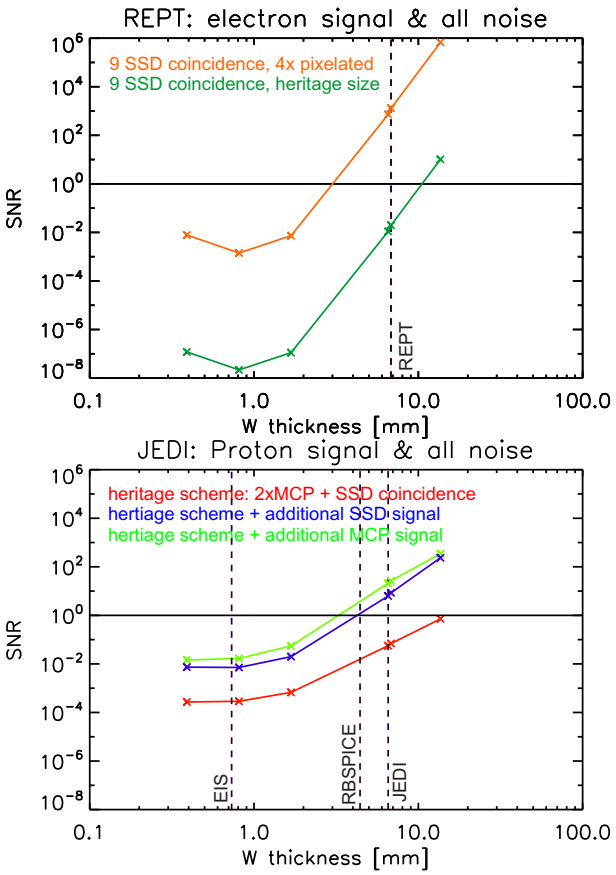

Exhibit 3-3: COMPASS aims to address raidation contamination issues by implementing straighforward mitigations to heritage instruments. Expected signal-to-noise (SNR) ratio as a function of shielding thickness for 0.2 MeV protons measured by a Juno/JEDI-like instrument (COMPASS/EPD) and 15 MeV electrons measured by a RBSP/REPT-like instrument (COMPASS/RPD).

used by recent missions such as Juno/JEDI and RBSP/REPT—can be simply doubled to achieve a desired SNR in Jupiter's harshest regions. An alternative to shielding is adding additional coincidence detectors into the instrument to reduce backgrounds via logic in the flight software. JEDI measures ions using a combination of two MCPs and one SSD detector. Where MCPs are typically used in time-of-flight based instruments for measuring timing pulses triggered by secondary electrons. Adding another MCP allows additional time pulses for redundancy and increases SNR by 3 orders of magnitude (see bottom panel in Exhibit 3-3). REPT measures electrons using up to nine SSD detectors arranged in a stack. The right panel in Exhibit 3-3 illustrates that even this high number

of coincidence detectors can be insufficient. The reason for this is that the detectors are running in saturation; that is to say, particles reach the detectors faster than they can be counted. One possible solution is to either reduce the detector size or pixelate the detectors. The latter essentially maintains sensitivity in low count environments and avoids saturation in high count environments. In summary, shielding can provide a straight forward means in reducing backgrounds, but it can add significant mass to the overall payload (see Exhibit 3-1); however, other techniques such as adding additional detectors or pixelating them can significantly improve the outcome, while not gowning the mass significantly. COMPASS, and other missions that want to measure extreme environments, can benefit from future research and development into background mitigation techniques. We leave further details about instrument backgrounds for the Appendix.

3.3 Flight System

The COMPASS flight system consists of an orbiting spacecraft and fits within the 5-m diameter of SpaceX's Flacon Heavy Expendable fairing. No staging or other elements are required to meet the mission science objectives. All functions are incorporated on the spacecraft to meet the science objectives, including X-band communication functions with Earth, orbital maneuvers, a stable platform for the science measurements, and powering of all systems. All electronics subsystems are redundant to accommodate the 10-year mission design life. Overall, COMPASS is a spin-stabilized hexagonal spacecraft with maximum dry mass of 1,456 kg. The spacecraft bus is 4.6 m across and 3.4 m high, with three Roll-Out Solar Arrays (ROSAs) mounted on three of the faces, as shown in Exhibit 3-4. Instruments and spacecraft electronics are mounted in the remaining three bays. Exhibit TBD provides the spacecraft block diagram (add block diagram and s/c pictures). Spacecraft characteristics are given in Exhibits 3-2, 3-4 & 3-5.

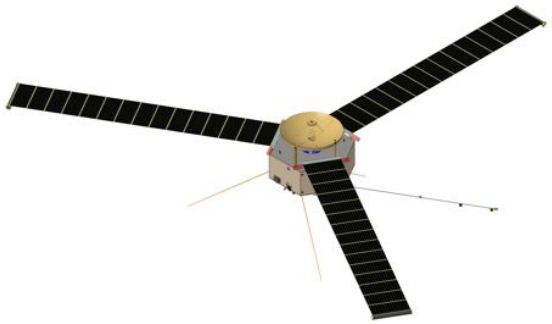

Exhibit 3-4: COMPASS spacecraft structure builds off heritage from IVO & IMAP. Shown is spacecraft structure with roll out solar arrays, high gain antenna shown, magnetic field boom, electric-field stacers, and bay with instruments located

3.4 Spacecraft Structure

The COMPASS spacecraft will be built with an aluminum honeycomb structure, modeled on the patterns of the Io Volcano Observer (IVO) and Interstellar Mapping Probe (IMAP, McComas et al., 2018). This design baselines a hexagonal spacecraft with a central cylinder. Three fuel tanks will be located in alternating bays, with three pressurant tanks in the central cylinder. Instruments are located in the alternating three bays from the fuel tanks, with electronics boxes and other bus components spread throughout all six bays, as space permits (see Exhibit 3-5).

All six external bays have aluminum honeycomb closeout panels. These serve two functions, providing both structural support for the bays as well as additional radiation protection for the electronics boxes, subsystems, and instruments inside. Most instruments are located just inside these closeout panels, on the top and bottom decks or on the radial panels, with small cutouts in the closeout panels for fields of view outward from the spacecraft. Instruments are not mounted directly to the closeout panels, to preserve the ability to install and remove these panels as easily as possible during I&T.

Solar arrays are modeled after the Roll Out Solar Arrays (ROSAs) recently flown on DART and the International Space Station. Three such arrays are body-mounted to the top deck, to deploy radially away from the spacecraft. The spacecraft structure is sized to be as large as possible while fitting in the 5-m SpaceX Falcon Heavy fairing, so that each structure "face" will

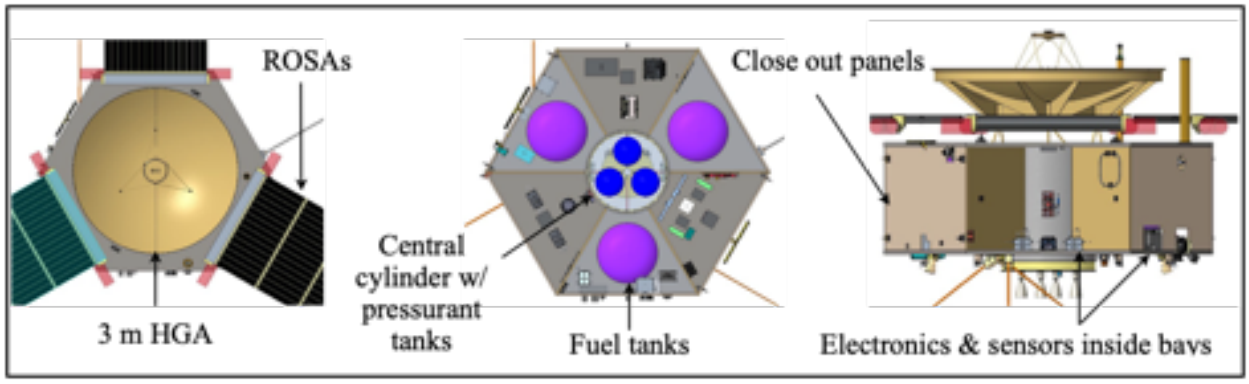

Exhibit 3-5: Spacecraft structure highlighting the HGA, ROSAs, fuel tanks, pressurant tanks, close out panels, and sensor arrangement inside bays.

be as large as possible, thus giving the solar arrays the maxi mum possible width.

This spacecraft will require several deployable mechanisms. Each of the three ROSAs will deploy from the spacecraft top deck, as well as a double-hinge magnetometer boom deployment from the bottom deck. All other deployments will be internal to specific instruments. Note, all deployments occur prior to arrival to the Jovian system.

3.5 Propulsion

COMPASS will use a pressurized monopropellant hydrazine system, as shown in Exhibits 3-5 & 3-6. The hydrazine will be stored in three identical, qualified, NGIS 80451 diaphragm tanks each capable of carrying 451 kg of propellant for a total of 1,456 kg. This will provide 1500 m/s of ΔV to a 3,230 kg launch mass. Helium pressurant will be stored in three additional COPV tanks (i.e., NGIS 80436) and will allow the system to provide a constant feed pressure to the thrusters. For large ΔV burns and time sensitive maneuvers, COMPASS will incorporate four 100-lbf class thrusters, notionally the Aerojet MR-104A/C. Four are needed to handle the propellant throughput required. The mission will have the option of firing a single engine or two at a time depending on the maneuver requirements. An additional four 5-lbf Aerojet MR-106E thrusters will be used for steering during large burns and twelve 1-lbf Aerojet MR-111C thrusters for ACS. The system, shown in Exhibit 3-6 will be procured as a whole from a subcontractor. No qualification testing is required for any component in the baseline propulsion system. Each component has flight qualified options, most of which have been flown on heritage spacecraft.

A dual-mode system was also considered for COMPASS. The use of dual mode main engines, rather than the four 100-lbf thrusters baselined, would reduce the total propellant load to 1300 kg while maintaining the same spacecraft dry mass. However, because the COMPASS structure design and launch vehicle are capable of carrying the heavier propellant load, the monoprop system was baselined. In COMPASS's case, the monoprop system's simplicity of design and usage, as well as significantly lower cost, wins against the additional performance provided by the more complex dual mode system. A monoprop baseline also enables the option of switching to a dual mode system to gain that

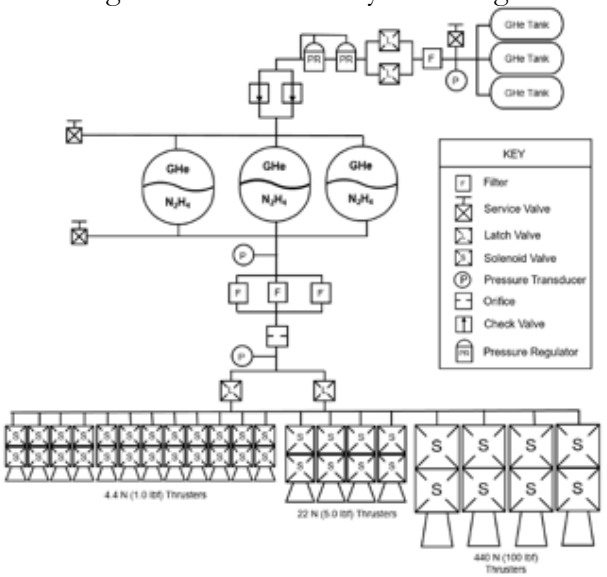

Exhibit 3-6: COMPASS propulsion system block design.

added performance and reduce the propellant load if mission requirements change (increased dry mass or ΔV, reduced launch vehicle capability, etc.). In addition, since the dual mode tankage would be smaller in volume, the fundamental design of the spacecraft would not need to be altered to accommodate it.

3.6 Electrical Power

The Electrical Power Subsystem (EPS) uses a high-efficiency, peak-power-tracking, solar-array/battery architecture with significant heritage from PSP and other APL missions. As shown in the block diagram (Exhibit 3-7), solar array (SA) power is processed by buck-topology dc/dc converters within the power system electronics (PSE) box, which regulates SA power and battery charging. The battery-dominated power bus is maintained within a voltage range of 22 to 35 V.

Three Roll-Out Solar Array (ROSA) wings, provided by Redwire/Deployable Space Systems, provide primary power of 500 W with a total of 72 square meters of flexible blanket area. To accommodate the charged particle radiation environment, the solar cell assemblies incorporate 500 um (20 mils) coverglass. Backside shielding provided by the standard power modules that comprise the array is taken into account in the radiation degradation estimates. Radiation testing, and low-irradiance, low-temperature and room-temperature characterization and screening is baselined for the solar cells, which are optimized for this environment.

The PSE design has been flight-proven on PSP and DART, and similar slices are used on COMPASS. Four parallel buck converters process SA power. In the unlikely event of a buck converter fault, the remaining three can accommodate the load. Local, autonomous, SA electrical peak-power tracking within the PSE reduces burden on the S/C processor and improves subsystem testability. Peak-power tracking also allows all SA strings to have the same quantity of series cells, which optimizes the power available under worst-case conditions. The PSE performs constant-current, constant-voltage

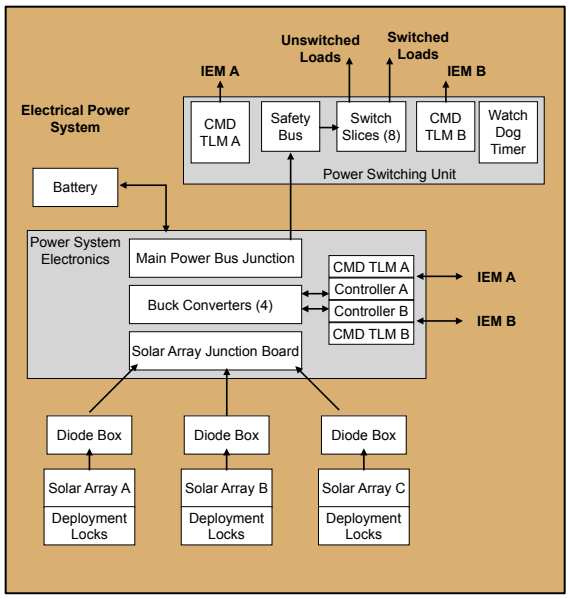

Exhibit 3-7: COMPASS electrical power subsystem block diagram.

battery charging with default limits that can be modified by command for contingencies. Three solar array diode boxes serve as the interfaces between the SA wings and the PSE, with diode isolation of each string of cells and power bussing. The power switching unit (PSU) contains individual power services for distribution to S/C components. The PSU receives power from the PSE and provides unswitched, switched, and pulsed power services. PSU circuits have significant heritage from distribution units flown on PSP, DART, and Van Allen Probes. Individual load currents are included in telemetry. Safety busses controlled by S/C separation signals feed power to services for propulsion thrusters, RF transmission, and mechanical deployments to meet range safety requirements. A 42-amp-hour capacity lithium-ion battery supports launch and peak loads. The battery, procured from ABSL, is similar to the design flown on PSP but is larger in capacity.

3.7 Avionics

The avionics subsystem manages the spacecraft's command and data handling (C&DH) system. The low-power avionics, uses techniques and design approaches proven by MESSENGER, STEREO, New Horizons (NH), Van Allen Probes, and PSP, coupled with radiation mitigation strategies flown on Van Allen Probes,

enable APL's low-risk C&DH implementation. The key components of the avionics subsystem, are radiation-shielded integrated electronic modules (IEMs), distributed remote interface units (RIUs), and a radiation monitor (RadMon). The IEMs each combine C&DH and mass memory storage. The IEMs are based on the PSP modular avionics design and leverage those circuit cards to provide a high-heritage design. The SBCs provide 256 MB of SDRAM, 8 MB of MRAM, and 64 Gb of flash memory (Exhibit 3-8) with the UT700 100 MHz processor. Additional PSP heritage-based components include a pair of Spacecraft Interface Cards (SCIF), two Thruster/Actuator Cards (TAC), two Instrument Interface Cards (IIF) with Solid State Recorders (SSR), and two DC/DC converters. Two strings of Remote Interface Units (RIUs) provide a total of 120 analog channels for temperature sensing. The engineering RadMon is an APL-designed radiation monitor for Europa Clipper, and it will monitor total dose and dielectric charging in real time. In addition, RadMon benefits the mission by assessing the radiation health of the spacecraft.

Exhibit 3-8: COMPASS C&DH table

Command & Data Handling	
Flight element housekeeping data rate	1 kbps
Data storage capacity	64 Gb
Maximum storage record rate	600 kbps
Maximum storage playback rate	500 kbps

3.8 Guidance & Control

COMPASS is predominately a passive spin-stabilized spacecraft, drawing inspiration from IVO and Juno. Nominally, the spacecraft maintains a constant spin about its fixed antenna boresight axis at a rate of 2 rotations per minute (RPM), keeping its antenna pointed toward Earth for telecommunications. This spin motion also allows for spacecraft to sweep its instrument suite to get a complete view of its environment, which is a top-level mission requirement. The spin rate was chosen to provide stability while keeping propellant usage during precession maneuvers at an acceptable level, while providing a suitable scan rate to the instruments. This passive mode will be routinely perturbed via thruster firings to precess the spin axis to maintain line of sight communications to Earth. On the few occasions where large modifications to the trajectory are required (Deep Space Maneuver (DSM), Jupiter Orbit Insertion (JOI), Perijove Raise Maneuver (PRM)), the spacecraft will precess the spin axis to align its main ΔV thrusters in the direction of the required thrust vector, and perform the burn maneuver while spinning for stability. For smaller Trajectory Correction Maneuvers (TCMs), the spacecraft may choose to maintain its Earth-pointing posture and pulse the smaller thrusters to achieve the desired correction to minimize propellant consumption. Thruster firings will excite spacecraft nutation and solar array motions that will dampen out over time, accelerated by two nutation dampers.

Due to its spinning nature, COMPASS does not require continuous active attitude control. However, providing better than 0.25° attitude knowledge for the instruments requires a sufficient level of sensing. This is achieved through a pair, for redundancy, of Sodern Hydra TC Star Trackers and an internally redundant Northrop Grumman Scalable Space Inertial Reference Unit (SSIRU), containing four (4) gyros and four (4) accelerometers. The star trackers are mounted with boresights 15° off the spin axis to reduce the perceived rotational rate to ensure a robust star lock and thus would provide 6 arcsecond accuracy to their boresights and 50 arcsecond accuracy about the boresight (3δ). The SSIRU allows for closed loop trajectory adjustments as well as provides rate information that can be integrated to provide attitude information for situations where the star trackers are physically obstructed or momentarily affected by radiation. Two Sun Sensors manufactured by Redwire provide additional position information relative to the Sun and are primarily used for safe mode; however, precession maneuvers and TCMs may utilize the Sun pulse from these sensors to properly phase thruster firings if it is determined that the on-board attitude knowledge is degraded and the Sun vector is separated from the spin axis. This thruster control method using Sun Sensors has been used many times on-orbit, including the Van Allen Probes and planned for

IMAP. All components were chosen for the purpose of establishing the baseline subsystem design. The selection of the actual components will go through the standard competitive procurement process for commercial-off-the-shelf (COTS) flight hardware several years prior to launch.

3.9 Flight Software

The Flight Software (FSW) subsystem (Exhibit 3-9) can be built with heavy reuse from legacy software that provides a reused common set of applications for command management, telemetry, formatting, data recording and playback, autonomy, file management, and application scheduling that can be used with minimal changes/updates. A description of the flight software design and heritage is given in Exhibit 3-9. Some unique components would be required for a mission like COMPASS, but none that present any insurmountable challenges from those normally solved during the FSW development for current missions. No major showstoppers or risks have been identified for this mission from a FSW perspective.

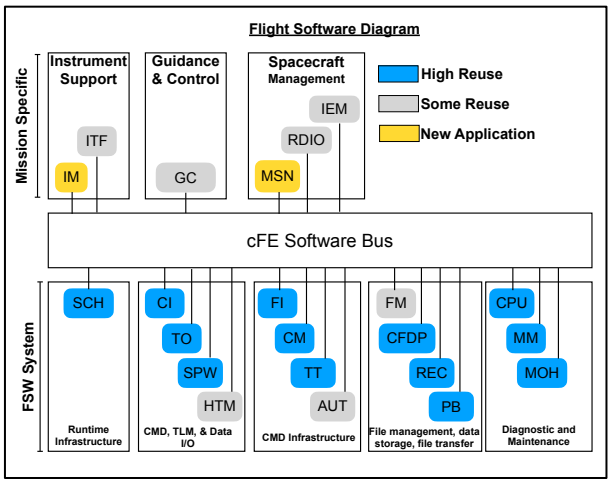

Exhibit 3-9: The FSW Architecture Concept built on cFE applications. As shown, nearly all applications in flight software system can be reused entirely, while there are some mission specific apps that will be customized for COMPASS, as is typical for any mission.

3.10 Communications

The telecommunications subsystem (Exhibit 3-10) characteristics are driven by the data volume required during the shortest Science Phase 2 orbit durations, down to 16.7 days. The most prominent result of this is the 3-m HGA, mounted on the aft of this spinning spacecraft. Science data downlinking at X-band from a 65-W TWTA for 8 hours a day, 5 days a week is sufficient to complete the transfer of 1.37 GB of compressed data plus a 50% margin at Jupiter's maximum Earth range of 6.45 AU. All communication is through NASA's Deep Space Network (DSN). The science data downlinks

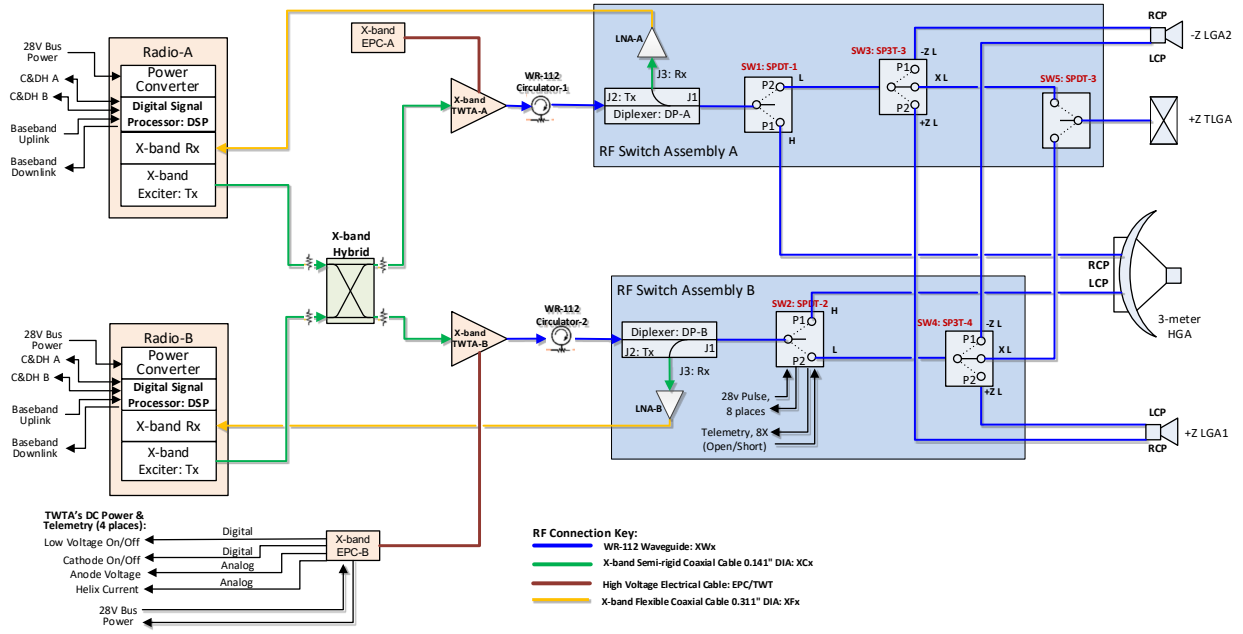

Exhibit 3-10: COMPASS telecommunications subsystem

require use of a single, 34-m DSN station and HGA pointing accuracy maintained to within ±0.4 degrees. Use of the 70-m DSN station will increase our downlink allocation and enhance science return. Emergency operations at Jupiter range would require a 70-m DSN station if pointing cannot be maintained.

Key trades defined the telecommunications subsystem. First, NASA directs all new missions to baseline Ka-band downlinks, and indeed that does inherently offer more gain. However, it also adds mass and complexity and, more critically, a pointing accuracy requirement of ±0.1 degree or better which is not feasible for this spin-stabilized spacecraft. Second, as the spacecraft is more power constrained than mass constrained, the 3-m HGA was selected to minimize the TWTAs' demand for larger solar arrays.

Two opposing (fore and aft) low-gain antennas (LGAs) and a toroidal low-gain antenna (TLGA) compliment the HGA to provide coverage for all mission phases. During launch and early operations (LEOP) and the Earth gravity assist (EGA) maneuver, the LGAs are sufficient to support downlink throughput of up to 1 Mbps. A deep-space maneuver at approximately 4.3 AU Earth range is covered by the TLGA (which provides a donut-shaped pattern perpendicular to the spin axis) as the Earth is visible at an angle 90 degrees off the spin axis. During this maneuver, only minimal data rates of 7.8 bps for uplink and 10 bps for downlink are supported. During Jupiter Orbit Insertion (JOI) and Perijove Raise Maneuver (PRM), the spacecraft is off-pointed by 50 degrees and command and telemetry links cannot close with sufficient margin, however, beacon tones are still available to indicate status.

Telemetry, tracking, and control (TT&C) is provided through redundant APL Frontier Radios. A next-generation version is under development to replace the current "Classic" version and would be available by the time COMPASS is underway. The Frontier Radio Classic has significant flight heritage on NASA's Van Allen Probes, Parker Solar Probe, and Double Asteroid Redirection Test (DART) missions as well as the United Arab Emirates' Hope Mars mission, and by the time COMPASS would launch, NASA's Europa Clipper and Dragonfly missions. The next-generation version will employ major reuse of the software-defined radio (SDR) algorithms and processing while taking advantage of more advanced modern hardware. A block diagram details the subsystem in Exhibit 3-10.

Exhibit 3-11: COMPASS mass and power resource table

	Mass		Average Power	
	CBE (kg)	MEV (kg)	CBE (W)	MEV (W)
Structures & Mechanisms	352.66	402.93	-	-
Thermal Control	31.20	34.37	85.00	97.75
Propulsion (Dry Mass)	276.54	290.37	-	-
Attitude Control	45.38	48.49	41.60	43.68
Command & Data Handling	35.12	38.15	55.15	63.11
Telecommunications	66.00	74.67	124.50	137.43
Power	293.26	336.09	41.40	46.31
Harness	102.92	108.06	12.56	14.12
Science Payload	87.8	123.1	71	82.5
Total Flight Element Dry Bus Mass	1290.88	1456.23	431.21	484.90
Propellant Mass	-	1630	Contingency: 13% Margin: 142% Tot. Margin: 173%	
LV Capability	-	5160		

3.11 Mass & Power Resource Table

Exhibit 3-11 depicts the mass and power resource table for COMPASS.

3.12 Mission Design

The COMPASS trajectory design is composed of three mission phases: launch and interplanetary cruise; capture into the Jovian system; multiphase science tour (see Exhibit 3-12).

Exhibit 3-12: Mission phases, with assumptions and the major events.

Mission Phase	Description
I. Launch & Interplanetary Cruise	• Launch, Falcon Heavy Expendable • Deep Space Maneuver (DSM) • Earth Gravity Assist (EGA) • Jupiter system arrival
II. Capture into the Jovian System	• Io-flyby (I1) • Jupiter Orbit Insertion (JOI) • Perijove-Raise Maneuver (PRM) • Io-flyby (I2)
III. Science Tour	• Science Phase I (high-inclination, larger PJ) • Science Phase II (low-inclination, lower PJ) • Disposal via Jupiter impact

The goal of mission phases I and II is to deliver COMPASS to an orbit that meets the requirements for Science Phase I, while setting up conditions for efficient transition into Science Phase II. The science campaigns/phases can be further broken into their respective requirements flowed down from the science and measurement objectives. Here, r_p and r_a represent perijove and apojove radii, respectively, i represents inclination relative to the Jovian equator, and local solar time is denoted as LST. The radius of Jupiter is defined as RJ = 71492 km. Previous concepts to study the Jovian magnetosphere and radiation environment are structured such that the initial science orbit lies in the Jovian moon plane, and inclination is increased via flybys of Callisto (Campagnola & Kawakatsu 2012). In the COMPASS study, this paradigm is reversed so that the tour is initially inclined, with Io flybys executed on each revolution of the spacecraft about Jupiter to reduce orbital period and apojove radius. Then, while still in this inclined orbit, a transfer to Callisto is performed, and a series of Callisto flybys enable simultaneous reduction of both inclination and perijove radius, thus covering lower inclinations in the last phase of the mission. To reduce radiation Total Ionizing Dose (TID) and risk of Europa impact, non-zero inclination is maintained during the entire Science Phase. The Science Phase details are:

Science Phase I (SP1)
- Orbital inclination relative to Jovian equator i ≥ 30°
- Perijove within 4 RJ ≤ r_p ≤ 6 RJ, and within dusk quadrant 15:00 ≤ LST ≤ 21:00 hrs
- Apojove within 30 RJ ≤ r_a ≤ 90 R_J, and within dawn quadrant 3:00 ≤ LST ≤ 9:00 hrs
- ≥ 4 orbits

Science Phase II (SP2)
- Orbital inclination relative to Jovian equator i ≤ 20°
- Perijove within 1 RJ ≤ r_p ≤ 2 RJ, and within dusk quadrant 15:00 ≤ LST ≤ 21:00 hrs
- Provide coverage out to r = 30 R_J
- ≥ 3 orbits
- Ensure safe disposal, given possible spacecraft failure on any orbit in this phase

Launch and Interplanetary Cruise. Assuming the FHE, a 3:1 ΔV-EGA cruise trajectory is enabled. Here, a higher launch C3 is achievable, injecting the spacecraft into a roughly 3:1 resonance with Earth. A DSM at aphelion targets an increased V_∞ at the EGA, enabling transfer to Jupiter. During the EGA, COMPASS's payload will be turned on to operate the instruments for science and cross calibration opportunities in Earth's relatively observatory dense magnetosphere. Launch in 2030 is assumed for this point design, however the flight system design is scaled to meet the maximum propellant needs expected for any launch from 2030 – 2042. Launch declination is constrained ≤ 28.5° for all solutions. For each day in the launch period, Jupiter arrival is constrained to a single epoch to enable the design of a single capture sequence and science tour. The date of arrival to the Jovian system is initially selected to minimize the DSM+JOI ΔV, and is then adjusted forward ~16 days to optimize moon transfer phasing during the science tour. A summary of the 2030 launch appears in Exhibit 3-13. Details on the launch and interplanetary trade space are provided in the mission design Appendix.

Capture into the Jovian System. Upon arrival to the Jovian system, a capture sequence inserts the spacecraft into Jovian orbit. The capture sequence that best aligns with the goals of the science campaign is an Io-aided (I1) JOI maneuver, followed by a PRM at apojove to counteract solar gravity perturbations and retarget a second Io flyby (I2). (A summary of the capture trade study is provided in mission design Appendix.) All Io flybys are modeled at 300 km altitude, and JOI and PRM are 871.7 m/s and 22.3 m/s, respectively. Because the I1 flyby occurs after perijove, it is navigationally risky to execute JOI at perijove (prior to I1). For this reason, JOI is delayed to 1-hour after exit from the I1 sphere-of-influence. To place perijove over Jupiter's northern hemisphere, the Io flybys are targeted at the orbit descending node. This improves detection of particle losses in regions where Jupiter's magnetic field changes more steeply as a function of latitude and longitude, and enables the X-ray imager to observe Jupiter's northern main aurora and atmosphere.

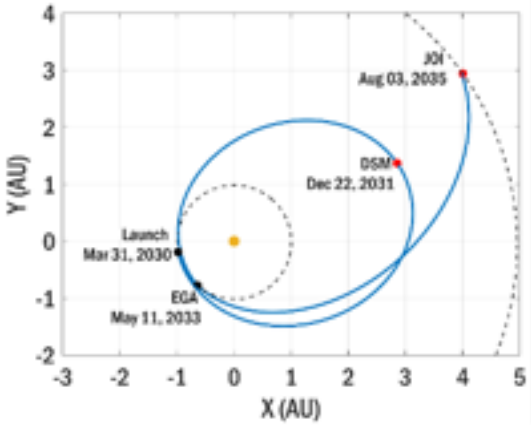

2030 3:1 ΔV-EGA	
Dates	Mar 31 – Apr 20, 2030
Max C3 (km2/s2)	52.0
Max DSM (m/s)	226.2
Min EGA Alt (km)	1570
Years to Jupiter	5.1
Arrival V_∞ (km/s)	6.3 km/s
Arrival Date	Aug 03 2035

Exhibit 3-13: Interplanetary Cruise to Jupiter on a 3:1 ΔV-EGA

Science Tour. The COMPASS science tour is composed of two mission design phases that are tailored to meet the requirements for Science Phases I & II:

Io Pump-Down
- From an inclined orbit (i ≥ 30°), use repeated flybys of Io to reduce orbit period and apojove
- Approach 1:1 resonance with Callisto, and intersection of ascending node with Callisto's orbit
- Transfer to Callisto to begin transition to Science Phase II

Callisto Crank-Down
- Use repeated flybys of Callisto to simultaneously reduce inclination and perijove radius
- Begin Science Phase II, i.e., where $r_p \leq 2$ RJ and i ≤ 20°

To transfer between Io and Callisto from an inclined orbit, both orbit node crossings must intersect each of the moon orbits, leading to a fairly constrained geometry. The benefit of targeting such a condition is that the entire science tour can remain inclined, reducing TID and risk of Europa impact. By design, COMPASS's orbital tour ensures no inspections with Europa's orbit, minimizing any chance of collision with Europa prior to entry into Jovian atmosphere at mission end-of-life. Exhibit 3-14 shows the targeted orbital element space for Science Phase II, i.e., the Callisto flyby conditions that enable $r_p \leq 1.5$ R_J with $i \leq 20$. In Exhibit 3-14 (left panel), curves of constant V_∞ are plotted in r_p - i orbital element space, assuming 1:1 resonance with Callisto and with regions that violate the Science Phase II conditions grayed out. The result is a targeted range of Callisto V_∞ magnitudes from ~9.5 - 10 km/s. With the inclusion of Jupiter gravity harmonics, specifically J2, the ΔV to continue targeting subsequent Callisto flybys increases significantly,

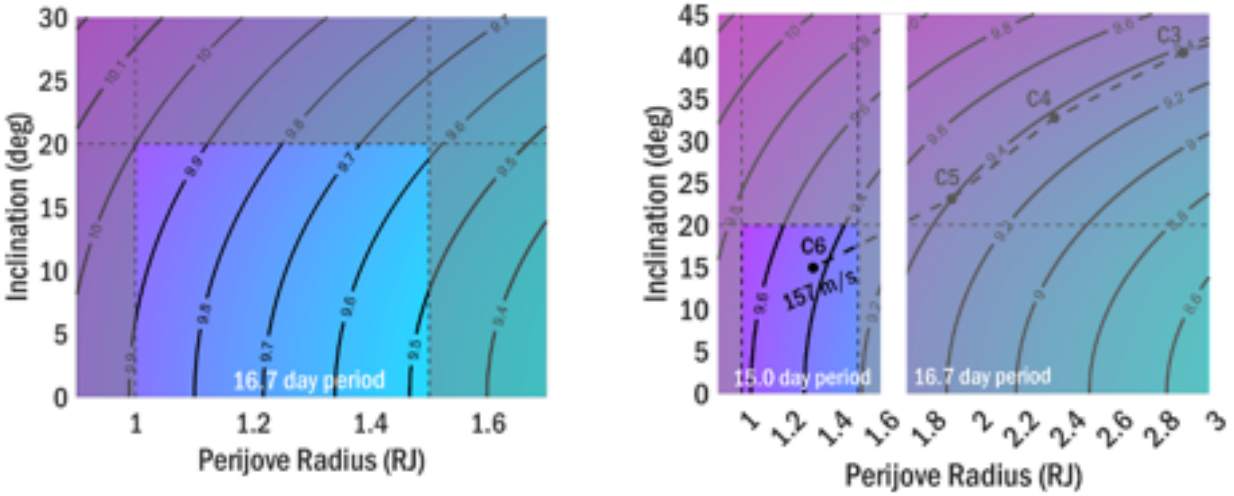

Exhibit 3-14: Callisto flybys are used to simultaneously reduce perijove radius and inclination. Colormaps with curves of constant V_∞ (km/s) overlaid in black).

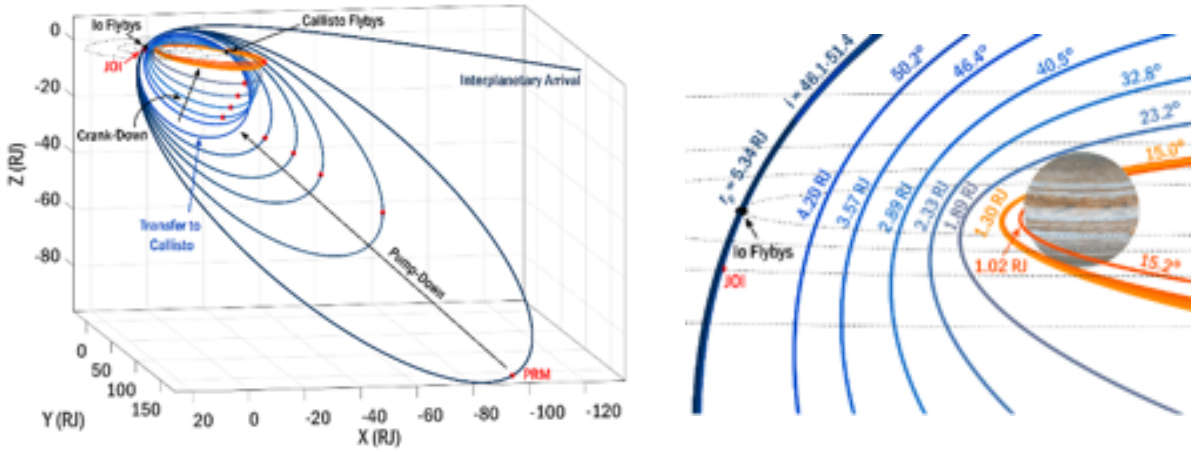

Exhibit 3-15: COMPASS science tour, flybys, and maneuvers appear as black and red points, respectively. Blue curves represent Science Phase I, orange curves represent Science Phase II.

especially as r_p and i decrease. By allowing the orbital period to reduce from the 1:1 resonance after a final Callisto flyby (C6 for the tour presented here), a lower perijove can be achieved for reduced Callisto V_∞ and fewer Callisto flybys. The path of the final COMPASS science tour appears in Exhibit 3-14 (right panel), with joined maps of r_p - i space for the 1:1 resonance, and the post-C6 orbital period of 15 days. The outgoing C6 inclination is constrained $\geq 15°$ to reduce TID, and the final tour is optimized from launch through end of Science Phase II in a high-fidelity model, including solar gravity, Jupiter J2, and Io, Europa, Ganymede and Callisto point-mass gravity while inside Jupiter's sphere-of-influence.

The final tour associated with the path in Exhibit 3-14 is plotted in the Ecliptic-J2000 frame in Exhibit 3-15. Exhibit 3-15 (left panel) shows the full tour from interplanetary arrival through disposal, and Exhibit 3-15 (right panel) focuses on the changes in perijove radius and inclination during the Callisto crank-down phase. A summary figure showing the evolution of perijove, inclination, and TID appears in Exhibit 3-16. Note that from flybys C5 to C6, both perijove and inclination are in between the required values for Science Phases I & II. This period is defined as a "Transition" between the two science campaigns, but valid science is still contributed during this time. A tabulated summary of the tour is additionally provided in the Appendix.

Disposal. After completion of the first 3 orbits of the Science Phase II campaign, a 150 m/s disposal maneuver is performed at apojove to reduce perijove to 1.022 RJ, enabling Jupiter J3 gravity perturbations to further reduce perijove until "impact" with Jupiter occurs 66 days later. Here, impact is defined as spacecraft vaporization due to Jovian atmospheric entry. While perturbations from J2 will drag the orientation of the orbit, it would not cross Europa's orbit until 74 days *after impact*. This disposal strategy enables an extended mission without requiring s/c survival to ensure impact. The time to impact can be adjusted by changing the magnitude and/or date of the disposal maneuver. The maneuver could also be delayed or executed earlier, depending on radiation degradation assessments during the tour.

ΔV Budget. The ΔV budget for the COMPASS trajectory is provided in Exhibit 3-17, and covers any launch year given the assumptions listed. Both deterministic and statistical ΔV are included in the allocated budget, and an additional 2% margin for unallocated ΔV is assumed.

3.13 Concept of Operations

The trajectory elements and critical events are similar to previous missions operated at APL, and the mission operations can be supported using existing APL Mission Operations Center (MOC) infrastructure and NASA Deep Space Network (DSN) capabilities. Post-launch commissioning is

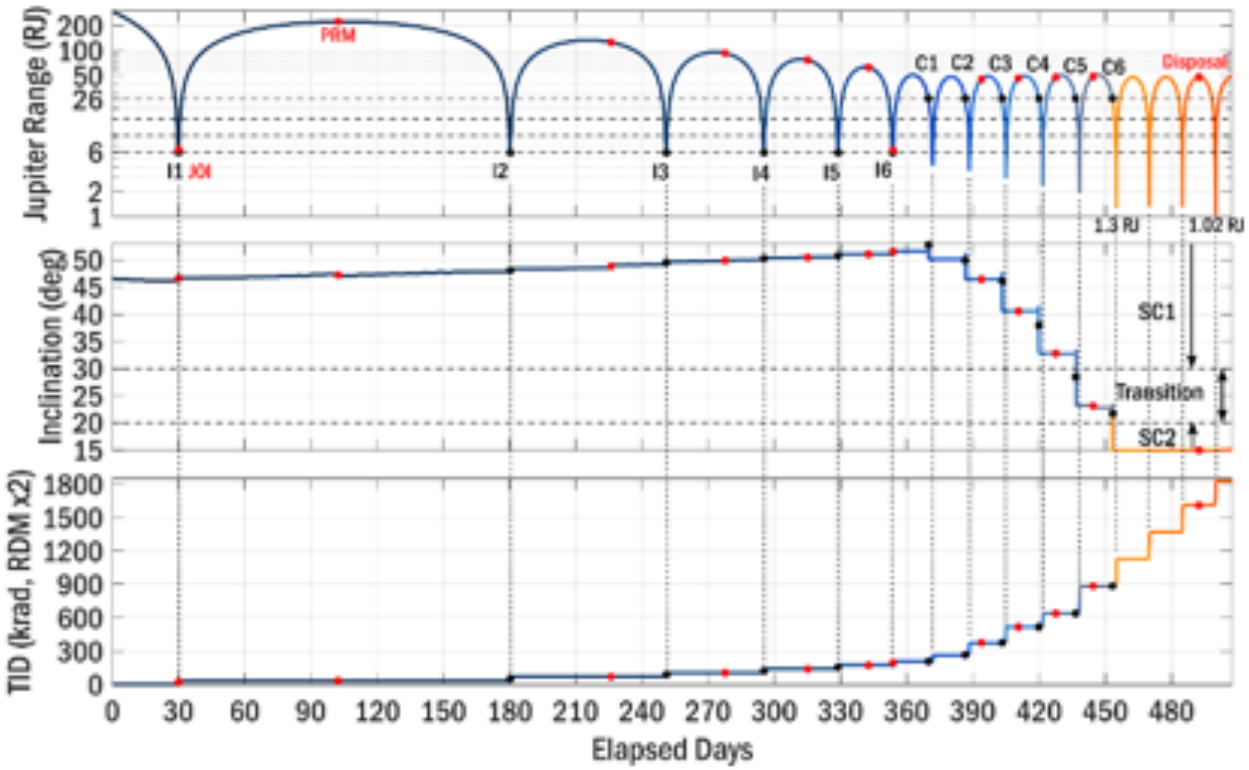

Exhibit 3-16: Time history (beginning 30 days prior to I1) of Jupiter range, inclination relative to the Jovian equator, and total ionizing dose over the science tour; perijove passes connected by vertical lines.

expected to take approximately five weeks, during which there is near-continuous DSN coverage in the first week, gradually reducing to a single 8-hour X-band communications pass per day by the end of the period. The cruise phase is 5.5 years, including a deep space maneuver (DSM) and an Earth gravity assist (EGA). The spacecraft will operate in spin-stabilized mode, with annual checkout activities. Instruments will be on during early cruise instrument checkouts, around the EGA, and for annual checkouts during cruise. Operating the instruments in continuous burst mode (in-situ payloads) and special burst campaigns (remote sensing payloads) during the EGA will be particularly advantageous for checkout, in-flight calibrations, and comparisons to other observatories in the well-observed Terrestrial magnetosphere system; EGA observations may even provide publishable scientific results in collaboration with additional NASA and other observatories at Earth. During most of cruise, DSN 34-m antennas will be utilized for three 8-hour X-band communications passes per week to conduct typical operations including uplink of command loads every 3-4 weeks, regular downlink of spacecraft engineering data, and real-time evaluation of spacecraft health and safety. DSN coverage is increased before and after the DSM and EGA to

Exhibit 3-17: COMPASS ΔV budget

Maneuver Name	ΔV (m/s)		Assumptions
	Deterministic	Statistical	
Launch cleanup	-	20	C3 ≤ 52 km²/s²
DSM (3:1 ΔV-EGA)	230	5	3:1 ΔV-EGA
EGA	-	10	Flyby targeting + cleanup
JOI	875	25	Io-aided JOI
Tour	157	125	Flyby targeting and cleanup
		5	3% of tour deterministic
Disposal	150	-	Targeting perijove at 1.02 R_J
Subtotal	1412	190	Total allocated ΔV
Unallocated Margin	28		2% of deterministic total
Total	**128**		

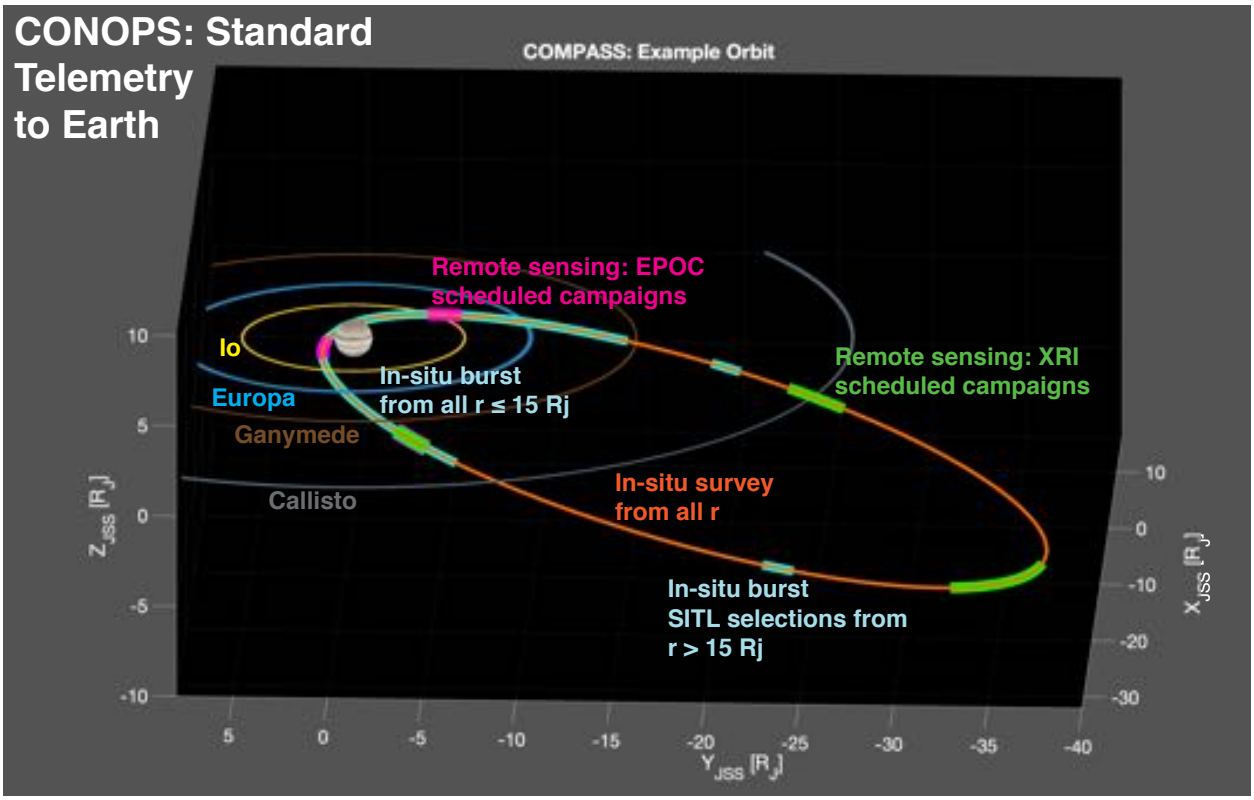

Exhibit 3-18: COMPASS concept of operations plan for a Science Phase II. A Data Acquisition plan is in the Appendix.

support ranging and navigation, as well as instrument data downlink after EGA.

Jupiter approach begins approximately five months before Jupiter orbit insertion (JOI). During Jupiter approach, instruments will be on in survey mode for science characterization of the solar wind. DSN coverage increases in this period compared to cruise, to support ranging and navigation approaching JOI. Given the X-band downlink data rates available using the high-gain antenna at this time, and a cadence of three 8-hour DSN communications passes per week, science data collected can be downlinked within the same week, so there are no concerns about onboard data buildup prior to JOI and Science Phase operations. Continuous critical event DSN coverage will be required for ten hours around the JOI burn. Instruments will be turned off during the JOI burn, but turned on again soon after, providing the "first-light" observations from COMPASS within the inner Jovian magnetosphere. A few months after JOI, there is a large periapsis raise maneuver (PRM), with increased DSN coverage before and after to support ranging and navigation.

Science Phase I begins soon after the PRM and includes thirteen orbits of Jupiter over the 1.5-year baseline. The Science Phase is roughly divided into Phase 1 (30º or higher inclination) and Phase II (low inclination, r_p between 1 and 2 R_J) orbits. During both phases, the communications cadence is approximately five 8-hour X-band pass per week (seven days) with a single 34-m DSN antenna. Command loads are uplinked once every two weeks. In order to maximize the value of the science return despite limitations on downlink capability from Jupiter, the science data collection approach is to maximize onboard collection, and then downlink only selected portions of the high-rate ("burst mode") data. During every orbit of the Prime Science Phases (see Exhibit 3-18), COMPASS acquires and records (onboard) data from all of the in-situ payloads (particles: TPD, SPD, EPD, RPD, and UPD; fields: FGM; and duty-cycled waves data: FGM, SCM, and EFS) in *both* survey and burst modes. The in-situ payloads data

acquisition modes, rates, and products are summarized in the Appendix. Remote sensing (XRI and EPOC) payloads are operated during pre-scheduled image-capture campaigns for moons and Jupiter (XRI and EPOC) and radiation belts (XRI) based on relative orbit, target, and FoV orientations. The remote sensing payloads data acquisition modes and rates are summarized in the Appendix. The standard products that will be downlinked to ground from every orbit during the Prime Science Phases include: all in-situ burst data from $r \leq 15$ R_J; all survey data from the entire orbit; all remote sensing data from the scheduled acquisition campaigns. Using the survey data from all locations at $r > 15$ R_J, ground-in-the-loop decisions made by the science team upon review of the downlinked survey data (i.e., "scientist-in-the-loop" or "tohban" review and prioritization) will inform data management decisions for the collected high-rate (burst) science data; the telemetry budget accounts for additional burst-rate telemetry to be downlinked to Earth from selected periods of high-interest from $r > 15$ R_J. The onboard data storage capacity allows for storage of approximately 1.5 months' worth of data to account for this approach, as well as any anomalies, thus ensuring that these data management decisions will not be particularly time-critical for the mission and science operations teams.

During Phase I and Phase II orbits, most of the in-situ instruments collect data continuously at both survey and burst rates throughout the orbit. The burst-rate particle data ensures adequate sampling throughout every COMPASS orbit of the particle distributions required to close on COMPASS science (see the STM). For example, during the fastest portions of COMPASS' orbital tour, the observatory crosses L-shells at a maximum rate during perijove passes of $\Delta L/\Delta t = 0.02$ L-shells/minute, and in burst-mode (standard inside of $r \leq 15$ R_J and thus available during *all* perijove passes), particle distributions (including phase space densities) will be available every 15-seconds (i.e., every 1/2 -spin or $\Delta L \geq 0.005$). This is also true for the wave spectral data, which will be collected at 6-samples per second in burst mode. As alluded to above, due to the large data volume they generate, the in-situ SCM and EFW instruments cannot capture data at burst rates throughout the orbit and must be duty cycled. The remote sensing instruments acquire data at lower survey rates throughout the orbit, with selected imaging periods during pre-scheduled image-capture campaigns. These include XRI imaging campaigns targeting Jupiter, moons, and the radiation belts, and EPOC imaging campaigns for the moons and Jupiter. Reiterating: All of the survey rate data from the instruments and the imaging campaign data are downlinked, along with a subset of collected burst data – data from within 15 R_J and selected burst data from the rest of the orbit, based on ground-in-the-loop selection by the science team. With this strategy, the mission science data return from the Prime Science Phase is 230 Gb, including 174 Gb from Science Phase I, and 56 Gb from Science Phase II orbits, with 25% or greater margin compared to available downlink capability in each orbit.

The total mission science data return is 300 Gb. In total, 15,620 hours of DSN time over 1816 passes is needed to support the entire mission. This data acquisition and downlinked telemetry strategy is fully intended to keep COMPASS science operations simple and manageable while simultaneously optimizing data return and availability for state-of-the-art and unprecedented studies of Jupiter's magnetosphere and radiation environment. Such a "scientist-in-the-loop" approach is novel for Jovian science missions, and it should enable unexpected, discovery-level science above and beyond of the primary science goals. Furthermore, this standard data acquisition and downlink approach and dedicated system resources to ensure the sheer magnitude of burst-rate data from all COMPASS payloads offers unprecedented levels of high-quality data from the Jovian system and ensures discovery-level science during both Prime Science Phases and closure on COMPASS science goals and objectives.

3.14 Ground System

The Compass Ground Data System (GDS) is based on proven ground data systems from previous APL decoupled instrument commanding missions including Parker Solar Probe and Van Allen Probes. The GDS will utilize the existing APL Mission Operations Center (MOC) infrastructure and APL's Mission Independent Ground Software (MIGS). No new GDS functionality has been identified for the Compass mission at this time. The Compass GDS supports all phases of the mission including: subsystem test, observatory I&T, hardware simulator control, and flight operations. A block diagram of the GDS architecture is included in the Appendix. Key GDS functionality includes:

- Delivery of commands to the spacecraft and GSE
- Acquisition, routing, processing, monitoring, and archive of real-time telemetry
- Supports CFDP (uplink/downlink)
- Tools for on-board memory management
- Tools for radiation monitoring
- Timekeeping functions
- Navigations tools

3.15 Risk List

Risks identified during the COMPASS study are listed below with proposed mitigations. Exhibit 3-19 summarizes the risks in a likelihood vs. consequences matrix.

- **Risk 1:** If the radiation environment prevents the instruments from achieving adequate SNR, then science requirements may not be met. **Mitigation:** Ensure development plans adequately address environment; increase shielding mass; subtract signal detection; review/update Jovian radiation model using more updated information.
- **Risk 2:** If the radiation environment impacts the solar cell performance to a greater degree than expected, then the solar panels may not provide adequate power output at EOL. **Mitigation:** Further LILT/high-radiation characterization testing; review/update Jovian radiation model using more updated information.

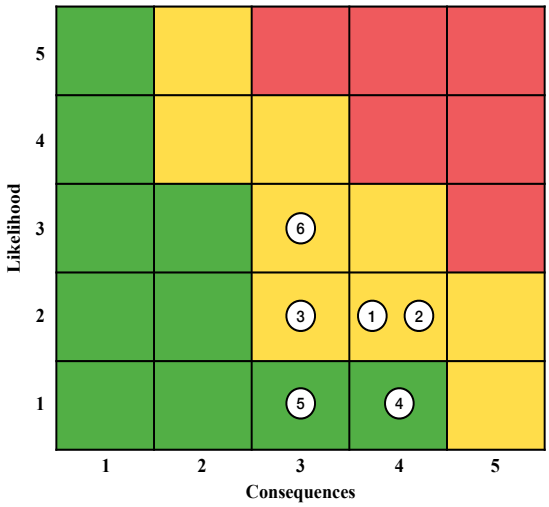

Exhibit 3-19: Risk summary for COMPASS

- **Risk 3:** If blockage of trackers by Jupiter or blinding of the trackers by the radiation environment occurs, then an accurate reconstruction of the attitude may not be possible. **Mitigation:** SSIRU and gyro rate propagations; review/update Jovian radiation model using more updated information.
- **Risk 4:** If the spacecraft is impacted by dust or particles in the Jovian ring system, then it may suffer a critical failure**. Mitigation:** Mission design works to avoid rings; review/update Jovian ring modeling (and understand severity); redundant systems; dust impact mitigation implementation on SC.
- **Risk 5:** If the SPE angle around EGA is unacceptably large, then communications may be degraded in order to remain power positive. **Mitigation**: Continued study/phase A; additional antennas/capability.
- **Risk 6:** If the designed ROSAs required for this design are too large to manufacture or to be accommodated by the spacecraft structure, then the spacecraft may need to be redesigned. **Mitigation:** Advanced early discussions/analysis with ROSA vendors; analysis of alternatives; refine/"sharpen the pencil" on design; reduce power on design.

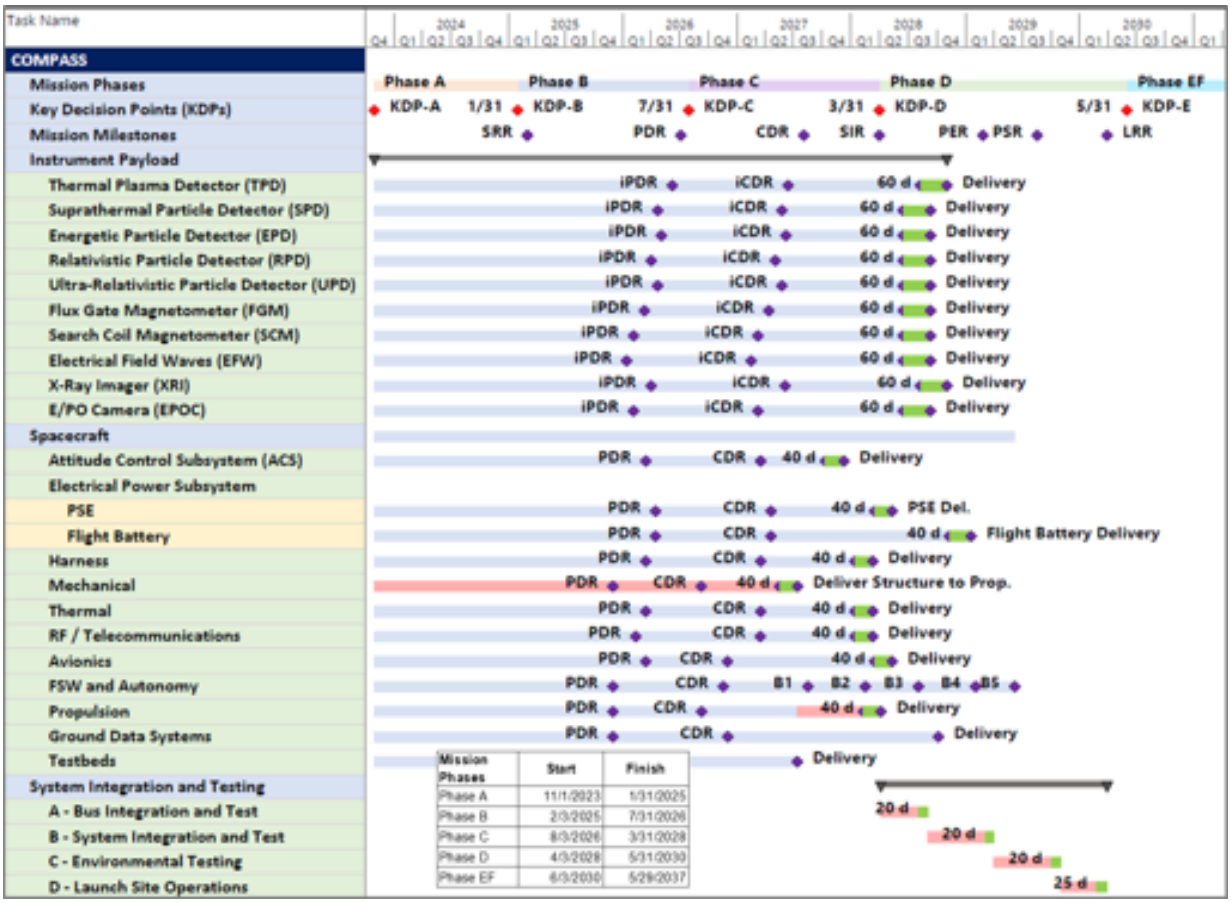

Exhibit 4-1: COMPASS high-level mission schedule.

4. Development: Schedule & Constraints

The High-Level Mission Schedule for COMPASS (Exhibit 4-1) is based upon IMAP, a mission of analogous scope and complexity. **However, it must be emphasized that this only represents a notional representative timeline that assumes an imminent Phase A start in 2023 and targets a launch in 2030. The mission design is extremely flexible and can accommodate multiple alternative launch windows (see Appendix B).**

Science, Technology Development Plan(s). All spacecraft components are at TRL 6 or higher, and all instruments within the payload are based upon previously flown instruments. The Appendix contains technology maturity plans to enhance science return (e.g., higher SNR) of COMPASS; however, they are not needed for the success of the mission.

Development Schedule and Constraints. The development phase critical path includes the spacecraft structure design and fabrication, followed by integration of the propulsion system, and remaining spacecraft integration and testing activities. The schedule contains a total of 8 months of funded schedule reserves (Exhibit 4-2). The Primary Launch Period is March 11, 2030 through April 20, 2030. Additional launch periods are discussed in Section 3 of this report.

5. Mission Life-Cycle Cost

The COMPASS mission is of Concept Maturity Level 4. The payload and spacecraft estimates capture the resources required for a preferred point design and take into account subsystem level mass, power, and risk. Our estimate also takes into account the technical and performance characteristics of components. Estimates for Science, Mission Operations, and Ground Data System elements whose costs are primarily determined by labor take into account the Phase A–D schedule and Phase E timeline.

Exhibit 4-2: Key mission phases with associated durations

Project Phase	Duration (Months)	Project Phase	Duration (Months)
Phase A – Conceptual Design	15 mos.	Start of Phase B to Delivery of E/PO Camera (EPOC)	43 mos.
Phase B – Preliminary Design	18 mos.	Start of Phase B to Delivery of Search Coil Magnetometer (SCM)	43 mos.
Phase C – Detailed Design	20 mos.	Start of Phase B to Delivery of Electrical Field Waves (EFW)	43 mos.
Phase D – Integration & Test	26 mos.	Start of Phase B to Delivery of Attitude Control System (ACS)	34 mos.
Phase E/F – Primary Mission Operations / Extended Mission Operations	84 mos.	Start of Phase B to Delivery of Power System Electronics (PSE)	39 mos.
Start of Phase B to PDR	17 mos.	Start of Phase B to Delivery of Flight Battery	47 mos.
Start of Phase B to CDR	30 mos.	Start of Phase B to Delivery of Harness	37 mos.
Start of Phase B to Delivery of Thermal Plasma Detector (TPD)	45 mos.	Start of Phase B to Delivery of Propulsion Structure	29 mos.
Start of Phase B to Delivery of Flux Gate Magnetometer (FGM)	43 mos.	Start of Phase B to Delivery of Thermal	37 mos.
Start of Phase B to Delivery of Energetic Particle Detector (EPD)	43 mos.	Start of Phase B to Delivery of RF Subsystem	37 mos.
Start of Phase B to Delivery of Relativistic Particle Detector (RPD)	43 mos.	Start of Phase B to Delivery of Avionics	39 mos.
Start of Phase B to Delivery of Ultra-Relativistic Particle Detector (UPD)	43 mos.	Start of Phase B to Delivery of Propulsion System	38 mos.
Start of Phase B to Delivery of Suprathermal Particle Detector (SPD)	43 mos.	System Level Integration & Test	26 mos.
Start of Phase B to Delivery of X-Ray Imager (XRI)	45 mos.	Project Total Funded Schedule Reserve	8 mos.
Total Development Time Phases B - D		65 mos.	

The result is a mission estimate that is comprehensive and representative of expenditures that might be expected if the COMPASS mission is executed as described. The COMPASS Phase A–F mission cost, including unencumbered reserves of 50% (A–D) and 25% (E–F), is $1.2B in fiscal year 2022 dollars (FY$22), as shown in Exhibit 5-1. Excluding all LV-related costs, the COMPASS Phase A–D mission cost is $882M FY22.

Exhibit 5-2 shows an estimated spend profile by phase and fiscal year for Phases A-D, excluding the LV costs.

5.1 Mission Ground Rules and Assumptions

Here is a list of ground rules and assumptions used for estimating the mission life-cycle cost of COMPASS:

- Estimating ground rules and assumptions are derived from the "Ground Rules for Mission Concept Studies in Support of Heliophysics Decadal Survey" dated January 2022
- Mission costs are reported using the level-2 (and level-3 where appropriate) work breakdown structure (WBS) provided in NPR 7120.5E
- Cost estimates are reported in fiscal year 2022 (FY22) dollars
- The NASA New Start inflation index provided by the Planetary Mission Concept Studies Headquarters (PMCS HQ) was used to adjust historical cost, price data, and parametric results to FY22 dollars if necessary
- The mission does not require Technology Development dollars to advance components to TRL 6 because all COMPASS mission components are TRL 6 or greater

Exhibit 5-1: Estimated Phases A-F COMPASS mission cost by WBS elements

COMPASS Mission ROM Estimate (FY22$M)					
WBS	**Description**	**Ph A-D**	**Ph E-F**	**Total**	**Notes**
	Phase A	$6.0	-	$6.0	Assumption based on previous studies
1/2/3	PM/SE/MA	$78.1	-	$78.1	A-D: Wrap factor based on recent NFs and APL missions E-F: Bookkept with WBS7
4	Science	$21.8	$26.4	$48.2	Cost per month of recent NFs and APL missions
5	Payload	$134.5	-	$134.5	Parametric and analogy based estimates
6	Spacecraft	$262.9	-	$262.9	Estimated via parametric models
7	Mission Ops	$24.1	$33.2	$57.3	Cost per month of recent NFs and APL missions
8	LV	$210	-	$210	Falcon Heavy Expendable Placeholder
9	Ground Data Systems	$11.3	$1.8	$13.1	COMPASS specific estimate from GDS lead
10	I&T	$61.7	-	$61.7	APL historic I&T % of HW (incl. testbeds)
	Subtotal	$810.5	$61.3	$871.8	
	Reserves	$297.3	$15.3	$312.6	50% B-D, 25% E-F, excludes LV
	Total w/ reserves	$1107.8	$76.6	$1184.4	
	Total w/o LV	$897.8	$76.6	$974.4	

- A launch vehicle cost estimate of $210M is held in WBS 8 and assumes a SpaceX Falcon Heavy Expendable launch vehicle
- Phase A–D cost reserves are calculated as 50% of the estimated costs of all components excluding the launch vehicle. Phase E–F cost reserves are calculated as 25% of the estimated costs of all Phase E elements

5.2 Cost Benchmarking

The cost and scope of the COMPASS concept corresponds well with the NASA missions shown Exhibit 5-3. The estimated cost to develop COMPASS compares favorably to these NASA missions with an average cost of $970M. Excluding LV, the Phase A-D COMPASS estimate of $882M FY22$ would put it in the New Frontiers mission class cost range.

5.3 Methodology & Basis of Estimate

The COMPASS CML 4 mission cost estimate is a combination of high-level parametric and analog techniques and incorporates a wide range of uncertainty in the estimating process. No adjustments were made to remove the historical cost of manifested risk from the heritage data underlying the baseline estimate. Therefore, before reserves are applied, the estimated costs already include a historical average of the cost of risk. This approach is appropriate for capturing risk and uncertainty commensurate with early formulation stages of a mission. The following describes the basis of estimate for each element.

WBS 1, 2, 3 Project Management, Systems Engineering, Mission Assurance (PM/SE/MA). Because these functions depend on multiple mission- and organization-specific characteristics (Hahn, 2014), cost analogies to comparable historical missions are preferred over cost model output, which does not take the mission into account. Existing analyses demonstrate that hardware costs are a reliable predictor of these critical mission function costs. APL has conducted thorough and rigorous analyses of PM/SE/MA costs, both for historical APL missions and for analogous missions. The PM/SE/MA estimate for COMPASS relies on APL's analysis of historical PM, SE, and MA practices on Van

Exhibit 5-2: Estimated Phases A-D spend profile (excludes LV)

Phase	FY22$M
Phase A (FY24)	$4.4
Phase A (FY25)	$1.6
Phase B (FY25)	$120.4
Phase B (FY26)	$120.4
Phase C/D (FY26)	$2.0
Phase C/D (FY27)	$280.4
Phase C/D (FY28)	$197.8
Phase C/D (FY29)	$115.2
Phase C/D (FY30)	$39.8
Total	**$881.9**

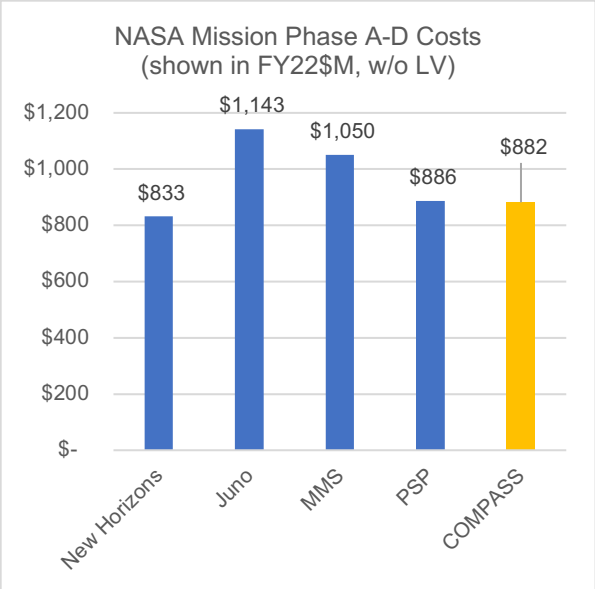

Exhibit 5-3: Phase A-D cost with comparable NASA missions

Allen Probes, Parker Solar Probe (PSP), and New Horizons (NH). Van Allen Probes and PSP in particular include costs associated with current NASA requirements (e.g., Earned Value Management System (EVMS), NASA 7120.5F). COMPASS's total mission PM/SE/MA cost is 15.9% of the flight system (payload + spacecraft + I&T). This percentage is allowed to vary along with hardware costs as part of the mission cost risk analysis, discussed below, to capture uncertainty (particularly given CML-4-level design phase).

WBS 4 Science. This element covers the managing, directing, and controlling of the science investigation. It includes the costs of the Principal Investigator (PI), Project Scientist (PS), science team members, and activities. The Phase A–D and E–F science estimate is an analogous estimate based on the cost per month of NH, MESSENGER, Cassini, Dragonfly, OSIRIS-Rex, and Juno. NH is APL's most recently-flown New Frontiers mission and MESSENGER is a recent historical data point for planetary orbital science. The analogy costs are representative of expenditures for science on a typical New Frontiers mission. The estimate reflects the manpower needed to create various data products as well as to ensure closure to science objectives.

Exhibit 5-4: COMPASS WBS 5 costs in FY$22M

COMPASS Mission Estimate (FY22$M)			
WBS	**Description**	**Total**	**Notes**
5	Payload	$130.2	Parametric and analogy-based estimates
5.1	PL PM/SE/MA	$9.9	Based on NH, PSP, Van Allen Probes, MESSENGER
5.2	Thermal Plasma Detector (TPD)	$12.6	Average of NICM 9/SEER Space Estimates
5.3	Suprathermal Particle Detector (SPD)	$15.5	
5.4	Energetic Particle Detector (EPD)	$12.0	
5.5	Relativistic Particle Detector (RPD)	$13.4	
5.6	Ultra-relativistic particle detector (UPD)	$17.5	
5.7	X-Ray Imager (XRI)	$21.2	
5.8	Flux Gate Magnetometer (FGM) incl. boom	$8.0	
5.9	Search Coil Magnetometer (SCM)	$2.8	
5.A	Electric Field Waves (EFW)	$11.2	
5.B	Education/Public Outreach Camera (EPOC)	$6.1	

WBS 5 Payload. The WBS 5 estimate includes a science payload of 10 instruments and payload-level PM/SE/MA (Exhibit 5-4). The 8.2% cost-to-cost factor for estimating payload PM/SE/MA costs is based on the Van Allen Probes, NH, MESSENGER, and PSP payload suite cost data with PM/SE/MA costs estimated as a percentage of the payload hardware. Technical management and systems engineering costs for individual instruments are carried in their respective instrument development costs. Given the early design phase, multiple approaches are used to estimate each instrument

to capture the potential range in cost. This includes two parametric estimates that rely on different sets of input variables (SEER Space and NICM 9). An average of the two parametric estimates is used as the point estimate to prevent estimate bias (high or low). These estimates are subject to a cost risk analysis (discussed below) to further quantify uncertainty. No technology development is required for the payload.

WBS 6 Spacecraft. The WBS 6 estimate includes the spacecraft (SC) bus, flight software, component engineering, and radiation shielding (Exhibit 5-5). SC PM/SE/MA is carried in WBS 1, 2, and 3 consistent with APL in-house builds [Hahn 2015]. The basis of estimate relies primarily on parametric models. The exception to this is the propulsion system, estimated via a ROM by a propulsion subject-matter expert. An average of two parametric estimates is used as the point estimate to mitigate estimate bias (high or low). SEER Space is one of the primary estimating methodologies because it was designed specifically for missions in early formulation stages. TruePlanning is also utilized as it provides a cost estimate at the component level. No technology development is required for the SC. The two parametric estimates are within 15% of each other (which is a reasonable range given different input variables). Cross-checks are shown in the table.

Exhibit 5-5: COMPASS WBS 6 costs in FY$22M

COMPASS Mission Estimate (FY22$M)			
WBS	**Description**	**Total**	**Notes**
6	Spacecraft	$263.3	Estimated via parametric models
6.1	Mechanical	$32.6	All subsystem estimates use the average of SEER Space and PRICE TruePlanning model outputs with the exception of three. The propulsion estimate is a ROM from the subsystem lead. FSW and Component Engineering estimates are based on average of larger APL historical missions.
6.2	Propulsion	$17.3	
6.3	Avionics	$35.2	
6.4	Power	$78.0	
6.5	Guidance & Control	$20.9	
6.6	Thermal	$4.9	
6.7	Telecommunications	$34.5	
6.8	Harness	$5.3	
6.9	Flight Software	$17.0	
6.A	Component Engineering	$17.7	

Exhibit 5-6: Inputs to cost distributions in FY$22M

COMPASS (FY22$M)			
WBS	**Cost Element**	**Point Estimate**	**High**
1, 2, 3	Mission PM/SE/MA	$72	$99
4	Science	$23	$29
5	Payload	$130	$175
6	Spacecraft	$263	$376
7	Mission Ops	$24	$30
9	GDS	$11	$14
10	I&T	$60	$70

WBS 7 & 9 Mission Operations (MOps) and Ground Data Systems (GDS). The COMPASS mission operations estimate includes mission operations planning and development, network security, data processing, and mission management. The pre- and post-launch mission operations estimate are based on the cost per month of NH, Dragonfly, Juno and OSIRIS-Rex. These missions represent expenditure on pre- and post-launch MOps for projects of comparable scope and complexity. The GDS estimate is a BUE from a ground data systems subject matter expert. The COMPASS Ground Data system provides full life cycle support for Subsystem Test, Observatory I&T, Hardware Simulator Control, & Flight Operations. The cost estimate is based on extensive reuse of PSP, IMAP, and DART Ground Software via APL's Mission Independent Ground Software (MIGS) as well as use of the existing Mission Operations Center (MOC).

WBS 8 Launch Vehicle & Services. The mission requires a launch vehicle that does not correspond with any of the options currently described in the Decadal Survey Ground Rules. As such, the figures used in this estimate are based on an evaluation of current best estimates

Exhibit 5-7: Cost risk analysis

Description	Value (FY$22M)	Confidence Level
Point Estimate	$799.9	48.8%
Mean	$899.3	
Standard Deviation	$374.7	
Reserves	$292.0	
Total w/ reserves	**$1,091.9**	**76.8%**

of the cost of the capability that will be required. The price of a LV with Falcon Heavy Expendable-type capabilities, based on past pricing to NASA missions of EELVs, would be approximately $210M for a launch using a standard sized fairing.

WBS 10 System Integration & Testing (I&T). This element covers the efforts to assemble and test the spacecraft and instruments. The COMPASS I&T effort is estimated as 12.7% of the hardware. This percentage is based on a detailed analysis of cost actuals from previous APL missions, including MESSENGER, NH, STEREO, Van Allen Probes, and PSP. This percentage is allowed to vary along with hardware costs as part of the mission cost risk analysis to capture the risk historically manifested during I&T.

Deep Space Network (DSN) Charges. This element provides for access to the DSN infrastructure needed to transmit and receive mission and scientific data. Mission charges are estimated at $28.5M using the Jet Propulsion Laboratory (JPL) DSN Aperture Fee tool. The DSN cost estimate covers pre- and post-contact activity for each linkage. The DSN aperture fee estimate is excluded from the mission budget and the cost tables in this report. DSN set up costs are estimated based on prior missions and included in the WBS 7 estimate.

5.4 Confidence and Cost Reserves

The cost risk ranges by major WBS element as inputs for the COMPASS probabilistic cost risk analysis to quantify total cost risk are found in Exhibit 5-6 & 5-7 and are described below.

PM/SE/MA. Given the use of cost-to-cost factors to estimate these functions, both the CER and underlying cost drivers are allowed to range

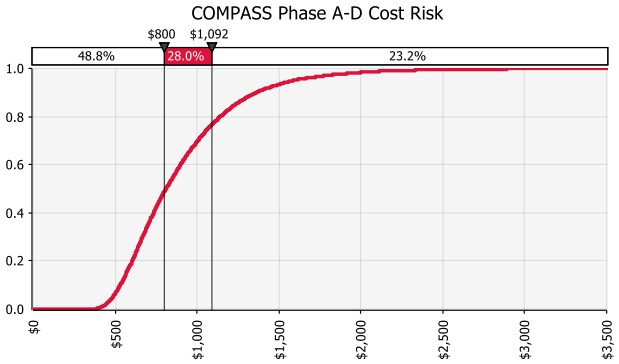

Exhibit 5-8: S-curve summary for COMPASS

so that all sources of uncertainty can be quantified.

Science/GDS/MOps. These are low-risk cost elements but are subject to cost growth as part of the cost risk analysis.

Payload. The average of the following three values: 70th percentile estimates of the two parametric model outputs and the analogy estimates with 35% growth, is used to inform the COMPASS payload risk model to capture the uncertainty given the CML-4-level design phase.

Spacecraft. Each subsystem is subject to a data-driven risk analysis based on historical APL cost growth. Mass input also varies in the SEER model consistent with early design programs to 30% over current best estimate.

I&T. I&T as a percentage of the payload and spacecraft from the point estimate is used to inform the risk analysis, allowing I&T to vary with hardware cost.

The estimate includes unencumbered cost reserves of 50% of the estimated costs of all Phase A–D elements except for the launch vehicle. A probabilistic cost risk analysis shows 76.8% confidence that the Phase A–D mission is achievable within the estimated costs of this study (Exhibit 5-8). The high confidence level is driven primarily by the large cost reserves for this pre-proposal concept. Given a typical competitive pre-Phase A NASA environment with 25% reserves on Phase A–D elements, the probabilistic cost risk analysis shows 64.7% confidence that the Phase A–D mission would be achievable. A 50th- to 70th-percentile confidence level is expected and reasonable for a pre-Phase A concept with this level of reserves.

A coefficient of variation (standard deviation/mean) of approximately 42% indicates appropriate levels of conservatism given the early formulation phase. The model confirms the point estimate and provides a reasonable basis for the COMPASS CML-4 study.

Appendix A. Additional Science Background and Technical Analyses

A.1 Science Background

Particle Origins

Background. Jupiter is known for its magnetosphere being filled with ions originating from its geologically active moons where oxygen and sulfur intensities rival that of protons (Mauk et. al 2004; Smyth and Marconi 2006; Smith et al. 2019). However, basic questions still remain unanswered, e.g., the moons Io and Europa exhibit geologic activity (e.g., Roth et al., 2014), but it is unclear which of them is the major oxygen source for the radiation belts. In addition to the moons, the Jovian ring system might indirectly provide heavy ions when already existing radiation causes spallation of atomic nuclei (Roussos et al., 2022). While moons, their associated gas tori, and rings provide particles to the radiation belts, these objects also simultaneously remove particles through absorption or cool them through Coulomb collisions (Clark et al., 2014, Nénon et al., 2018). The processes at play that ultimately balance the sources and losses and lead to the production and accumulation of Jupiter's extreme radiation belts is currently unknown. While a lot of attention in the planetary community was going into particle origins related to moons and rings, there are indications there are also processes at work that may be similar to those found at Earth, e.g., solar wind may gain access to the magnetosphere and supply the population of protons and electrons (e.g., Delamere et al., 2013). Furthermore, auroral regions of both Earth and Jupiter are known to be sources of energetic ions and electrons that at Jupiter can reach upwards of a few MeV (McKibben et al., 1993; Paranicas et al., 2018; Mauk et al., 2018; Clark et al., 2017, 2018). Interestingly, Jupiter's magnetosphere shows MeV electrons throughout the entire magnetosphere (e.g., Kollmann et al., 2018), suggesting that the original auroral field-aligned particles may be scattered and end up being trapped on Jovian magnetic field lines (e.g., Speiser, 1965; Young et al., 2008; Roussos et al., 2016). This may ultimately demonstrate a possible pathway for an atmospheric origin of radiation belt particles that at the Earth may be obscured by other processes. Conversely, the CRAND process is clearly observed at the Earth, which essentially uses the atmosphere to convert galactic cosmic rays into radiation belt protons. Currently it is unclear if CRAND is significant at Jupiter because its hydrogen atmosphere is inefficient in producing neutrons while on the other hand its strong magnetic field will efficiently trap the few produced protons. The numerous moons within the Jovian space environment may enhance CRAND sources locally (Blake and Schulz, 1980; Roussos et al., 2021). Determining the role of CRAND will facilitate our understanding of radiation belts of encompassing planets with atmospheres.

Origin objectives: To uncover the role of distinct aspects of Jupiter's magnetospheric environment to the seeding of its radiation belts, we must address the following: 1) determine the fraction of solar wind ions in the radiation belts and if solar wind electrons may play a major role; 2) determine the role of the atmosphere in sourcing the radiation belts. To make significant progress toward understanding the roles of moon and ring materials in sourcing, sustaining and decreasing the radiation belt particles the following objectives must be addressed: 3) discover whether nuclear collision processes are a significant particle origin; 4) determine the relative roles of Io and Europa providing the source population of the radiation belts.

Mission Implementation & Science Analysis: To address these objectives, the mission design is tailored so COMPASS can 1) Measure the ion charge states and compare with chemical models that are based on the measured electron temperature. The current expectation is that higher and lower charge-state oxygen can be assumed from Io, and Europa, respectively (e.g., Smith et al., 2019). Charge states are expected to remain constant between ~10 eV and ~1 MeV because electron impact-driven reaction rates stay constant. Analysis requires an independent measurement of particle mass and charge, not just their ratio (particularly distinguishing the common species O^+ and S^{2+} that have the same M/Q ratio). This measurement is technologically easier at suprathermal than plasma energies

(Allen et al., 2019 vs. Kim et al., 2020), which is why we baseline the suprathermal SPD instrument. Interaction time scales are weeks or longer (e.g., Smith et al., 2019), meaning that this study can already be done with a very small number of orbits (≥3) that establish typical electron temperatures. 2) Determine phase space density (PSD) profiles. Such profiles will be useful tools to analyze a variety of other objectives, too. PSD maxima that persist between orbits reveal locations of ongoing source processes. The COMPASS tour is designed to ensure that PSD profiles with invariants equivalent to the full equatorial pitch angle range can be constructed. Spallation is indicated through a major local production of a broad mass distribution of heavy, fully stripped ions (including Li, Be, and N; Roussos et al., 2022) with masses and isotopes that are not the major magnetospheric species (H, O, and S). For identifying spallation as a viable process, the exact species does not need to be resolved, just the presence of a very broad mass distribution. As we are searching for the viability of this process, that analysis can be done with as little as a single orbit. CRAND is indicated through PSD enhancements in protons and electrons only. The profile of the enhancements will indicate if CRAND mostly occurs in the atmosphere or if the moons and rings are involved. The contribution of solar wind ions at radiation belt energies can be determined through species ratios such as C/O (Cohen et al., 2001). These can be accomplished at >100 keV/nuc with heritage instruments (e.g., Hill et al., 2017). Solar wind contribution particularly for electrons is supported when the PSD in the solar wind is for certain invariants higher than in the magnetosphere (e.g., Turner et al., 2021). Comprehensive measurements of the full equatorial pitch angle distribution, which are only sparsely available from earlier missions, in combination with particle tracing models will allow us to identify times when field-aligned particles, accelerated from the ionosphere, scatter into the equatorial plane. Transport models reproducing the PSD will show if the source rate is significant.

Acceleration

Background: Jupiter is well-known for its radiation belts that are both extreme in its energies as well as its intensities. The processes that accelerate particles are thought to overlap with Earth, but how Jupiter manages to exceed the terrestrial belts, and if this occurs due to a different combination of the same processes or unique processes is still a mystery. Like at Earth, acceleration processes can be separated into local acceleration and acceleration through transport that does and that does not conserve the first and second adiabatic invariants. The setup of Jupiter's magnetosphere makes it easier compared to the Earth to disentangle local from transport-related acceleration. At Earth, local acceleration—potentially non-linear mechanisms (e.g., Allanson et al., 2020)—may occur throughout all L-shells of the radiation belts (e.g., Meredith et al. 2020; Aryan et al. 2021). Even when a combination of data and modeling reveals the current combination of adiabatic transport and local acceleration, it may not be straightforward to understand which magnetospheric mechanisms trigger these acceleration modes. Observations suggest that most particle-accelerating waves in Jupiter's magnetosphere occur in the vicinity of its mass-loading moons that are located deep in the magnetosphere (e.g., Menietti et al., 2021; Sulaiman et al., 2020; green curve in Exhibit 1-5), meaning that local acceleration processes can be ruled out at range of Jupiter locations. So far there is no detailed knowledge about the relative roles of the candidate processes at Jupiter. Local acceleration may work through various plasma waves (e.g., Woodfield et al., 2014; Yu et al., 2019; Sulaiman et al., 2020, Szalay et al., 2018, Clark et al., 2020) or turbulence (Saur et al., 2021), some driven by moon-magnetosphere interaction (e.g., Clark et al., 2020). Acceleration through adiabatic transport may arise from inward radial diffusion (De Pater and Goertz, 1994; Kollmann et al., 2018; Nenon et al., 2018) driven by random field fluctuations in the magnetosphere or the ionosphere (Lejosne and Kollmann, 2020), centrifugally driven interchange (Mauk et al., 2002), or convective transport via large-scale coherent plasma flows (Hao, Sun, Roussos, et al., 2020). Non-adiabatic transport may occur during

reconnection (Vasyliunas et al., 1983; Vogt et al., 2010, Ebert et al., 2017), leading to acceleration processes similar to those found in Earth's magnetotail (e.g., Cohen et al., 2021; Turner et al. 2021).

Acceleration objectives: We parse this goal into the following objectives: 1) reveal how particles are pre-conditioned to < 1 MeV energies and transported to L < 30; 2) determine where and via which processes, radiation belt particles with the difference species are accelerated locally; 3) uncover the drivers responsible for radial transport of > 1 MeV charged particles.

Mission Implementation & Science Analysis: To address these objectives, COMPASS must *cleanly* measure energy- and pitch-angle-resolved differential electron and ion fluxes together with plasma waves of both low and high frequencies. 1) Phase space density (PSD) profiles will be constructed and reproduced with numerical models involving all relevant physics, including local acceleration constrained through 3D wave measurements (e.g., Turner et al., 2012; Woodfield et al. 2014; Li et al., 2016; Shprits et al., 2008). Electron spectra often show a cutoff somewhere in the tens of MeV energy range (Kollmann et al., 2018; blue curve in Exhibit 1-5). Thus far, it has only been resolved down to L~15 (orange curve in Exhibit 1-5); however, with large uncertainties due to limitations of the available data. Searching for its presence inside of L~15 and mappings its L-Shell and pitch angle dependent location (Sun et al., 2019) would reveal if adiabatic transport has a significant role throughout the radiation belts and if coherent radial plasma flows are responsible for it (Hao et al., 2020). Resolving its location with accuracy allows for comparison with expectations for adiabatic heating. 2) Different transport mechanisms have different energy- and species-dependent signatures that will be identified through in-situ and remote measurements. Remote measurements of transport signatures can generally be done through the following: Observations of X-rays created by inverse Compton scattering of radiation belt electrons (> ~10 MeV) on photons (Numazawa et al., 2019) or X-rays created charge exchange or stripping reactions of several MeV heavy ions in the Io torus or through synchrotron emission. The COMPASS spacecraft baselines X-ray instead of synchrotron observations because they require less resources and resolve the energy of the involved particles with less ambiguity. Additionally, synchrotron emission is only sensitive to electrons, while X-rays can be emitted by interactions of both energetic ions and electrons. Finally, synchrotron requires those energetic electrons to be imbedded in a strong magnetic field, which is why relevant emissions are mostly visible between ~1.5 to 3 Jovian radii. Large-scale convection results in energy- and species-dependent "zebra stripe" patterns in energy spectrograms (Ukhorskiy et al., 2014) that have been predicted, but not observed with the available integral energy measurements, at Jupiter (Hao, Sun, Roussos et al., 2021), and energy-dependent displacement of moon absorption signatures (so far could only resolved at Saturn, e.g., Andriopoulou et al., 2014), radial plasma flows (e.g., Wilson et al., 2013), and local time asymmetries in in-situ and remote measurements. Extreme solar wind-driven space weather events may also contain signatures of radial transport, at global or local scales (e.g., Hao et al., 2020). Extreme transient events may not occur during the COMPASS mission duration but if they do, they can be identified from within the magnetosphere through foreground decreases in GCR measurements without an upstream monitor, since COMPASS can resolve the low-energy tail of the GCR spectrum, which efficiently penetrates into the Jovian magnetosphere down to Europa's orbit (e.g., Selesnick, 2002; Roussos et al., 2018). A powerful method to infer the presence and further characterize the efficiency of radial diffusion is to observe refilling of moon absorption signatures with increasing longitudinal distance to the moon. This method has been applied to Jupiter in principle (e.g., Mogro-Campero 1976, Thomsen et al., 1977, Thomsen 1979) but was limited by the low signal-to-noise of previous measurements. Drivers of the diffusive processes may be determined though correlation. Correlation of transient radiation belt enhancements indicated through synctrotron emissions with independently measured solar EUV input into the Jovian atmosphere suggested that the driver of diffusion could be ionosphere driven (Tsuchiya al., 2011). This would however require a diffusion coefficient with an L-shell dependence different to what theory predicts

for this mechanism (e.g., Lejosne and Kollmann, 2020), an issue that may be resolved through monitoring of Jupiter's belts with COMPASS.

Loss

Background: While acceleration processes draw a lot of attention, it is critically important to also understand losses because without them, intensities would accumulate indefinitely. Like at Earth, Jupiter loses particles via precipitation to the atmosphere. Magnetopause shadowing plays no role for Jupiter's belts because its magnetopause is so far out. Its moons, rings, and gas tori on the other hand are so close in that they orbit within the radiation belts, leading to a prevalence of loss processes that at the Earth only occur for precipitating particles (e.g., Nénon et al., 2017, 2018). Moons may even be so efficient sinks that they decouple what would have been single, continuous radiation belt, into multiple belts, that are strictly separated at the moon orbits and that achieve at best limited particle exchange among them, as is the case of Saturn (e.g., Kollmann et al. 2013) and possibly Jupiter (Roussos et al. 2022). Past studies on loss processes were often based on observing losses during close moon flybys, observing particles within loss cones, and calculating precipitation based on wave observations. These methods have the disadvantage that they are working locally in time and space, while not all particles in the geometric path of the moon precipitate onto it, particularly for moons with faint ionospheres (e.g., Nordheim et al., 2018; Roussos et al., 2012). Some moons may completely clear out their orbits, meaning that there is no steady state precipitation anymore. Also, particle precipitation is very dynamic in time and space (e.g., Mauk et al., 2019, 2021), making it difficult to build up a global picture through in-situ measurement. COMPASS will add to these methods the use of remote X-ray observations that globally image the precipitation onto Jupiter's atmosphere and moon surfaces, where they leave valuable signatures that so far have only been leveraged at other planetary bodies (e.g., Starr et al., 2012).

Loss objectives: COMPASS must address the following key objectives: 1) determine the contributions of atmospheric precipitation to overall radiation belt dynamics and 2) determine if the moon and ring orbits are hard barriers for Jupiter's radiation belt particles.

Mission Implementation & Science Analysis: 1) While in-situ measurements provide signatures of particle losses, there often is an ambiguity between losses caused to equatorial material (moon and rings themselves) and scattering losses into the atmosphere (particularly for in-situ measurements that cover the full pitch angle distribution but not resolve the loss cone).

Global imaging of the atmosphere (as facilitated through the two orbit phases) will indicate with little ambiguity over which volume in Jupiter's magnetosphere scattering losses develop. Imaging of 0.2-1.5 keV x-rays will sample the precipitation of charge exchanging ions. 0.2- 20keV x-rays sample electron precipitation through their emitted bremsstrahlung. (The actually measured energy range may be smaller.)

These imaging results will then be compared through the in-situ measurements that COMPASS also provides. COMPASS will use a combination of in-situ particle distribution functions and 3D wave measurements in order to determine the expected precipitation rate of particles (e.g., through a Fokker-Planck formalism, Nénon et al. 2017, W. Li et al., 2021). Note that atmospheric precipitation is not only affected through waves but also a result of pitch angle friction resulting from synchrotron emissions (e.g., Santos-Costa et al., 2001), an effect that so far was not observed in-situ because it requires the angle and energy resolved measurements of >10MeV electrons that will be provided by COMPASS.

2) Inverting x-ray measurements of moons and rings will characterize the effective particle loss rates. This approach requires information about either the moon's surface composition or the incident energy spectrum. In the case of COMPASS, we will measure the energy spectrum in-situ, meaning

that bonus science can be done on the moon's surface composition. Particularly its non-ice components are difficult to determine in other wavelengths and key to understand the moon's geology.

Precipitation rates determined like this may be more reliable than analyzing data from a close flyby through the highly structured moon environment. Numerical modeling of near-equatorial PSD profiles will then reveal efficiency of absorption at moons and rings. Analyzing how PSD develops with longitudinal separation from the moon informs if the loss mechanism is purely collisional (absorption at the surface), or enhanced by wave activity that even inactive moons appear to generate (e.g., Arkyphov and Rucker, 2007; Zarka et al. 2017).

A.2 Pitch Angle & Corotation Coverage

Charged particles bounce along magnetic field lines depending on their equatorial pitch angle. Energetic ions and all electrons organize mostly with pitch angle. Low energy plasma on the other hand flows along the corotation direction. In order to fully characterize the particle distributions, COMPASS needs to be able to cover a large range of equatorial pitch angle and at least the nominal corotation direction. Equatorial pitch angle coverage at Jupiter is always a challenge because the magnetic and rotational equator planes are tilted, meaning that a spacecraft orbit never stays in the magnetic equator, and because the magnetic field lines are stretched tail-like already in the middle magnetosphere (Connerney et al. 2020), meaning that even small magnetic latitude limit the equatorial pitch angle coverage. Exhibit A-1 shows that our chosen tour still manages to build up full equatorial pitch angle coverage—assuming a single look direction (or telescope) instrument—through combining neighboring orbits. Instantaneous pitch angle gaps will be mitigated by filling them with information from other orbits (as in Smirnov, 2022). Coverage of the nominal corotation direction would be patchy when using a single instrument. Different to the equatorial pitch angle coverage that mostly depends on the magnetic latitude, the local coverage of the corotation direction can be fixed through adding another instrument (Exhibit A-2), which is why we baseline two plasma sensors.

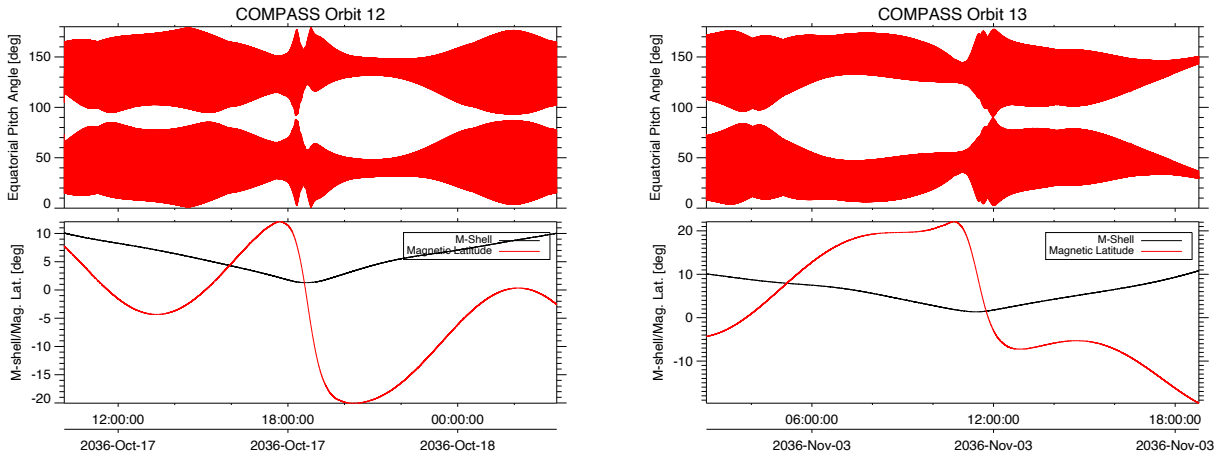

Exhibit A-1: Upper panels: Equatorial pitch angle coverage by a single telescope instrument mounted perpendicular to the spacecraft spin plane for orbits 12 & 13. Lower panels: Location of COMPASS in L-shell and magnetic latitude, calculated in the JRM09+CAN magnetic field (Connerney et al., 1981, 2018). The two panels show two example orbits in science phase 2 where pitch angle coverage is most critical. It can be seen that coverage is not continuous, but full equatorial coverage can be accomplished by combining neighboring orbits.

Instruments with multiple instantaneous look directions (such as Juno/JEDI, Mauk et al., 2017) can obtain more complete instantaneous pitch angle coverage (Exhibit A-3). And finally, Exhibit A-4 illustrates the sampling duration of equatorial pitch angles as a function of M-shell (using the Connerney et al., 2018 magnetic field model) for all COMPASS orbits.

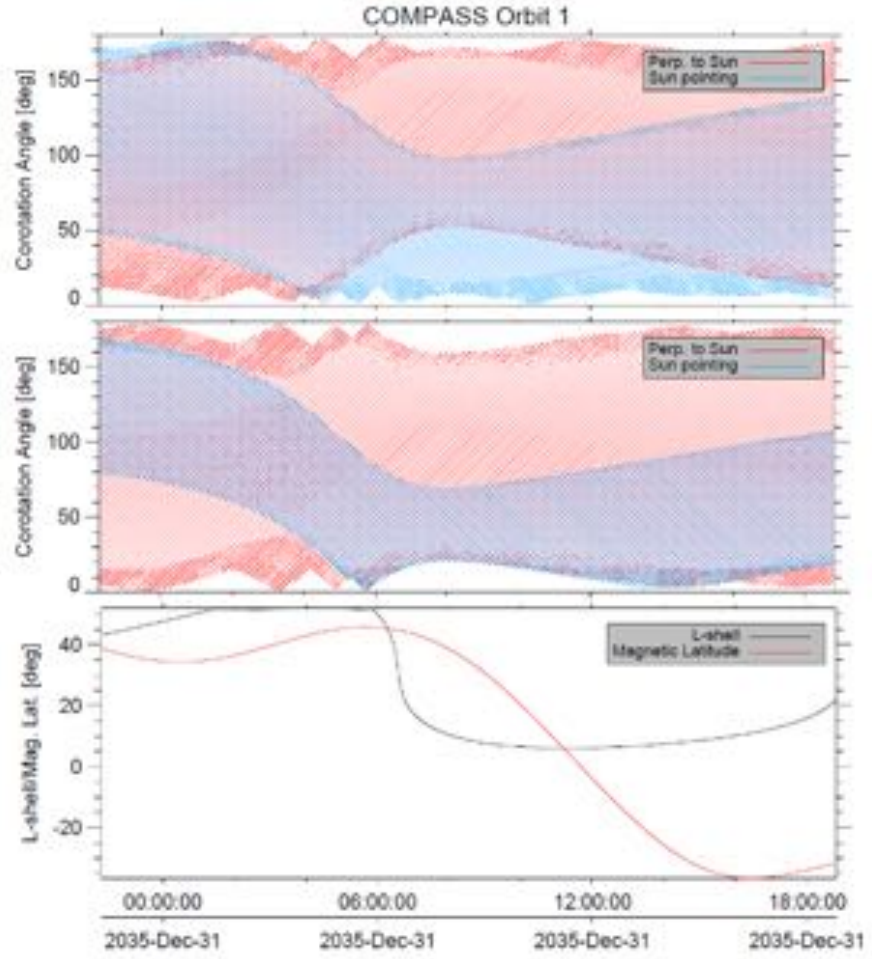

Exhibit A-2: Coverage of the corotation direction using two TPD instruments (red and blue) illustrated based on the example of orbit 1. Upper panel: baseline mission with two instruments that are tilted 30deg from the spin axis. It can be seen that they cover the corotation direction at all times. Further optimization may be possible to extend the coverage toward the <10deg directions. Middle panel: The two instruments are pointed perpendicular and parallel to the spin axis. It can be seen that the perpendicular instrument alone is able to cover almost directions and that the parallel one can be descoped if necessary. Lower panel: L-Shell and magnetic-latitude coverage of COMPASS in orbit 1.

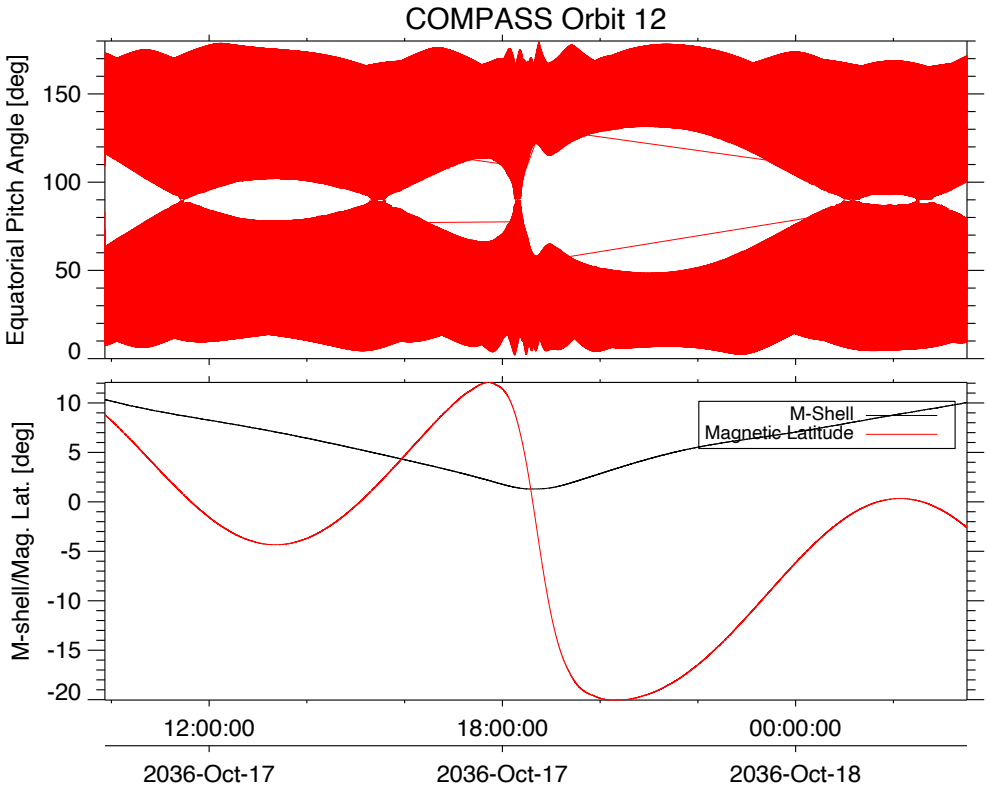

Exhibit A-3: Same format as A-1, but instead using a multi-look direction instrument such as Juno/JEDI.

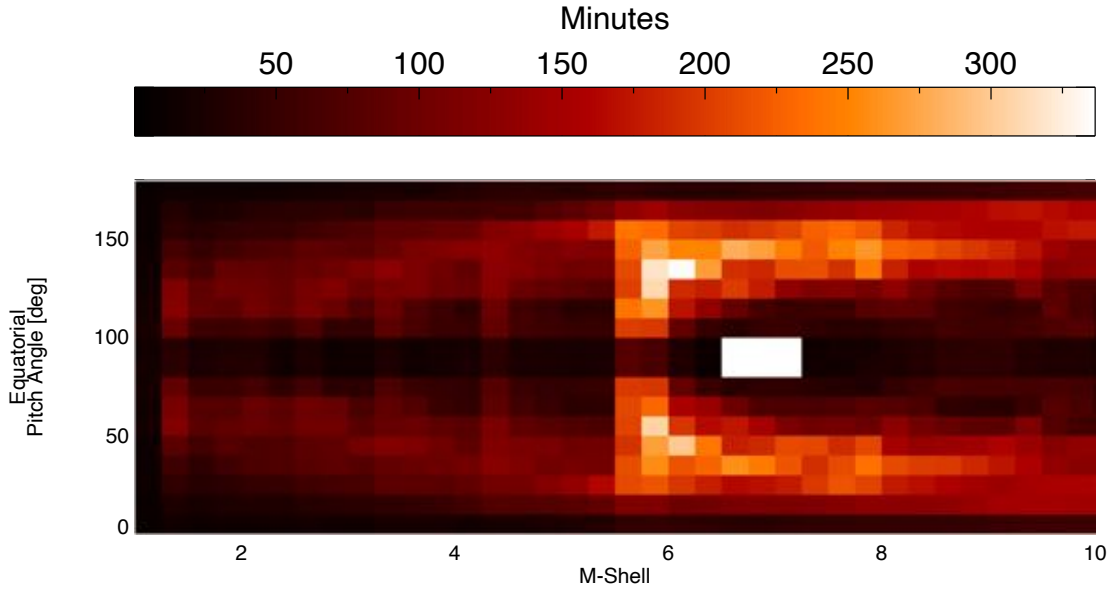

Exhibit A-4: Color coded sampling durations as a function of equatorial pitch angle and M-shell for all COMPASS orbits.

A.3 Magnetic Latitude Coverage

An important requirement for COMPASS is to ensure complete PAD coverage (see discussion above) to reveal acceleration, loss, and transport processes in the inner-most regions. Therefore, Jovigraphic and magnetic latitude requirements were imposed on the design tour. Exhibit A-5 illustrates the magnetic latitude coverage of COMPASS over both science phases as well as the transition phase. In the second science phase, it can be seen that COMPASS is able to skirt along magnetic latitudes < 10°, which is critically important.

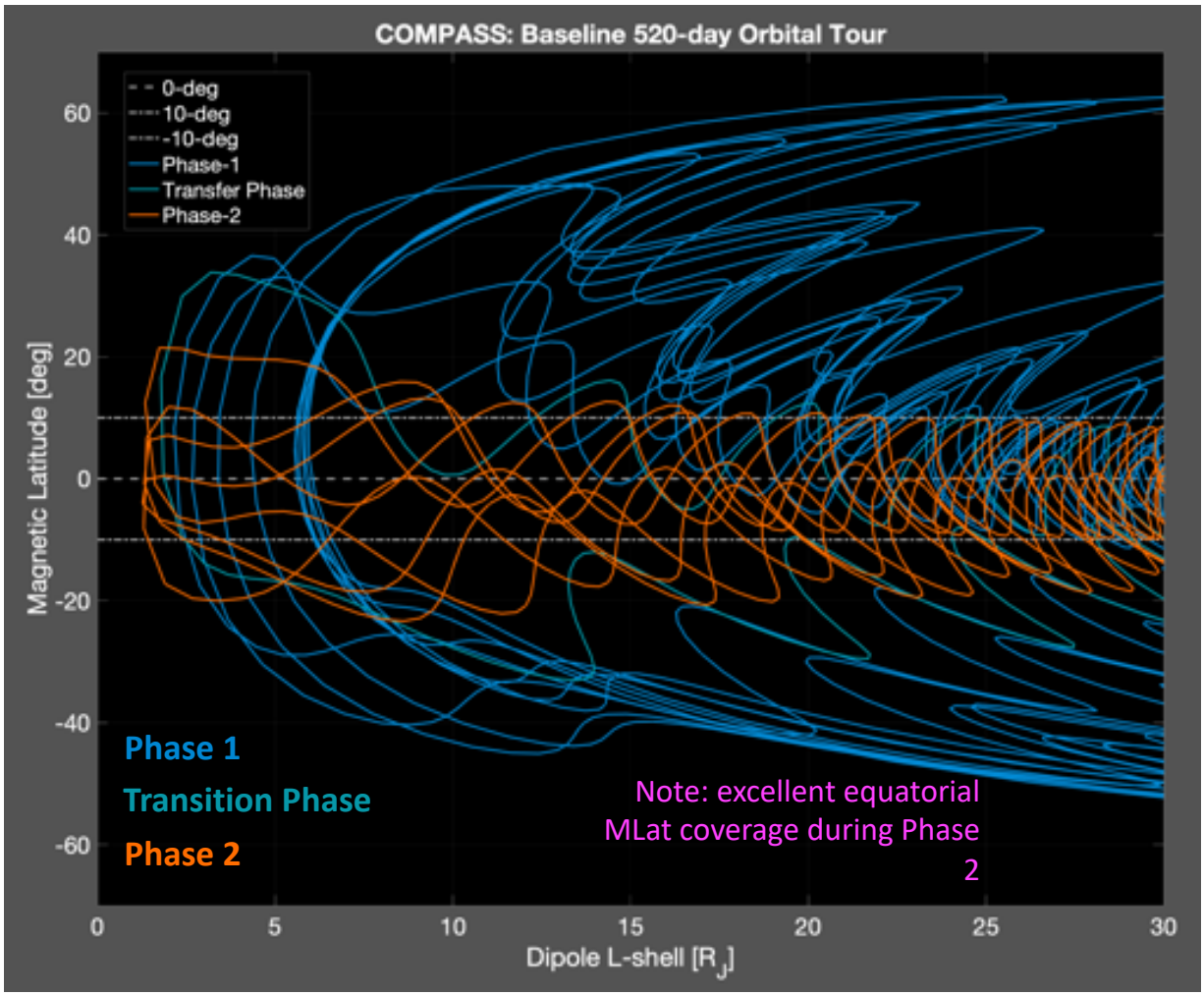

Exhibit A-5: Magnetic latitude coverage of COMPASS for science phase 1 (blue trajectories) and science phase 2 (orange trajectories).

A.4 Spatial coverage of the Jovian moons

Repeated Io and Callisto flybys are utilized to reduce the orbit period and apojove as well as reduce the inclination and perijove distances. Although the flybys are not tied to the baseline or threshold science requirements, there does exist many enhancing, cross-divisional, science opportunities. For example, the X-ray imager on board COMPASS is capable of measuring fluorescence emitted from

the moon's surfaces. Exhibits A-6 and A-7 illustrate the flyby trajectories in a moon-centered coordinate system as well as the longitudinal coverage, respectively.

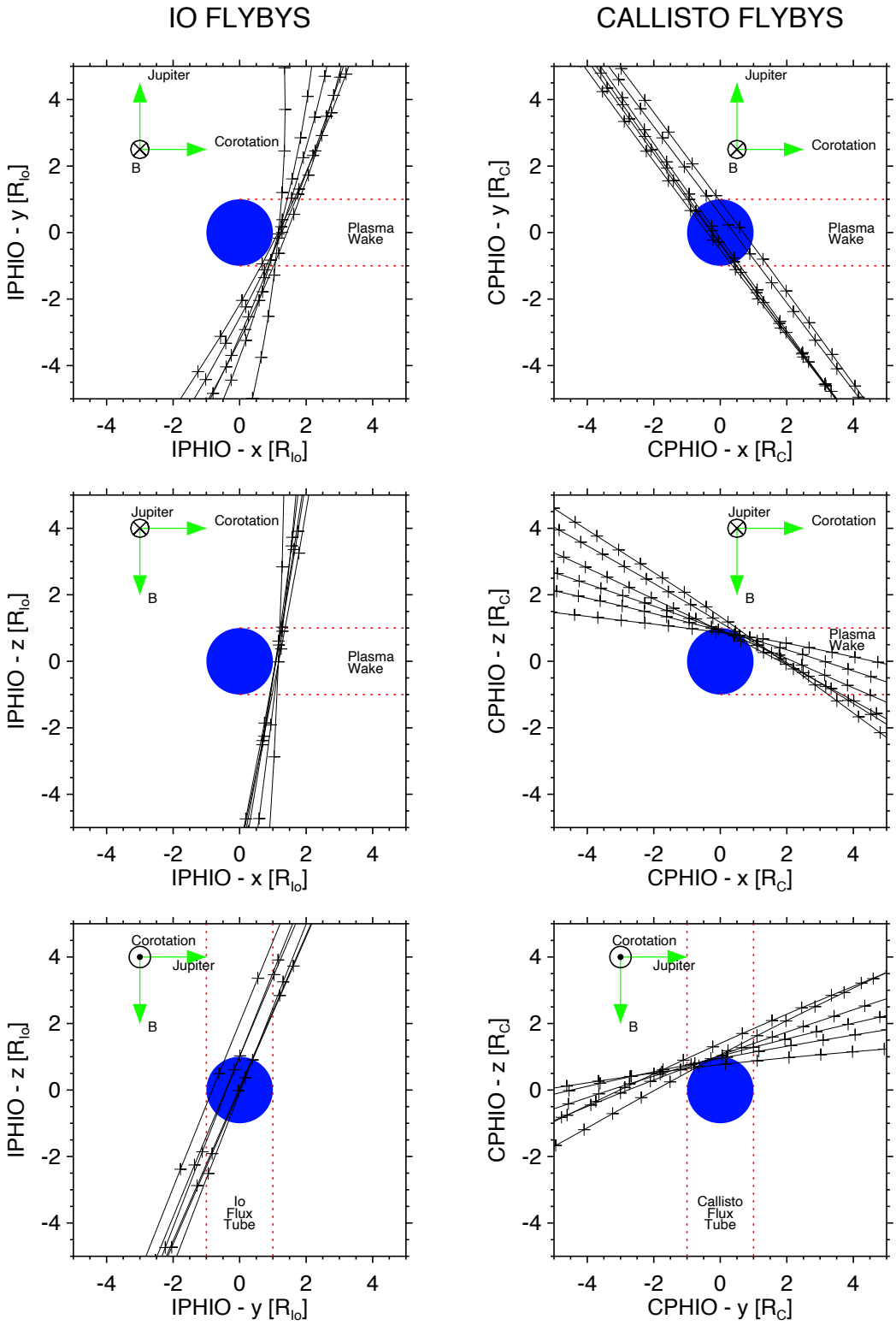

Exhibit A-6: COMPASS flyby trajectories in a moon-centered coordinate system for both Io (left panels) and Callisto (right panels). Dashed red lines illustrate the approximate geometrical wake and flux tube locations. In reality, these are tilted and depend on the moon's location with respect to the Jovian current sheet, but this is not taken into account here.

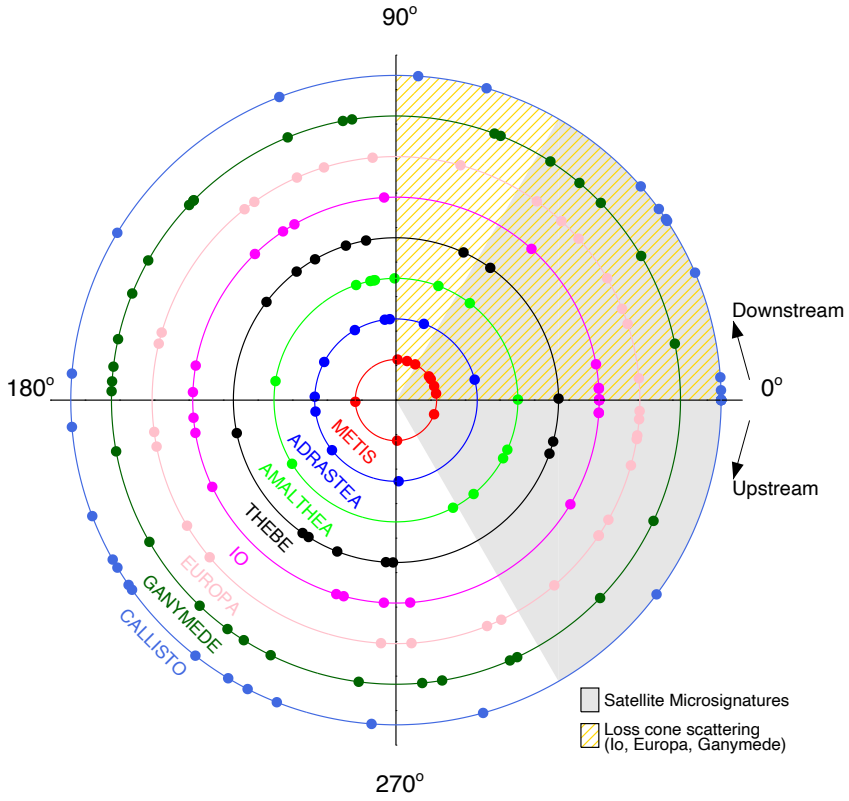

Exhibit A-7: Polar projection illustrating COMPASS' longitudinal coverage of the various Jovian moons. In addition to the Galilean moons, COMPASS will make repeated passes of the inner-most moons that are relatively unexplored. The shaded regions highlight a set of longitudes where we expect to carry out observations associated with satellite microsignatures (gray shading) and processes associated with loss cone scattering (beige shading).

Appendix B. Mission Design Trade Studies

B.1 Launch and Interplanetary Trade Study

For COMPASS, two Launch Vehicles (LVs) are considered, the Falcon Heavy Recovery (FHR), and the Falcon Heavy Expendable (FHE). The lift capability for the FHR generally enables two interplanetary options: (1) a VEEGA (inner cruise, Venus-Earth-Earth Gravity Assist), and (2) a 2:1 ΔV-EGA (ΔV-Earth Gravity Assist, with launch into a roughly 2-year resonance with Earth). Considering the FHE, a third itinerary becomes available: (3) 3:1 ΔV-EGA (ΔV-Earth Gravity Assist, with launch into a roughly 3-year resonance with Earth). A summary of the general characteristics of these options is provided in Exhibit B-1. Note that all 3:1 ΔV-EGA solutions are constrained such that time-of-flight to Jupiter is ≤ 5.5 years. Two rows appear under the DSM ΔV for each itinerary. The first row provides an estimate for the total deterministic ΔV over the interplanetary itinerary; the second row is given in parenthesis, and estimates statistical ΔV for flyby targeting and clean-up. The statistical ΔV assumed is 25 m/s for Venus, and 50 m/s for Earth flybys to account for the possibility of implementing an Earth-biasing strategy. For properties that depend on planetary geometries, such as ΔV magnitudes, a range of values is provided to reflect variation with launch year. An enabling feature of the VEEGA inner cruise option is the low C3 that allows a higher lift mass. Additionally, for some launch years the VEEGA does not require deterministic ΔV, reducing the required propellant mass. Additional details on the VEEGA and other cruise options to Jupiter can be found in (Petropoulos, Longuski & Bonfiglio, 2000).

Exhibit B-1: Launch and interplanetary trade-space

LV	Itinerary	Max C3 (km^2/s^2)	Lift Mass (kg)	Years to Jupiter	Arrival V_∞ (km/s)	*DSM (m/s)
FHR	VEEGA	25	3270	5.5 – 7.5	5.7 – 6.4	0 – 500 (125)
FHR	2:1 ΔV-EGA	31	2645	4.5 – 5.5	5.5 – 6.2	535 – 700 (50)
FHE	3:1 ΔV-EGA	52	5035	5.5 – 6.0	5.8 – 6.4	175 – 275 (50)

* DSM range listed represents estimated maximum deterministic DSM ΔV over a 21-day launch period

While potentially feasible for many launch years with the FHR LV, the inner cruise interplanetary option offers challenges with regard to the spacecraft thermal design. The additional required propellant mass for the 2:1 ΔV-EGA DSM leads to a spacecraft wet mass that likely exceeds the lift capability of the FHR. For these reasons, the FHE LV with the 3:1 ΔV-EGA interplanetary itinerary are selected for the COMPASS design. Note that changes to the interplanetary trajectory, e.g., from changing LV, have minimal impact to the subsequent mission phases. Assuming the 3:1 ΔV-EGA cruise option, launch periods of ≥ 21 days are built from 2030 – 2042 to quantify the maximum expected DSM and JOI ΔV, as summarized in Exhibit B-2. For each launch day in a particular period, the Jupiter arrival date is constrained to a single epoch, enabling the design of a single capture sequence and science tour for each launch year. This launch period analysis is performed in a patched-conic model, and arrival date and V_∞ are therefore estimates.

A high-fidelity launch period is constructed for a 2030 launch, with details provided in Exhibits B-3 & B-4 for comparison. For all cases, JOI is estimated as an un-aided (no Io flyby prior to JOI) capture maneuver that inserts the spacecraft onto a 150-day orbit about Jupiter. The 2030 launch is among the most stressing in terms of the DSM and JOI ΔV required, and the COMPASS ΔV includes sufficient unallocated margin to accommodate the worst-case launch years of 2040-2042. In addition, the mission design could be adjusted for these launch years to reduce the required ΔV

(e.g., maintaining two Jupiter arrival dates, and/or reducing JOI by capturing into a higher orbital period).

Exhibit B-2: Launch period estimates for 3:1 ΔV-EGA (C3 ≤ 52 km²/s²), patched-conic model

Launch Year	Launch Period	Arrival Date	Arrival V_∞ (km/s)	Max DSM (m/s)	*JOI (m/s)	DSM + JOI (m/s)
2030	Mar 31 – Apr 22	Jul 18 2035	6.3	217.1	1125.7	1342.8
2031	May 09 – May 31	Nov 05 2036	5.8	195.0	1004.9	1199.9
2032	Jun 10 – Jul 01	Nov 17 2037	5.8	188.5	1004.9	1193.4
2033	Jul 18 – Aug 08	Dec 17 2038	5.9	236.6	1028.3	1264.9
2034	Aug 19 – Sep 08	Jan 15 2040	6.1	256.4	1076.2	1332.6
2035	Sep 18 – Oct 11	Mar 18 2041	6.1	261.1	1076.2	1337.3
2036	Oct 17 – Nov 08	Apr 15 2042	6.2	233.3	1100.8	1334.1
2037	Nov 16 – Dec 10	May 14 2043	6.2	190.4	1100.8	1291.2
2038/9	Dec 15 – Jan 11	May 18 2044	6.4	178.5	1150.9	1329.4
2040	Jan 18 – Feb 14	May 09 2045	6.4	204.9	1150.9	1355.8
2041	Feb 25 – Mar 22	Jun 12 2046	6.4	217.1	1150.9	1368.0
2042	Apr 07 – Apr 29	Sep 14 2047	6.0	218.2	1052.1	1270.3

* JOI estimated for periapsis at 6 R_J, no Io flyby before JOI, with capture into 150-day orbit

Exhibit B-3: Launch period for 2030 3:1 ΔV-EGA interplanetary cruise (C3 ≤ 52 km²/s²), high-fidelity

Launch Year	Launch Period	*Arrival Date	Arrival V_∞ (km/s)	Max DSM (m/s)	**JOI (m/s)	DSM + JOI (m/s)
2030	Mar 31 – Apr 20	Aug 03 2035	6.3	226.2	871.7	1097.9

* Arrival date adjusted to optimize phasing for Io-Callisto transfer during COMPASS science tour

** Assumes Io-aided JOI, with capture into 150-day orbit

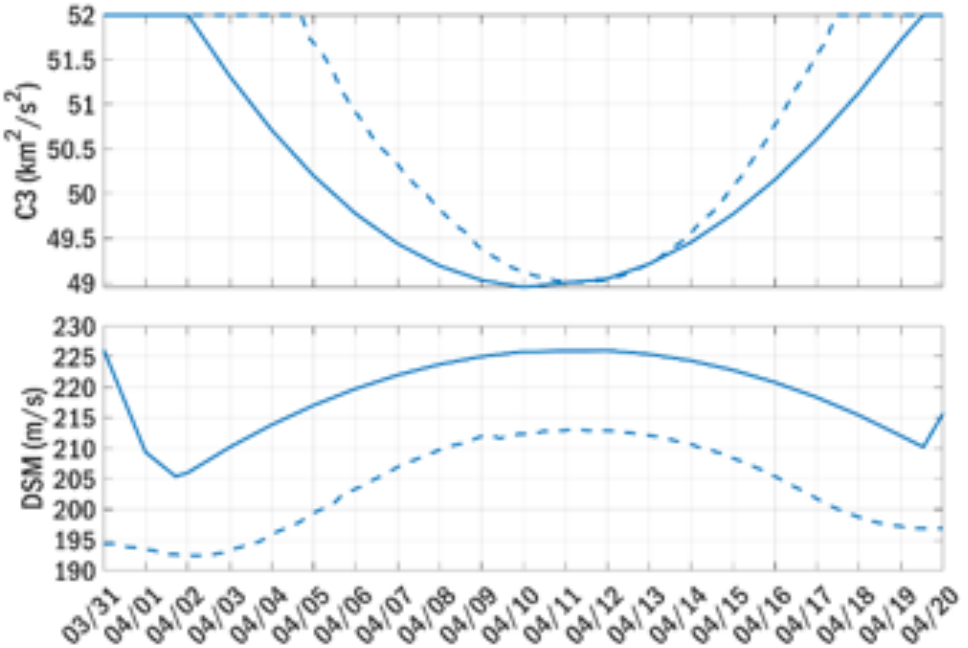

Exhibit B-4: Comparison of patched-conic (dashed line) and fully integrated high-fidelity (solid line) launch periods. Note that the arrival date is adjusted for the high-fidelity solutions to optimize phasing for the Io-Callisto transfer during COMPASS science tour.

Exhibit B-5: Comparison of capture sequence options

Sequence	Capture Period (days)	Io Flyby Alt. (km)	JOI Altitude	JOI (m/s)	PRM (m/s)	JOI+PRM (m/s)
Io-aided JOI	150	300	6.22 RJ	872	22	894
Low-altitude JOI	150	-	4200 km	393	367	760

B.2 Capture Sequence Trade

Two capture sequences are considered for this study: (1) Io-aided JOI: Io flyby (I1), followed by JOI 1-hour after I1; (2) un-aided, low-altitude JOI: JOI ΔV performed at low perijove, similar to Juno. A comparison of each option appears in Exhibit B-5. Note that while the Io-aided JOI values are computed from the final high-fidelity solution, optimized from launch through end of science operations, the low-altitude JOI sequence assumes a patched-conic analysis. Transitioning the low-altitude sequence to high-fidelity, the PRM magnitude is expected to increase on the order of the Io-aided PRM ΔV. Clearly, the low-altitude JOI offers significant propellant savings over the Io-aided sequence, even with the significant increase in PRM required to target the subsequent Io-flyby.

The geometry of each capture sequence is shown in Exhibit B-6. For an Io-aided JOI, the ascending node crossing falls at 41 RJ while, for the low-altitude JOI option, the ascending node is much further out at around 110 RJ. In the COMPASS tour design, the initial Io pump-down sequence serves to reduce orbital period, but also to align the ascending node with Callisto (~26.5 RJ) to enable transfer from Io to Callisto to begin the crank-down phase of the tour. This strategy is infeasible for the low-altitude JOI option due to the large initial distance of the ascending node. Correcting the node location inward via adjustment during interplanetary cruise requires prohibitively large ΔV. Due to the challenges of implementing the current science tour design strategy with the low-altitude JOI sequence, the Io-aided JOI option is assumed for COMPASS.

B.3 Science Tour

A summary of the orbit-changing events (flybys and maneuvers) along the science tour is provided in Exhibit B-7. This table demonstrates the evolution of the tour through these discrete events, and includes a description of the intent for each event. Alternatively, a visual representation of the tour evolution is available through Tisserand surfaces (Heaton et al. 2002; Campagnola & Kawakatsu 2012). The COMPASS pump-down is depicted in Exhibit B-8 (a) as it evolves along the Tisserand surface of Io $V_\infty \approx 19$ km/s. The pump-down terminates near the intersection with the surface of Callisto $V_\infty = 9.4$ km/s. The transfer from the Io pump-down to the Callisto crank-down is pictured in Exhibit B-9 (b), with maneuvers included as red points.

Note that the true V_∞ fluctuates along the pump-down, thus, while these surfaces offer a close approximation, the paths do not exactly follow the surfaces. Two perspective views of the Io and Callisto flybys appear in Exhibit B-9. During the pump-down, all Io flybys are over the leading hemisphere to reduce orbital energy;

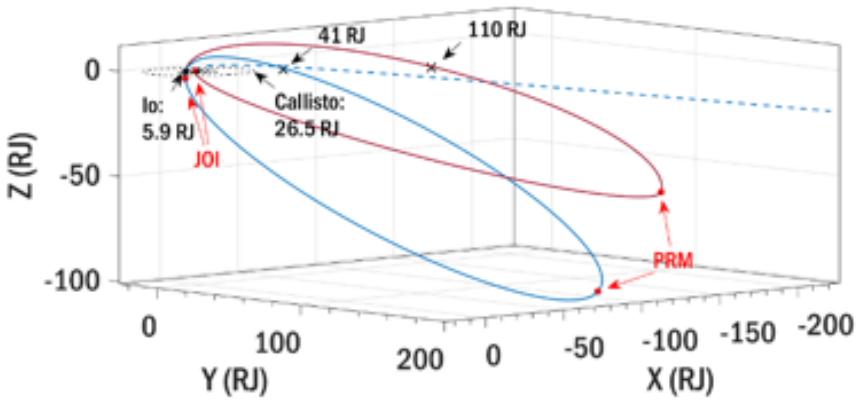

Exhibit B-6: Comparison of geometry for Io-aided (blue) and Juno-like capture (red), ascending nodes indicated with dots and labeled by Jovian distance (both solutions inclined 50° relative to Jovian equator).

Exhibit B-7: Summary of flybys and maneuvers over the COMPASS science tour.

Maneuver	Maneuver Date	ΔV (m/s)	Flyby	Flyby Date	V_∞ (km/s)	Period (days)	Intent
			I1	Aug 03, 2035	18.86	-	Flyby: Reduce energy
JOI	Aug 03, 2035	871.7				155.8	Maneuver: Capture into Jovian orbit
PRM	Oct 14, 2035	22.3				150.9	Maneuver: Counteract solar perturbations to re-target Io
			I2	Dec 31, 2035	18.68	71.5	Flyby: Reduce energy / period
I3-targeting	Feb 15, 2036	13.4				70.9	Maneuver: Counteract solar perturbations to re-target Io
			I3	Mar 11, 2036	18.90	44.6	Flyby: Reduce energy / period
I4-targeting	Apr 06, 2036	5.8				44.2	Maneuver: Counteract solar perturbations to re-target Io
			I4	Apr 24, 2036	18.95	33.7	Flyby: Reduce energy / period
I5-targeting	May 14, 2036	1.7				33.6	Maneuver: Counteract solar perturbations to re-target Io
			I5	May 28, 2036	18.97	24.9	Flyby: Reduce energy / period
I6-targeting	Jun 10, 2036	1.2				24.8	Maneuver: Counteract solar perturbations to re-target Io
			I6	Jun 21, 2036	18.98	19.1	Flyby: Reduce energy / period
C1-targeting	Jun 21, 2036	37.4				18.4	Maneuver: Target Callisto
			C1	Jul 07, 2036	9.36	16.7	Flyby: Reduce r_p/i
			C2	Jul 24, 2036	9.35	16.7	Flyby: Reduce r_p/i
C3-targeting	Jul 31, 2036	9.5				16.7	Maneuver: Counteract Jupiter J2 to re-target Callisto
			C3	Aug 10, 2036	9.36	16.7	Flyby: Reduce r_p/i
C4-targeting	Aug 17, 2036	11.0				16.7	Maneuver: Counteract Jupiter J2 to re-target Callisto
			C4	Aug 27, 2036	9.37	16.7	Flyby: Reduce r_p/i
C5-targeting	Sep 03, 2036	20.1				16.7	Maneuver: Counteract Jupiter J2 to re-target Callisto
			C5	Sep 12, 2036	9.39	16.7	Flyby: Reduce r_p/i
C6-targeting	Sep 20, 2036	34.4				16.7	Maneuver: Leveraging to slightly increase V_∞ + counteract Jupiter J2 to re-target Callisto
			C6	Sep 29, 2036	9.45	15.0	Flyby: Reduce period to drop r_p and i while preserving Callisto V_∞
Disposal	Nov 07, 2036	150.0				15.0	Maneuver: Reduce r_p to ensure Jupiter impact

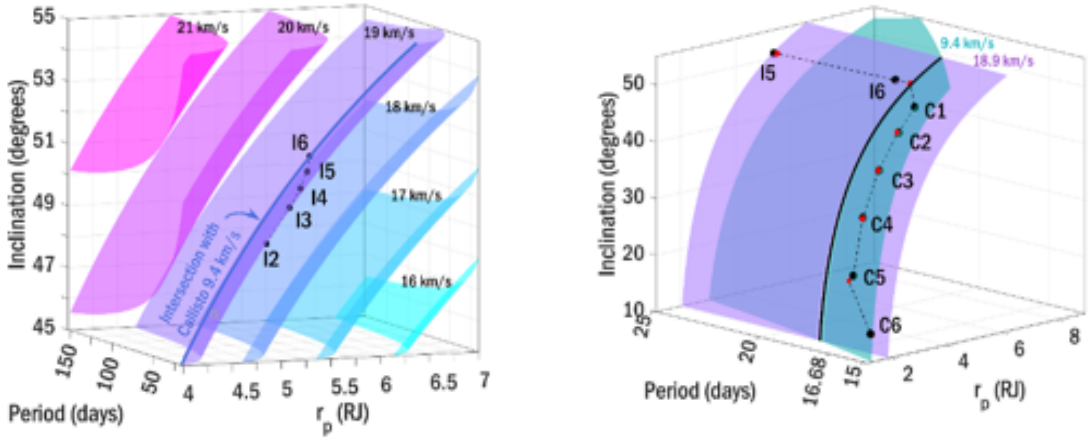

Exhibit B-8: Science tour evolution from the perspective of Tisserand surfaces: (a) Io pump-down, with flybys included as black points (b) connection between pump-down and crank-down sequences, flybys and maneuvers included as black and red points, respectively.

during the crank-down, each Callisto flyby is designed to preserve orbital period, while reducing perijove and inclination.

B.4 Disposal

Because Science Phase II operations are in a high-radiation environment, it is important for the disposal strategy to incorporate an increased risk of s/c failure. Two disposal options are identified for COMPASS: (1) disposal maneuver to reduce perijove, resulting in Jupiter impact, and (2) Callisto impact. For the Jupiter impact strategy, the disposal maneuver can be designed to reduce perijove such that it remains above Jupiter's atmosphere for some duration, but Jupiter gravity harmonics lead to eventual impact. Because the orbit is inclined, it spends most of the duration outside of the moon plane, minimizing the risk of a Europa impact. However, the orbit node crossings will drift as a result of Jupiter J2, and could cross the orbit of Europa. A conservative planetary protection stance is to ensure Jovian impact occurs prior to the crossing of either orbit node with Europa's orbit. A time history of the post-disposal orbit evolution for COMPASS appears in Exhibit B-10 demonstrating that the spacecraft will impact Jupiter ~74 days prior to the first node crossing with Europa's orbit. Even should that node crossing occur prior to impact, the probability of both the spacecraft and Europa being *at* the node crossing on that revolution is very low.

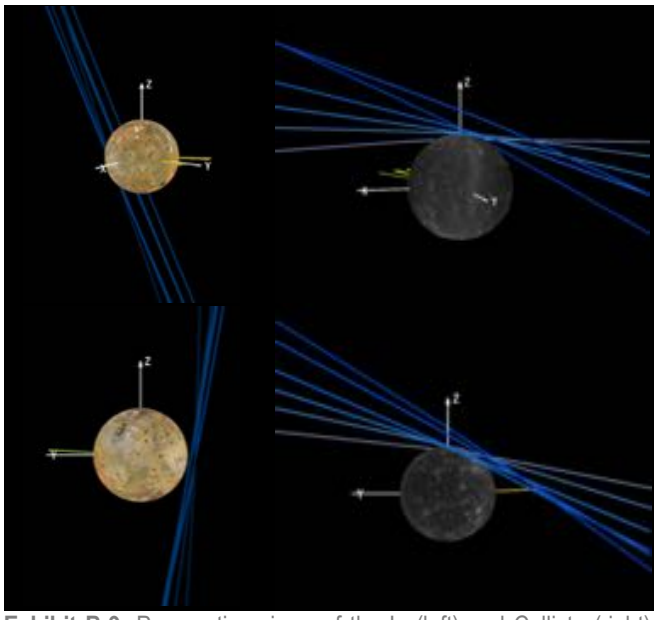

Exhibit B-9: Perspective views of the Io (left) and Callisto (right) flybys, with extremes of Sun- and Earth-point vectors over the flyby date range plotted in yellow and green, respectively.

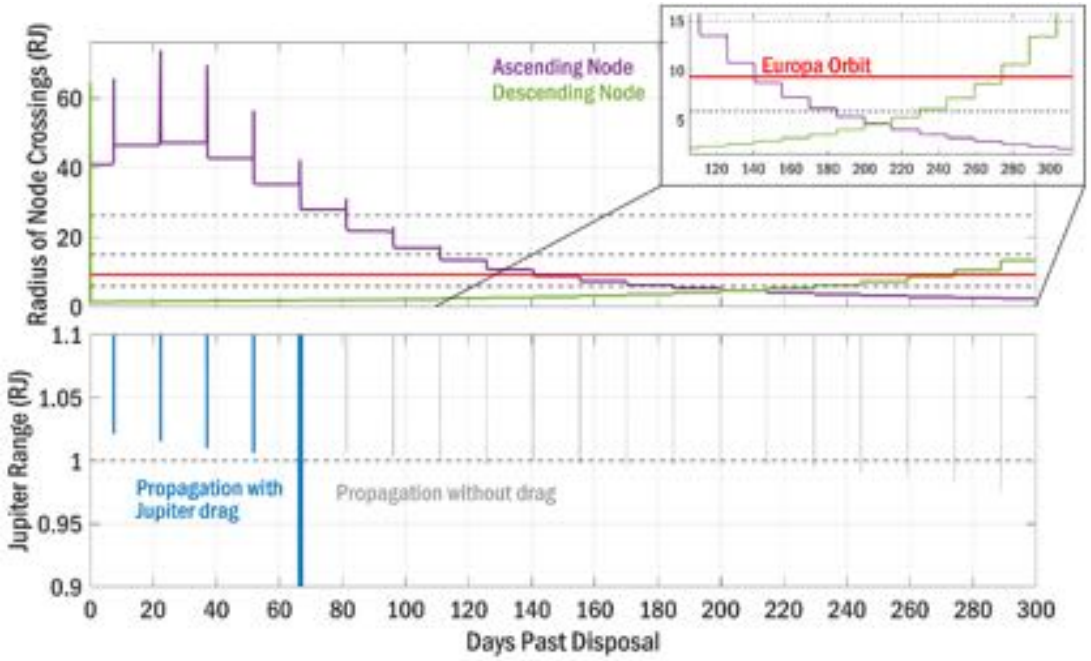

Exhibit B-10: Orbit evolution after disposal maneuver, COMPASS impacts Jupiter 66 days after disposal, while the ascending and descending node crossing do not cross Europa's orbit until 140 and 274 days after impact, respectively

Alternatively, because a portion of the tour exploits Callisto flybys to adjust the orbit perijove radius and inclination, a Callisto disposal option could be considered. As a conservative strategy, assuming a Callisto flyby on every revolution about Jupiter in Science Phase II, Callisto impact could be planned as the nominal behavior for each flyby. Should the s/c survive to execute it, a divert maneuver executed ~8 days prior to impact would increase the flyby altitude to a non-zero value to enable one additional revolution about Jupiter. This strategy incurs an increasingly large ΔV penalty as the mission continues into extended operations. Once in Science Phase II operations, the Callisto flybys must be at high altitudes of ~5000 km for the orbit to remain bounded within the Science Phase II r_p - i constraints. The estimated divert maneuver for these altitudes is ~15 m/s per flyby. Because the low inclination and perijove conditions of Science Phase II cause J2 perturbations to drive the orbit away from a return to Callisto, the ΔV to continue targeting Callisto flybys to become prohibitively expensive. For these reasons, the Jupiter impact option is selected for COMPASS.

B.5 Design Tools

COMPASS interplanetary trajectory and moon-tour broad searches are performed using the Moon-tour and Interplanetary eXplorer (MInX) software, developed at the Johns Hopkins University Applied Physics Laboratory. MInX provides an adaptable framework for the construction of resonant arcs, transfer design via Lambert solvers, and V_∞-leveraging transfer (VILT) algorithms. Patched-conic analysis is exploited for rapid generation of theoretical solutions, while transition to higher-fidelity patched-integrated models and differential corrections algorithms enable trajectories that satisfy the true dynamics and mission constraints. Filtering and ranking capabilities incorporated into MInX allow the user to prune the often-massive trade-space as the search script executes in order to maintain a finite set of solutions that best satisfy the design goals for a mission or concept. Promising solutions identified from the MInX broad searches are refined and optimized using the Evolutionary Mission Trajectory Generator (EMTG). Within EMTG, final constraints are implemented, and solutions are transitioned to the full-fidelity dynamical model. The EMTG dynamics model includes N-body gravity, central body harmonics, and spherical/cannonball solar radiation pressure (SRP) perturbations, and has been validated with high-fidelity tools such as the Multiple Interferometric Ranging Analysis using GPS Ensemble (MIRAGE) tool and the Systems Tool Kit (STK). EMTG currently supports trajectory optimization activities for Dragonfly, as well as the Europa Clipper Jupiter pump-down design. EMTG has been used previously to design and optimize the trajectories of the Discovery-class Lucy mission (now in Phase E), and the DAVINCI mission (now in Phase B). EMTG has additionally supported OSIRIS-REx, Janus, the Asteroid Robotic Redirect Mission (ARRM), the Double Asteroid Redirection Test (DART), an extended mission proposal for JAXA's Hayabusa 2, and numerous other Discovery and New Frontiers mission proposals. A tabulated summary of the tour flybys and perijove passages is provided in Exhibit B-11.

Exhibit B-11: Summary of science tour flybys and perijove passes.

Phase	Flyby Date	Flyby	Altitude (km)	V_∞ (km/s)	Period (days)	Perijove Date	r_p (RJ)	i (deg)	Perijove LST (hr:mn:sc)
Science Phase I	Aug 03, 2035	I1	301.7	18.9	-	Aug 02, 2035	5.42	46.1	17:43:49
	Dec 31, 2035	I2	301.6	18.7	71.5	Dec 31, 2035	5.34	47.8	16:37:32
	Mar 11, 2036	I3	300.3	18.9	44.6	Mar 11, 2036	5.33	49.1	16:08:23
	Apr 24, 2036	I4	649.2	18.9	33.7	Apr 24, 2036	5.34	49.9	15:50:24
	May 28, 2036	I5	300.5	19.0	24.9	May 27, 2036	5.35	50.5	15:38:41
	Jun 21, 2036	I6	301.9	19.0	19.1	Jun 21, 2036	5.34	51.0	15:32:04
	Jul 07, 2036	C1	411.7	9.4	16.7	Jul 09, 2036	4.20	50.2	15:37:21
	Jul 24, 2036	C2	822.2	9.4	16.7	Jul 26, 2036	3.57	46.4	15:28:50
	Aug 10, 2036	C3	126.6	9.4	16.7	Aug 12, 2036	2.89	40.5	15:24:37
	Aug 27, 2036	C4	24.4	9.4	16.7	Aug 28, 2036	2.33	32.8	15:17:48
Transition	Sep 12, 2036	C5	24.1	9.4	16.6	Sep 14, 2036	1.89	23.2	15:17:27
Science Phase II	Sep 29, 2036	C6	25.0	9.4	15.0	Oct 01, 2036	1.30	15.0	15:33:05
	-	-	-	-	-	Oct 16, 2036	1.30	14.9	15:15:51
	-	-	-	-	-	Oct 31, 2036	1.30	15.0	15:38:42
	-	-	-	-	-	Nov 15, 2036	1.02	15.0	15:32:05

Appendix C. Additional Science Payload Details

Additional details are captured here in tabular form for all COMPASS science payload instruments.

C.1 Thermal Plasma Detector (TPD)

Item	Value	Units
Type of instrument	Faraday cup	
Number of channels (baseline)	26 (per species)	
Size/dimensions (for each instrument)	30x22.9x29.2	cm
Instrument average science data rate^ without contingency	0.44 (survey)	kbps
	5.15 (burst)	kbps
Instrument average science data^ rate contingency	28	%
Instrument average science data^ rate with contingency	0.56 (survey)	kbps
	6.59 (burst)	kbps
Instrument field-of-view	45 (conical)	degrees
Pointing requirements (knowledge)	1	degrees
Pointing requirements (control)	n/a	degrees
Pointing requirements (stability)	n/a	deg/sec
Representative Heritage Instrument	Europa Clipper/PIMS (Grey et al., 2018)	

C.2 Suprathermal Plasma Detector (SPD)

Item	Value	Units
Type of instrument	Electrostatic analyzer with time-of-flight	
Number of channels (baseline)	16 (per species)	
Size/dimensions (for each instrument)	22.9x38.9x28.0	cm
Instrument average science data rate^ without contingency	1.21 (survey)	kbps
	14.07 (burst)	kbps
Instrument average science data^ rate contingency	28	%
Instrument average science data^ rate with contingency	1.55 (survey)	kbps
	18.01 (burst)	kbps
Instrument field-of-view	159´4 (FWHM)	degrees
Pointing requirements (knowledge)	1	degrees
Pointing requirements (control)	n/a	degrees
Pointing requirements (stability)	n/a	deg/sec
Representative Heritage Instrument	Cassini/CHEMS (Krimigis et al., 2004)	

C.3 Energetic Particle Detector (EPD)

Item	Value	Units
Type of instrument	Energy time-of-flight telescope	
Number of channels (baseline)	18 (per species)	
Size/dimensions (for each instrument)	23.0x16.9x17.7	cm
Instrument average science data rate^ without contingency	0.85 (survey)	kbps
	19.77 (burst)	kbps
Instrument average science data^ rate contingency	28	%
Instrument average science data^ rate with contingency	1.09 (survey)	kbps
	25.31 (burst)	kbps
Instrument field-of-view	160´12	degrees
Pointing requirements (knowledge)	1	degrees
Pointing requirements (control)	n/a	degrees
Pointing requirements (stability)	n/a	deg/sec
Representative Heritage Instrument	Juno/JEDI (Mauk et al., 2017)	

C.4 Relativistic Particle Detector (RPD)

Item	Value	Units
Type of instrument (baseline)	Solid-state telescope	
Number of channels	10 (per species)	
Size/dimensions (for each instrument)	23.5x29.6x24.7	cm
Instrument average science data rate^ without contingency	0.24 (survey)	kbps
	5.66 (burst)	kbps
Instrument average science data^ rate contingency	28	%
Instrument average science data^ rate with contingency	0.31 (survey)	kbps
	7.24 (burst)	kbps
Instrument field-of-view	32 (full angle)	degrees
Pointing requirements (knowledge)	1	degrees
Pointing requirements (control)	n/a	degrees
Pointing requirements (stability)	n/a	deg/sec
Representative Heritage Instrument	Van Allen Probes/REPT (Baker et al., 2012)	

C.5 Ultra-relativistic Particle Detector (UPD)

Item	Value	Units
Type of instrument	Solid-state telescope with Cherenkov radiator	
Number of channels (baseline)	14 (per species)	
Size/dimensions (for each instrument)	24.8x26.0x10.0	cm
Instrument average science data rate^ without contingency	0.17 (survey)	kbps
	3.40 (burst)	kbps
Instrument average science data^ rate contingency	28	%
Instrument average science data^ rate with contingency	0.22 (survey)	kbps
	4.35 (burst)	kbps
Instrument field-of-view	53.6 (conical)	degrees
Pointing requirements (knowledge)	1	degrees
Pointing requirements (control)	n/a	degrees
Pointing requirements (stability)	n/a	deg/sec
Representative Heritage Instrument	Van Allen Probes/RPS (Mazur et al., 2013)	

C.6 Flux Gate Magnetometer (FGM)

Item	Value	Units
Type of instrument	3D fluxgate magnetometer	
Number of channels (baseline)	25 (per axis)	
Size/dimensions (for each instrument)	14.0x7.6x13.7	cm
Instrument average science data rate^ without contingency	0.90 (survey)	kbps
	6.45 (burst)	kbps
Instrument average science data^ rate contingency	28	%
Instrument average science data^ rate with contingency	1.15 (survey)	kbps
	8.26 (burst)	kbps
Instrument field-of-view	n/a	degrees
Pointing requirements (knowledge)	0.005	degrees
Pointing requirements (control)	1	degrees
Pointing requirements (stability)	1	deg/sec
Representative Heritage Instrument	MESSENGER/MAG (Anderson et al., 2007)	

C.7 Search Coil Magnetometer (SCM)

Item	Value	Units
Type of instrument	3D search coil magnetometer	
Number of channels (baseline)	64 (per axis)	
Size/dimensions (for each instrument)	17.0x12.0x12.0	cm
Instrument average science data rate^ without contingency	0.27	kbps
	8.88	kbps
Instrument average science data^ rate contingency	28	%
Instrument average science data^ rate with contingency	0.35	kbps
	11.37	kbps
Instrument field-of-view	n/a	degrees
Pointing requirements (knowledge)	1	degrees
Pointing requirements (control)	1	degrees
Pointing requirements (stability)	1	deg/sec
Representative Heritage Instrument	Juno/Waves (Kurth et al., 2017)	

C.8 Electric Field Waves (EFW)

Item	Value	Units
Type of instrument	3D electric field antennae	
Number of channels (baseline)	111 (per axis)	
Size/dimensions (for each instrument)	44.4x43.0x18.5	cm (stowed)
	600 (´3)	cm (antennae)
Instrument average science data rate^ without contingency	0.57	kbps
	27.32	kbps
Instrument average science data^ rate contingency	28	%
Instrument average science data^ rate with contingency	0.73	kbps
	34.97	kbps
Instrument field-of-view	n/a	degrees
Pointing requirements (knowledge)	1	degrees
Pointing requirements (control)	1	degrees
Pointing requirements (stability)	1	deg/sec
Representative Heritage Instrument	STEREO/WAVES (Bougeret et al., 2008)	

C.9 X-ray Imager (XRI)

Item	Value	Units
Type of instrument	Solid-state X-ray imager	
Number of channels (baseline)	8	
Size/dimensions (for each instrument)	12.0x21.3x20.0	cm
Instrument average science data rate^ without contingency	1.07 (survey)	kbps
	64.0 (burst)	kbps
Instrument average science data^ rate contingency	28	%
Instrument average science data^ rate with contingency	1.37 (survey)	kbps
	81.92 (burst)	kbps
Instrument field-of-view	90	degrees
Pointing requirements (knowledge)	0.25	degrees
Pointing requirements (control)	2	degrees
Pointing requirements (stability)	0.25	deg/sec
Representative Heritage Instrument	AEPEX/AXIS (Marshall et al., 2020)	

C.10 Education and Public Outreach Camera (EPOC)

Item	Value	Units
Type of instrument	Color imager	
Number of channels (baseline)	16	
Size/dimensions (for each instrument)	16.6x9.9x13.0	cm
Instrument average science data rate^ without contingency	0.24 (survey)	kbps
	n/a (burst)	kbps
Instrument average science data^ rate contingency	28	%
Instrument average science data^ rate with contingency	0.31 (survey)	kbps
	n/a (burst)	kbps
Instrument field-of-view	58´5	degrees
Pointing requirements (knowledge)		degrees
Pointing requirements (control)		degrees
Pointing requirements (stability)		deg/sec
Representative Heritage Instrument	Juno/Junocam (Hansen et al., 2017)	

C.11 Instrument Degradation

The science payload will suffer different kinds of damage within the high radiation environment of Jupiter, which will affect the raw measurements in different ways. These effects can be mitigated through the use of detectors that are less degraded by radiation and/or in-flight recalibration of the instrument that compensates for the degradation.

In-flight recalibration often cannot be done after the fact but involves changing the flight software of the instrument before the next pass through the radiation belts. Mitigation therefore is not limited to hardware but also support of personnel during Phase E.

Solid state detectors exposed to ion radiation build up a dead layer on their most exposed surface (Knoll 2010). This layer does not respond to radiation and effectively makes particles appear to have less energy than in reality. Instruments that combine SSDs with independent time of flight (TOF) measurement (such as the nominal SPD and EPD instruments) can easily be recalibrated because the TOF is unaffected by the SSD (e.g., Lee-Payne et al., 2020). The remaining effect after recalibration is that the lowest measurable energy is rising during degradation. A similar rise in threshold results from the increase in leakage current as the detector degrades. Because the upper energy limit is unaffected in both cases (and the nominal Faraday cup TPD is immune to such degradation), that process can be mitigated by ensuring a large overlapping energy range between instruments. SSD-only instruments on the other hand (such as RPD and UPD) will need to rely on reducing the damage to detectors. Diamond detectors or avalanche photodiodes are much more reliable in high radiation environments (Ogasawara et al., 2016) and therefore may be better choices for COMPASS than the commonly used silicon detectors.

Ion radiation that penetrates SSD detectors also causes bulk damage that lowers the height and increases the width of the electronic pulses created during the detection of a particle (e.g. Knoll 2010). Such changes can be tracked by carrying an onboard radioactive calibration and a pulser that can insert artificial signals resembling particles into the detector. Both are common techniques that have been implemented in the past (e.g., McNutt et al., 2008; McComas et al., 2016).

MCP detectors lose efficiency the more particles they detect. MCPs therefore need to be strongly shielded to avoid unnecessarily counting penetrating particles. CEM detectors on the other hand show longer lifetimes in high radiation environments (e.g., Fedorov et al., 2020) and generally show a smaller response to penetrators, even when accounting for their typically smaller detection area. Therefore, MCPs may be replaced, wherever detection with high spatial resolution is not needed.

Accommodation of CEMs in already existing instruments is less straightforward due to their different form factor but are better suited for high radiation environments.

C.12 Signal to Noise Calculations

We calculate the ratio of counts due to the intentionally measured signal versus the counts due various noise sources. In order to do that, we selected Jupiter's L=2 as one the worst-case region, where energies and intensities of charged particles are highest, which is scientifically most interesting but also leads to strongest noise signals. Spectra in this region are not known with certainty, so we estimate their value based on the measurement constrained physical SALAMBO model for protons and electrons (Nénon et al., 2017, 2018). We then approximate instrument shielding through tungsten slabs with different thicknesses and use GEANT simulations to infer proton, electron, and gamma spectra behind that shielding. The respective spectra are shown in Exhibit C-1. Using aluminum slabs with the same column density trades less penetrating gamma rays vs. more penetrating electrons. A full shielding analysis may want to find the optimum between a layering of materials.

The signal count rate is simply calculated based on the ambient spectra and the documented geometry factor and efficiency of the respective instrument over the nominal energy interval of the chosen measurement.

The noise count rate can in principle be calculated equivalently. As geometry factor we assume that the detectors are very flat and are irradiated omnidirectionally, in which case the geometry factor

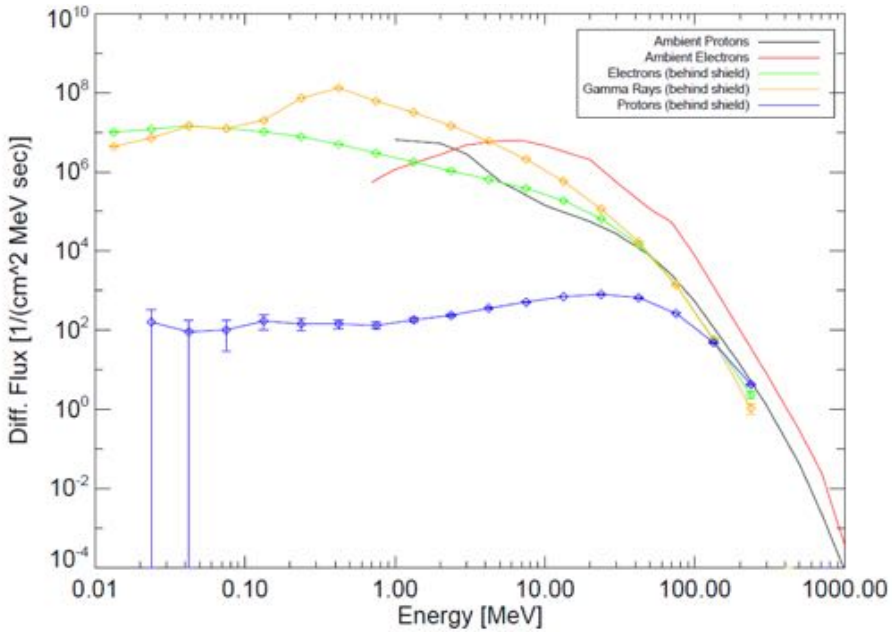

Exhibit C-1: Black and red: Worst case proton and electron energy spectra at Jupiter (found at L=2) based on the SALAMBO model (Nênon et al., 2017, 2018). Blue, green, orange: Proton, electron, and gamma spectra based behind 6.82mm W, the equivalent shielding of the RBSP/REPT instrument. It can be seen that shielding does not entirely block incoming radiation.

is detector area $* 2\pi$. Energy range and efficiency differ depending on the respective particle and detector:

Ions on SSD: We assume that the detector is 100% efficient to particles in the nominal energy range.

Ions on MCP: We assume that the detector is 100% efficient to any ion striking it.

Electrons on SSD: Electrons that penetrate the detector can deposit a very large range of energies that is unrelated to their incidence energy, see Exhibit C-2. To calculate the noise onto an electron measurement, we calculate such a distribution for the given detector thickness and determine the

efficiency for the energy range required for a valid measurement. To estimate the noise onto an ion measurement that is taken at the minimum ionizing energy of the detector, we assume that all SSD-penetrating electrons are counted.

Electrons on MCP: We use an energy dependent efficiency function (e.g., Andre et al., 2019) that is ~1 at ~1 keV and ~0.1 at ~1 MeV. We use the nominal energy range.

Gammas on SSD: We use an energy dependent efficiency function established from GEANT simulations of any non-zero ionizing losses that gammas have in a 300-μm SSD. The efficiency is ~1 at ~1 keV and ~0.01 at ~1 MeV. We use the nominal energy range.

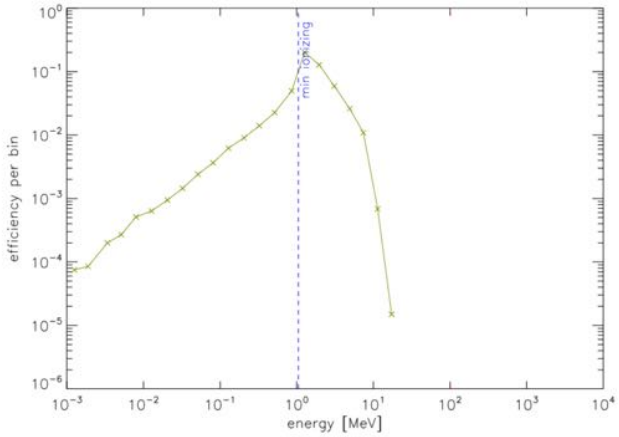

Exhibit C-2: Efficiency for detecting electrons of a certain energy with a 3mm thick SSD of 2cm diameter (equivalent to the first two REPT SSDs). This distribution is identical for all >1MeV input energies. The peak of the distribution is roughly at the minimum ionizing energy that scales linearly with the detector thickness.

Gammas on MCP: We use an energy dependent efficiency function (based on an estimate internally used within the JUICE mission) that uses the electron MCP efficiency, reduced by a factor of four (4). We use the nominal energy range.

The rate of accidental coincidences for SSD-only measurements is rates of single SSD to the power of coincidence number times the SSD pulse rise time to the power of coincidence number -1. The rate of accidental coincidences for SSDs combined with a time of flight (TOF) from two MCP measurements is MCP rates to the power of two (2) × TOF window × SSD rate × SSD pulse rise time. Anti-coincidence measurements add another factor of exp(- detector rate × pulse rise time), which only lowers the accidental rate when the detectors saturate.

We calculated SNR for ions measured at the minimum ionizing energy of SPD and EPD, which is where we expect most noise due to the contribution of SSD penetrators. Results for EPD were shown in Exhibit 3-3 and are similar for SPD due to the similar measurement technique.

For RPD measuring electrons we found that neither a two (2) nor a nine (9)-coincidence measurement reaches the desired SNR (results for the nine (9) coincidences were shown in Exhibit 3-3). Reducing the detector size significantly improves SNR for nine (9) coincidences, while two (2) coincidences still remain insufficient.

UPD with its thirteen (13) well-defined coincidences has even with the current design no SNR issue for measuring protons.

C.13 Instrument Development Plans to Enhance the Science Return from COMPASS

The Ultra-relativistic Particle Detector (UPD) of COMPASS has the challenging task to measure the energy, direction, time, and composition of the most energetic particles that can be trapped at Jupiter, covering electrons in the range of 10 MeV to >50-70 MeV, protons and ions (in particular oxygen and sulfur ions) from 100 MeV/nuc to few GeV/nuc. Measurements without energy resolution and physical models suggest the existence of such populations, but their distribution has never been accurately observed. New discoveries about phenomena in this energy range await us that will provide

clues to acceleration processes that have never been studied in-situ. Below we describe maturation plans for both RPS and a relativly new instrument concept Pix.PAN.

RPS

The Ultra-relativistic Particle Detector (UPD) will have heritage from the Relativistic Proton Spectrometer (RPS) aboard the Van Allen Probes. As its name implies, RPS was optimized to measure the protons in Earth's inner radiation belt, but evidence was found for an unexpected population of ultrarelativistic (>30 MeV) electrons within that belt as well. Based on measurements with and modeling of RPS, it would be worthwhile to evolve the Cherenkov portion of the UPD sensor head to take advantage of the different ways that electrons and ions produce Cherenkov light in a transparent material and thereby to better distinguish these species in observations at Jupiter. In particular, RPS used a single-pixel photocathode to count all photons that exited the Cherenkov radiator, but for UPD, investigating the use of position sensitivity to separate portions of the Cherenkov light that are more and less likely to have been produced by electrons rather than ions. RPS used a microchannel plate photomultiplier, whose photocathode could at best be subdivided into four regions and which is no longer being manufactured. For UPD, silicon photomultipliers (SiPMs), which can be divided into many pixels and have numerous other advantages such as compactness, ruggedness, and low power demand would be a natural future technology pursuit. SiPMs have been of interest for several years in the fields of medical imaging, high-energy physics, and nuclear security, and have undergone radiation testing relevant to these environments (e.g., Wonders et al., 2018). However, development of UPD would benefit from further characterization of these detectors that is specific to their use for the detection of Cherenkov light in space. This would include a focus on the radiation-dose dependence of parameters that are particularly relevant to Cherenkov light detection (gain shifts, dark current, hot pixels, quantum efficiency, etc.) and on testing in radiation fields that replicate the species and intensities to be encountered in the unique environment of Jupiter's magnetosphere.

Pix.PAN

A promising, but lower TRL instrument, is Pix.PAN, which is based on heritage from PAN (Wu et al., 2019). Below are details describing the Pix.PAN instrument, its expected performance, and a maturation plan for the next decade.

Pix.PAN concept. Magnetic spectrometr (MS) designs are a proven high precision detection technology for energetic particles, and has been successfully used in large space missions (e.g., Picozza et al., 2007; Lübelsmeyer et al., 2011). In a MS, the momentum resolution, thus the energy resolution, has two contributions: one, related to the magnetic field (strength and length) and the tracker precision, increases with momentum; the other, due to the multiple Coulomb scattering (MCS), which decreases with momentum. With appropriate instrument design, it is possible to mitigate these two effects to achieve a good energy resolution over the desired energy range.

A magnetic spectrometer measures the rigidity (momentum over charge p/Z) of a charged particle through its bending in a magnetic field, which then can be used to derive the momentum and energy if the charge (Z) of the particle, can be independently identified. The baseline layout of Pix.PAN, adopted from the Mini.PAN design—currently under development, is shown in Exhibit C-3. It is a cylindrical magnetic spectrometer with two Halbach magnet sectors of 5 cm in diameter, each providing a dipole field of ~0.4 Tesla, with 3 tracking stations to measure the bending of the particle trajectory. To satisfy the performance specifications of UPD, in particular the extreme high hit rates (up to ~60 MHz/cm2) and the hash operating environment, the tracking stations will be implemented with hybrid pixel detector read out by the latest version of the widely used, both on ground-based experiment and in space, Midepix/Timepix series of readout ASICs (Silari et al., 2020), the Timpix4 (Llopart et al., 2022). Not only can the Timepix4-based pixel detectors provide excellent tracking

performance under high rate and hostile operating conditions, it can also provide good timing and particle charge measurements for particle identification.

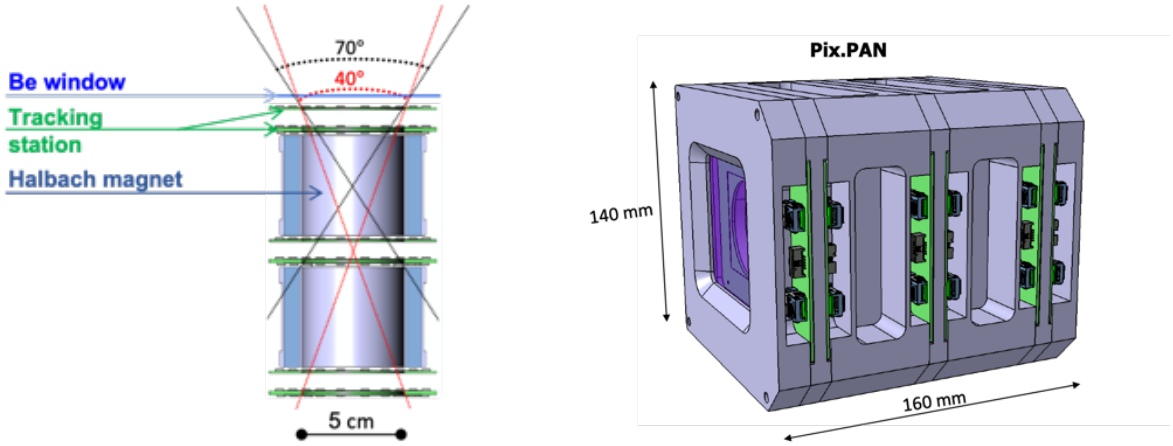

Exhibit C-3: A sketch of the spectrometer layout of Pix.PAN key components, showing the 2 magnet sectors and 3 tracking stations (left). Preliminary design of the mechanical structure of the Pix.PAN spectrometer, excluding shielding and radiator material (right).

Magnets. In the framework of Mini.PAN, the Halbach magnet sectors assembled with NdFeB permanent magnet pieces have been design, produced, measured and assembled (Exhibit C-4). The design requirements are mostly satisfied. The weight of each magnet is 0.8 kg, for a total of about 1.6 kg.

Exhibit C-4: The Mini.PAN magnets: Design sketch (left); Magnet prototype (middle left); Single magnet under magnetic field wire-scan at CERN (middle right); 2-magnet assembly under magnetic field measurement with Hall probe at CERN (right).

Tracker. The bending of a charge particle due to the magnetic field is measurand by a tracker: a series of position sensitive detectors placed along the track of the particle. The tracker of the Pix.PAN instrument consists of three tracking stations, each composed two tracking layers. Silicon strip or pixel detectors have been widely used in nuclear and particle physics experiments, as well as in space (e.g. PAMELA and AMS). Due to the high-rate environment of Jupiter's radiation belts, silicon Hybrid Active Pixel Sensors (HAPS) based on the Timepix4 readout ASIC will be used for Pix.PAN.

Timepix is a series of hybrid pixel detector readout ASIC developed by the Medipix collaboration led by CERN since 1999, and has been widely used in particle physics, nuclear physics, medical physics, and in space. Timepix4 is the 4th generation of the ASIC produced and validated in 2021. The Pix.PAN tracking layer consists of silicon pixel detector readout by 2x2 Timepix4. The Timepix4 chip measures 29.96×24.7 mm^2, therefore the quad assembly can readout a silicon pixel detector up to 60×50 mm^2 in size, sufficient to cover the sensitive area of the spectrometer, as shown in the left panel of Exhibit C-5. Note that Timepix3 quad assembly has been successfully produced for Mini.PAN, as shown in the right panel of Exhibit C-5.

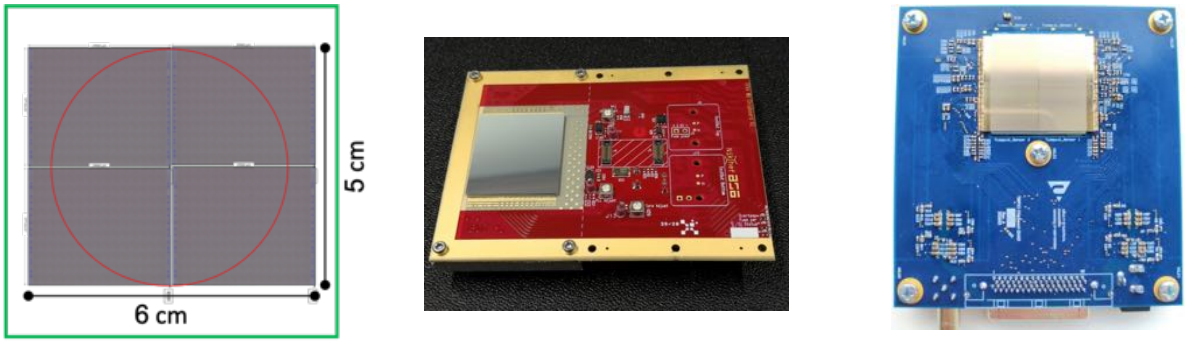

Exhibit C-5. Area of the Timepix4 quad assembly of a Pix.PAN tracking layer (left); Photo of a single Timepix4 assembly with a 300 μm silicon pixel detector (middle). Photo of the Mini.PAN Timepix3 quad assembly prototype (right).

Timepix4 is a large area pixel detector readout chip with high-rate capability, up to a hit rate of 358 Mz/cm^2. Each ASIC has 512×448 readout cells with 55 μm bump bonding pitch. In data-driven mode it has been demonstrated to operate with a threshold of 800 electrons, which is about 1/14 of electron-hole pairs produced by a minimum ionizing particle (MIP) in 150 μm of silicon. The energy resolution is ~1 keV, corresponding to about 1.7% for the most probable energy loss by a minimum ionizing particle in 150 μm of silicon. One important feature of the ASIC is that it can provide a timestamp within 195 picosecond bins, allowing to use the tracker as a Time-Of-Flight (TOF) detector as well. The tracking layers will also measure the charge number (Z) of the particles using the dE/dx method thanks to the full analog readout capability of Timepix4. Therefore, due to the powerful functionalities of Timepix4 the Pix.PAN instrument will have only one type of sensor, which makes it simple and robust to operate. There are also two important features: no trigger device is needed since Timepix4 uses a data-driven readout scheme, and the readout is purely digital since the ADC and TDC are fully integrated in Timepix4.

Silicon hybrid active pixel sensors have been operated successfully in high radiation environment such as in collider experiments at the LHC hadron collider at CERN, which is hasher than the 100 krad expected for Pix.PAN. Radiation induced single event upset effects can be mitigated by periodically refreshing the registers of the ASIC. The full configuration matrix of Timepix4 can be updated within 100 ms.

Silicon pixel detector geometry and connection scheme to Timepix4. The position resolution of a silicon pixel detector is mainly defined by its size, also called pitch. In the case of a magnetic spectrometer the position resolution requirement is more stringent in the bending plane (perpendicular to the field lines) than in the non-pending plane since the energy resolution is directly linked to the precision of measuring the bending radius. To reach the 20-30% energy resolution of ultra-relativistic particles required for UPD, a position resolution of 3-5 μm is needed, which can be provided with a pixel pitch of ~25-50 μm, but on the bending direction only. The pixel pitch on the

non-bending direction can be larger, up to the extent that the increased total capacitance of the "long pixel" will not degrade substantially the noise performance of the detector. The current estimate is that Timepix4 can still preform very well with a long pixel of 27.5 μm ×880 μm, which can substantially reduce the power consumption of the system.

To connect this non-standard pixel detector to 55 μm ×55 μm square readout cells of Timepix4 a specific "pitch adapter" needs to be integrated into the pixel detector that may necessitates a "double metal" structure, in particular when the pixel pitch is smaller than the Timepix4 readout pitch. Design discussions are underway with pixel detector manufacturers and preliminary solutions have been found. In one scenario the pixel sensor will consist of 2048 x 57 pixels of 27.5 μm × 880 μm in size, making a homogenous detection area of 56.32 mm x 50.16 mm, sufficient to cover the full magnet volume. The outer dimension of the sensor is 58.48 mm x 52.28 mm, as shown in the left panel of Exhibit C-6 The 116,736 pixels will be readout by 4 Timepix4 ASIC, but only 1 in 8 Timepix4 readout cells will be used, thanks to a double metal connection scheme, as shown in the right panel of Exhibit C-6.

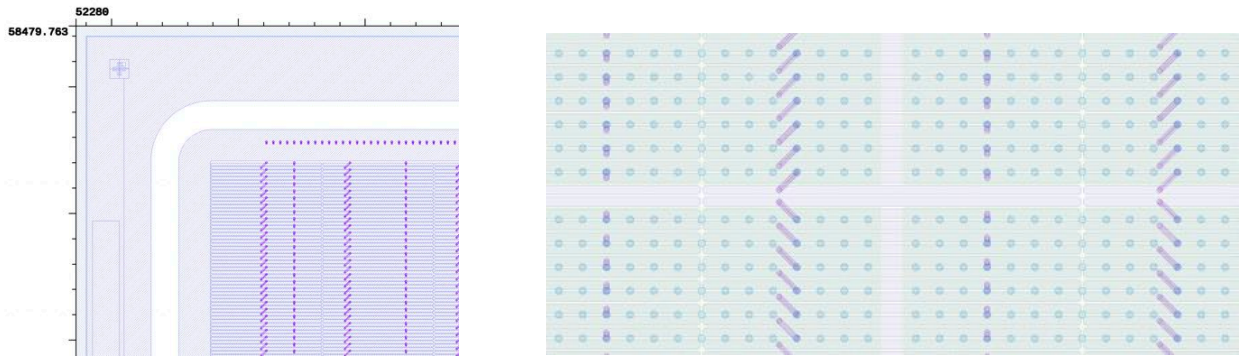

Exhibit C-6: Corner of the Pix.PAN pixel sensor showing the outer dimensions, the guard rings, and the pixels (left); The double metal connection scheme between the pixels (magenta squares) and the bonding pads for Timepix4 (cyan circle) at the center of the sensor where 4 Timepix4 chips are next each other. Only 1 out of 8 bonding pads are connected to the pixels (right).

In this design there is no dead area on the sensor between the four Timepix4 chips on a quad assembly. However, this scheme requires to use the high performance TSV (through-silicon via) interconnect technology to connect the ASICs to the carrier PCB, which will have cut-out areas under the ASICs to minimize dead material on the passage of the particles. Given the complexity of the quad assembly the design of the pixel detector and carrier PCB will need to be validated with prototypes and space qualified. The key feature of this design is that the analog power consumption of the ASICs will be reduced by a factor of 8 without compromising the performance of the spectrometer.

Development in the next decade: there are two key technologies that are needed to be addressed:

- Silicon pixel detector geometry and connection scheme to Timepix4 optimized for the Pix.PAN application for COMPASS
- Real time data processing with Machine Learning algorithm implemented on AI capable hardware

Silicon pixel detector geometry and connection scheme to Timepix4. As discussed above a preliminary sensor design with 27.5 μm×880 μm pixels based on double metal connection scheme has been defined, which allows to reduce substantially the power consumption of the instrument. This sensor geometry needs to be first validated with the Timpix4 simulation in terms of

noise performance. Then sensor prototypes need to be produced to evaluate the energy resolution achievable with various sensor thickness, which affects both the signal to noise ratio, and the multiple scattering effect. Another key development is the assembly of the pixel sensor with four Timepix4 ASICs to build a "quad" pixel layer. To minimize dead space the advance interconnect TSV technology, will be used to connect the ASICs to a carrier PCB, which will have cut out areas under the ASICs to minimize dead material on the passage of the particles. Note that TSV connectivity has already been foreseen in the Timepix4 design and its TSV processing and assembly procedures are currently being developed by several institutions, including the Fraunhofer Institute for Reliability and Microintegration (IZM) in Germany. Given its complexity the quad assembly will need to be validated with prototypes and space qualified, for both mechanical and thermal aspects.

Real time data processing. For an implementation on a Jupiter mission the real-time on-board processing of the Pix.PAN raw data is mandatory. As explained previously the data processing of a magnetic spectrometer, including the track reconstruction and particle identification, are well understood, but typically implemented as software algorithms running on computer clusters where power consumption is not the main concern. For the COMPASS application where the required data output is well-defined for the science objectives, the data processing can be optimized in terms of precision vs power consumption, using more advance approaches such as Machine Learning based algorithms, which are particularly suitable for the multivariate problems of tracking and particle identification, and can profit from the emerging AI capable electronics hardware, such as the Xilinx Kintex Ultrascale XQRKU060 Space-Grade FPGA.

Appendix D. References

Allen, R. C., Paranicas, C. P., Bagenal, F., Vines, S. K., Hamilton, D. C., Allegrini, F., ... & Wilson, R. J. (2019). Energetic oxygen and sulfur charge states in the outer Jovian magnetosphere: Insights from the Cassini Jupiter flyby. *Geophysical Research Letters*, *46*(21), 11709-11717.

Anderson, B. J., Acuña, M. H., Lohr, D. A., Scheifele, J., Raval, A., Korth, H., & Slavin, J. A. (2007). The Magnetometer instrument on MESSENGER. In *The MESSENGER mission to Mercury* (pp. 417-450). Springer, New York, NY.

Andriopoulou, M., Roussos, E., Krupp, N., Paranicas, C., Thomsen, M., Krimigis, S., ... & Glassmeier, K. H. (2014). Spatial and temporal dependence of the convective electric field in Saturn's inner magnetosphere. *Icarus*, *229*, 57-70.

Artemyev, A. V., et al. "Juno observations of heavy ion energization during transient dipolarizations in Jupiter magnetotail." *Journal of Geophysical Research: Space Physics* 125.5 (2020): e2020JA027933.

Aryan, H., Bortnik, J., Meredith, N. P., Horne, R. B., Sibeck, D. G., & Balikhin, M. A. (2021). Multi-parameter chorus and plasmaspheric hiss wave models. *Journal of Geophysical Research: Space Physics*, *126*(1), e2020JA028403.

Baker, D. N., et al. "Gradual diffusion and punctuated phase space density enhancements of highly relativistic electrons: Van Allen Probes observations." *Geophysical Research Letters* 41.5 (2014): 1351-1358.

Baker, D. N., et al. "Highly relativistic electrons in the Earth'; s outer magnetosphere: 1. Lifetimes and temporal history 1979–1984." *Journal of Geophysical Research: Space Physics*91.A4 (1986): 4265-4276.

Baker, D. N., Kanekal, S. G., Hoxie, V. C., Batiste, S., Bolton, M., Li, X., ... & Friedel, R. (2012). The Relativistic Electron-Proton Telescope (REPT) instrument on board the Radiation Belt Storm Probes (RBSP) spacecraft: Characterization of Earth's radiation belt high-energy particle populations. In *The van allen probes mission* (pp. 337-381). Springer, Boston, MA.

Bhardwaj, Anil, et al. "X-rays from solar system objects." *Planetary and Space Science* 55.9 (2007): 1135-1189.

Blake, J. B., and Michael Schulz. "The satellites of Jupiter as a source of very energetic magnetospheric particles." *Icarus*44.2 (1980): 367-372.

Blake, J. B., H. H. Hilton, and S. H. Margolis. "On the injection of cosmic ray secondaries into the inner Saturnian magnetosphere: 1. Protons from the CRAND process." *Journal of Geophysical Research: Space Physics* 88.A2 (1983): 803-807.

Bolton, S. J., et al. "Ultra-relativistic electrons in Jupiter's radiation belts." *Nature* 415.6875 (2002): 987-991.

Bolton, Scott J., et al. "Jupiter's inner radiation belts." *Jupiter: The Planet, Satellites, and Magnetosphere* 1 (2004): 671-688.

Bougeret, J. L., Goetz, K., Kaiser, M. L., Bale, S. D., Kellogg, P. J., Maksimovic, M., ... & Zouganelis, I. (2008). S/WAVES: The radio and plasma wave investigation on the STEREO mission. *Space Science Reviews*, *136*(1), 487-528.

Boyd, Alexander J., et al. "What causes radiation belt enhancements: A survey of the Van Allen Probes Era." *Geophysical Research Letters* 45.11 (2018): 5253-5259.

Branduardi-Raymont, G., et al. "X-rays from Saturn: a study with XMM-Newton and Chandra over the years 2002–05." *Astronomy & Astrophysics* 510 (2010): A73.

Clark, G., et al. "Charge states of energetic oxygen and sulfur ions in Jupiter's magnetosphere." *Journal of Geophysical Research: Space Physics* 121.3 (2016): 2264-2273.

Clark, G., et al. "Energetic particle signatures of magnetic field-aligned potentials over Jupiter's polar regions." *Geophysical Research Letters* 44.17 (2017): 8703-8711.

Clark, G., et al. "Evolution of electron pitch angle distributions across Saturn's middle magnetospheric region from MIMI/LEMMS." *Planetary and Space Science* 104 (2014): 18-28.

Clark, George, et al. "Heavy ion charge states in Jupiter's polar magnetosphere inferred from auroral megavolt electric potentials." *Journal of Geophysical Research: Space Physics*125.9 (2020): e2020JA028052.

Clark, G., Mauk, B. H., Kollmann, P., Szalay, J. R., Sulaiman, A. H., Gershman, D. J., ... & Westlake, J. (2020). Energetic proton acceleration associated with Io's footprint tail. *Geophysical Research Letters*, *47*(24), e2020GL090839.

Cohen, C. M. S., Stone, E. C., & Selesnick, R. S. (2001). Energetic ion observations in the middle Jovian magnetosphere. *Journal of Geophysical Research: Space Physics*, *106*(A12), 29871-29881.

Cohen, Ian J., et al. "Investigating the Link Between Outer Radiation Belt Losses and Energetic Electron Escape at the Magnetopause: A Case Study Using Multi-Mission Observations and Simulations." *Journal of Geophysical Research: Space Physics* 126.6 (2021): e2021JA029261.

Connerney, J. E. P., Kotsiaros, S., Oliversen, R. J., Espley, J. R., Joergensen, J. L., Joergensen, P. S., ... & Levin, S. M. (2018). A new model of Jupiter's magnetic field from Juno's first nine orbits. *Geophysical Research Letters*, *45*(6), 2590-2596.

Connerney, J. E. P., Timmins, S., Oliversen, R. J., Espley, J. R., Joergensen, J. L., Kotsiaros, S., ... & Levin, S. M. (2022). A new model of Jupiter's magnetic field at the completion of Juno's Prime Mission. *Journal of Geophysical Research: Planets*, *127*(2), e2021JE007055.

Cooper, J. F., and J. A. Simpson. "Sources of high-energy protons in Saturn's magnetosphere." *Journal of Geophysical Research: Space Physics* 85.A11 (1980): 5793-5802.

Cooper, John F. "Nuclear cascades in Saturn's rings: Cosmic ray albedo neutron decay and origins of trapped protons in the inner magnetosphere." *Journal of Geophysical Research: Space Physics* 88.A5 (1983): 3945-3954.

de Pater, Imke, and David E. Dunn. "VLA observations of Jupiter's synchrotron radiation at 15 and 22 GHz." *Icarus*163.2 (2003): 449-455.

Delamere, P. A., and F. Bagenal. "Solar wind interaction with Jupiter's magnetosphere." *Journal of Geophysical Research: Space Physics* 115.A10 (2010).

Doyle, Alexandra E., Steven J. Desch, and Edward D. Young. "Icy exomoons evidenced by spallogenic nuclides in polluted white dwarfs." *The Astrophysical Journal Letters* 907.2 (2021): L35.

Dunn, W. R., et al. "The independent pulsations of Jupiter's northern and southern X-ray auroras." *Nature Astronomy* 1.11 (2017): 758-764.

Ebert, R. W., Allegrini, F., Bagenal, F., Bolton, S. J., Connerney, J. E., Clark, G., ... & Wilson, R. J. (2017). Accelerated flows at Jupiter's magnetopause: Evidence for magnetic reconnection along the dawn flank. *Geophysical Research Letters*, *44*(10), 4401-4409.

Elsner, Ronald F., et al. "Discovery of soft X-ray emission from Io, Europa, and the Io plasma torus." *The Astrophysical Journal* 572.2 (2002): 1077.

Ezoe, Yuichiro, et al. "Discovery of diffuse hard X-ray emission around Jupiter with Suzaku." *The Astrophysical Journal Letters* 709.2 (2010): L178.

Fedorov, A., Romeo, J. R., Baruah, R., Grigoriev, A., & André, N. (2019, July). Lifetime of channel electron multiplier detectors dedicated to plasma instruments for Solar Orbiter and JUICE space missions. In *International Conference on Space Optics—ICSO 2018* (Vol. 11180, pp. 2314-2320). SPIE.

Gladstone, G. R., et al. "A pulsating auroral X-ray hot spot on Jupiter." *Nature* 415.6875 (2002): 1000-1003.

Grey, M., Westlake, J., Liang, S., Hohlfeld, E., Crew, A., & McNutt, R. (2018, March). Europa PIMS prototype faraday cup development. In *2018 IEEE Aerospace Conference* (pp. 1-15). IEEE.

Hamilton, D. C., G. Gloeckler, S. M. Krimigis, and L. J. Lanzerotti (1981), Composition of nonthermal ions in the Jovian magnetosphere, *J. Geophys. Res.*, **86**, 8301–8318, doi:10.1029/JA086iA10p08301.

Hansen, C. J., Caplinger, M. A., Ingersoll, A., Ravine, M. A., Jensen, E., Bolton, S., & Orton, G. (2017). Junocam: Juno's outreach camera. *Space Science Reviews*, *213*(1), 475-506.

Hao, Y. X., Sun, Y. X., Roussos, E., Liu, Y., Kollmann, P., Yuan, C. J., ... & Zong, Q. G. (2020). The formation of saturn's and jupiter's electron radiation belts by magnetospheric electric fields. *The Astrophysical Journal Letters*, *905*(1), L10.Hill, M. E., et al. "The Mushroom: A half-sky energetic ion and electron detector." *Journal of Geophysical Research: Space Physics* 122.2 (2017): 1513-1530.

Horne, Richard B., and Richard M. Thorne. "Potential waves for relativistic electron scattering and stochastic acceleration during magnetic storms." *Geophysical Research Letters* 25.15 (1998): 3011-3014.

Horne, Richard B., et al. "Gyro-resonant electron acceleration at Jupiter." *Nature Physics* 4.4 (2008): 301-304.

Horne, Richard B., et al. "Timescale for radiation belt electron acceleration by whistler mode chorus waves." *Journal of Geophysical Research: Space Physics* 110.A3 (2005).

Kim, T. K., Ebert, R. W., Valek, P. W., Allegrini, F., McComas, D. J., Bagenal, F., ... & Nicolaou, G. (2020). Method to derive ion properties from Juno JADE including abundance estimates for O+ and S2+. *Journal of Geophysical Research: Space Physics*, *125*(2), e2018JA026169.

Knoll, G. F. (2010). *Radiation detection and measurement*. John Wiley & Sons.

Kollmann, P., Roussos, E., Paranicas, C., Krupp, N., & Haggerty, D. K. (2013). Processes forming and sustaining Saturn's proton radiation belts. *Icarus*, *222*(1), 323-341.

Kollmann, P., et al. "Electron acceleration to MeV energies at Jupiter and Saturn." *Journal of Geophysical Research: Space Physics* 123.11 (2018): 9110-9129.

Kollmann, Peter, et al. "Spectra of Saturn's proton belts revealed." *Icarus* 376 (2022): 114795.

Krimigis, S. M., Mitchell, D. G., Hamilton, D. C., Livi, S., Dandouras, J., Jaskulek, S., ... & Williams, D. J. (2004). Magnetosphere imaging instrument (MIMI) on the Cassini mission to Saturn/Titan. *The cassini-huygens mission*, 233-329.

Kurth, W. S., Hospodarsky, G. B., Kirchner, D. L., Mokrzycki, B. T., Averkamp, T. F., Robison, W. T., ... & Zarka, P. (2017). The Juno waves investigation. *Space Science Reviews*, *213*(1), 347-392.

Lee-Payne, Z., Kollmann, P., Grande, M., & Knight, T. (2020). Correction of Galileo energetic particle detector, composition measurement system high rate data: Semiconductor dead layer correction. *Space Science Reviews*, *216*(1), 1-14.

Lejosne, Solène, and Peter Kollmann. "Radiation belt radial diffusion at Earth and beyond." *Space Science Reviews* 216.1 (2020): 1-78.

Li, W., Ma, Q., Thorne, R. M., Bortnik, J., Zhang, X. J., Li, J., ... & Goldstein, J. (2016). Radiation belt electron acceleration during the 17 March 2015 geomagnetic storm: Observations and simulations. *Journal of Geophysical Research: Space Physics*, *121*(6), 5520-5536.

Li, W., & Hudson, M. K. (2019). Earth's Van Allen radiation belts: From discovery to the Van Allen Probes era. *Journal of Geophysical Research: Space Physics*, *124*(11), 8319-8351.

Li, Xinlin, et al. "Measurement of electrons from albedo neutron decay and neutron density in near-Earth space." *Nature* 552.7685 (2017): 382-385.

Ma, Q., et al. "Quantitative evaluation of radial diffusion and local acceleration processes during GEM challenge events." *Journal of Geophysical Research: Space Physics* 123.3 (2018): 1938-1952.

Mazur, J., Friesen, L., Lin, A., Mabry, D., Katz, N., Dotan, Y., ... & McNab, M. (2012). The relativistic proton spectrometer (RPS) for the radiation belt storm probes mission. In *The Van Allen Probes Mission* (pp. 221-261). Springer, Boston, MA.

Mogro-Campero, A., & Fillius, W. (1976). The absorption of trapped particles by the inner satellites of Jupiter and the radial diffusion coefficient of particle transport. *Journal of Geophysical Research*, *81*(7), 1289-1295.

Marshall, Robert A., and Chris M. Cully. "Atmospheric effects and signatures of high-energy electron precipitation." *The dynamic loss of Earth's radiation belts*. Elsevier, 2020. 199-255.

Masters, Adam, et al. "Magnetic reconnection near the planet as a possible driver of Jupiter's mysterious polar auroras." *Journal of Geophysical Research: Space Physics* 126.8 (2021): e2021JA029544.

Mauk, B. H., and N. J. Fox. "Electron radiation belts of the solar system." *Journal of Geophysical Research: Space Physics* 115.A12 (2010).

Mauk, B. H., et al. "Energetic ion characteristics and neutral gas interactions in Jupiter's magnetosphere." *Journal of Geophysical Research: Space Physics* 109.A9 (2004).

Mauk, B. H., et al. "The Jupiter energetic particle detector instrument (JEDI) investigation for the Juno mission." *Space Science Reviews* 213.1 (2017): 289-346.

Mauk, B. H., et al. "Transient aurora on Jupiter from injections of magnetospheric electrons." *Nature* 415.6875 (2002): 1003-1005.

McKibben, R. B., Simpson, J. A., & Zhang, M. (1993). Impulsive bursts of relativistic electrons discovered during Ulysses' traversal of Jupiter's dusk-side magnetosphere. *Planetary and Space Science*, *41*(11-12), 1041-1058.

Menietti, J. D., et al. "Low-latitude whistler-mode and higher-latitude Z-mode emission at Jupiter observed by Juno." *Journal of Geophysical Research: Space Physics* 126.2 (2021): e2020JA028742.

Meredith, N. P., Horne, R. B., Shen, X. C., Li, W., & Bortnik, J. (2020). Global model of whistler mode chorus in the near-equatorial region ($|\lambda m| < 18$). *Geophysical Research Letters*, *47*(11), e2020GL087311.

Millan, R. M., and D. N. Baker. "Acceleration of particles to high energies in Earth's radiation belts." *Space Science Reviews* 173.1 (2012): 103-131.

Millan, Robyn Margaret, et al. "X-ray observations of MeV electron precipitation with a balloon-borne germanium spectrometer." *Geophysical research letters* 29.24 (2002): 47-1.

McComas, D. J., Alexander, N., Angold, N., Bale, S., Beebe, C., Birdwell, B., ... & Wilson, P. (2016). Integrated Science Investigation of the Sun (ISIS): Design of the energetic particle investigation. *Space Science Reviews*, *204*(1), 187-256.

McComas, D. J., Christian, E. R., Schwadron, N. A., Fox, N., Westlake, J., Allegrini, F., ... & Zirnstein, E. J. (2018). Interstellar mapping and acceleration probe (IMAP): A new NASA mission. *Space science reviews*, *214*(8), 1-54.

McNutt, R. L., Livi, S. A., Gurnee, R. S., Hill, M. E., Cooper, K. A., Andrews, G. B., ... & Vandegriff, J. D. (2008). The Pluto energetic particle spectrometer science investigation (PEPSSI) on the New Horizons mission. *Space science reviews*, *140*(1), 315-385.

Nénon, Q., A. Sicard, and S. Bourdarie. "A new physical model of the electron radiation belts of Jupiter inside Europa's orbit." *Journal of Geophysical Research: Space Physics* 122.5 (2017): 5148-5167.

Nenon, Q., Clark, G., Jun, I., Kollmann, P., Liuzzo, L., Mauk, B., … Woodfield, E. E. (2021). Open science questions and missing measurements in the radiation belts of Jupiter. *Bulletin of the AAS*, *53*(4). https://doi.org/10.3847/25c2cfeb.fb50005f

Nénon, Q., et al. "A physical model of the proton radiation belts of Jupiter inside Europa's orbit." *Journal of Geophysical Research: Space Physics* 123.5 (2018): 3512-3532.

Nordheim, T. A., K. P. Hand, and C. Paranicas. "Preservation of potential biosignatures in the shallow subsurface of Europa." *Nature Astronomy* 2.8 (2018): 673-679.

Nulsen, S., Kraft, R., Germain, G., Dunn, W., Tremblay, G., Beegle, L., ... & Vance, S. (2020). X-ray emission from Jupiter's Galilean moons: A tool for determining their surface composition and particle environment. *The Astrophysical Journal*, *895*(2), 79.

Numazawa, Masaki, et al. "Suzaku observations of Jovian diffuse hard X-ray emission." *Publications of the Astronomical Society of Japan* 73.4 (2021): 894-911.

Paranicas, C., et al. "Energetic charged particle weathering of Saturn's inner satellites." *Planetary and Space Science* 61.1 (2012): 60-65.

Paranicas, C., et al. "Intervals of intense energetic electron beams over Jupiter's poles." *Journal of Geophysical Research: Space Physics* 123.3 (2018): 1989-1999.

Reeves, G. D., et al. "Electron acceleration in the heart of the Van Allen radiation belts." *Science* 341.6149 (2013): 991-994.

Roth, Lorenz, et al. "Transient water vapor at Europa's south pole." *science* 343.6167 (2014): 171-174.

Roussos, E., Kollmann, P., Krupp, N., Paranicas, C., Krimigis, S. M., Mitchell, D. G., ... & Holmberg, M. K. (2012). Energetic electron observations of Rhea's magnetospheric interaction. *Icarus*, *221*(1), 116-134.

Roussos, E., et al. "Quasi-periodic injections of relativistic electrons in Saturn's outer magnetosphere." *Icarus* 263 (2016): 101-116.

Roussos, Elias, and Peter Kollmann. "The radiation belts of Jupiter and Saturn." *Magnetospheres in the Solar System*(2021): 499-514.

Roussos, Elias, et al. "A source of very energetic oxygen located in Jupiter's inner radiation belts." *Science advances*8.2 (2022): eabm4234.

Roussos, Elias, et al. "The in-situ exploration of Jupiter's radiation belts." *Experimental Astronomy* (2021): 1-45.

Santos-Costa, D., et al. "Synchrotron emission images from three-dimensional modeling of the Jovian electron radiation belts." *Advances in Space Research* 28.6 (2001): 915-918.

Santos-Costa, Daniel, and Scott J. Bolton. "Discussing the processes constraining the Jovian synchrotron radio emission's features." *Planetary and Space Science* 56.3-4 (2008): 326-345.

Saur, J. (2021). Turbulence in the Magnetospheres of the Outer Planets. *Frontiers in Astronomy and Space Sciences*, 56.

Selesnick, R. S., et al. "Observations of the inner radiation belt: CRAND and trapped solar protons." *Journal of Geophysical Research: Space Physics* 119.8 (2014): 6541-6552.

Shprits, Yuri Y., et al. "Review of modeling of losses and sources of relativistic electrons in the outer radiation belt II: Local acceleration and loss." *Journal of atmospheric and solar-terrestrial physics* 70.14 (2008): 1694-1713.

Smirnov, A., Shprits, Y. Y., Allison, H., Aseev, N., Drozdov, A., Kollmann, P., ... & Saikin, A. (2022). An empirical model of the equatorial electron pitch angle distributions in Earth's outer radiation belt. *Space Weather*, *20*(9), e2022SW003053.

Smith, Howard Todd, et al. "Europa neutral torus confirmation and characterization based on observations and modeling." *The Astrophysical Journal* 871.1 (2019): 69.

Smyth, William H., and Max L. Marconi. "Europa's atmosphere, gas tori, and magnetospheric implications." *Icarus* 181.2 (2006): 510-526.

Speiser, T. W. "Particle trajectories in model current sheets: 1. Analytical solutions." *Journal of Geophysical Research* 70.17 (1965): 4219-4226.

Starr, R. D., Schriver, D., Nittler, L. R., Weider, S. Z., Byrne, P. K., Ho, G. C., ... & Trávníček, P. M. (2012). MESSENGER detection of electron-induced X-ray fluorescence from Mercury's surface. *Journal of Geophysical Research: Planets*, *117*(E12).

Sulaiman, A. H., Hospodarsky, G. B., Elliott, S. S., Kurth, W. S., Gurnett, D. A., Imai, M., ... & Bolton, S. J. (2020). Wave-particle interactions associated with Io's auroral footprint: Evidence of Alfvén, ion cyclotron, and whistler modes. *Geophysical Research Letters*, *47*(22), e2020GL088432.

Sun, Y. X., Roussos, E., Krupp, N., Zong, Q. G., Kollmann, P., & Zhou, X. Z. (2019). Spectral signatures of adiabatic electron acceleration at Saturn through corotation drift cancelation. *Geophysical Research Letters*, *46*(17-18), 10240-10249.

Summers, Danny, Richard M. Thorne, and Fuliang Xiao. "Relativistic theory of wave-particle resonant diffusion with application to electron acceleration in the magnetosphere." *Journal of Geophysical Research: Space Physics* 103.A9 (1998): 20487-20500.

Szalay, J. R., Bonfond, B., Allegrini, F., Bagenal, F., Bolton, S., Clark, G., ... & Wilson, R. J. (2018). In situ observations connected to the Io footprint tail aurora. *Journal of Geophysical Research: Planets*, *123*(11), 3061-3077.

Thorne, RM ea, et al. "Rapid local acceleration of relativistic radiation-belt electrons by magnetospheric chorus." *Nature*504.7480 (2013): 411-414.

Tsuchiya, F., Misawa, H., Imai, K., & Morioka, A. (2011). Short-term changes in Jupiter's synchrotron radiation at 325 MHz: Enhanced radial diffusion in Jupiter's radiation belt driven by solar UV/EUV heating. *Journal of Geophysical Research: Space Physics*, *116*(A9).

Turner et al., Cross-scale physics and the acceleration of particles in collisionless plasmas throughout the Heliosphere and beyond: III. Radiation belts, White Paper submitted to the 2023 Solar and Space Physics Decadal Survey

Turner, Drew L., et al. "Characteristics of energetic electrons near active magnetotail reconnection sites: Tracers of a complex magnetic topology and evidence of localized acceleration." *Geophysical Research Letters* 48.2 (2021): e2020GL090089.

Ukhorskiy, A. Y., et al. "Rotationally driven 'zebra stripes' in Earth's inner radiation belt." *Nature* 507.7492 (2014): 338-340

Van Allen, J. A., et al. "Energetic electrons in the magnetosphere of Jupiter." *Science* 183.4122 (1974): 309-311.

Vasyliunas, V. M. (1983). Physics of the Jovian magnetosphere. 11. Plasma distribution and flow. *Physics of the Jovian magnetosphere*, 395-453.

Vogt, M. F., Kivelson, M. G., Khurana, K. K., Joy, S. P., & Walker, R. J. (2010). Reconnection and flows in the Jovian magnetotail as inferred from magnetometer observations. *Journal of Geophysical Research: Space Physics*, *115*(A6).

Vogt, Marissa F., et al. "Magnetotail reconnection at Jupiter: A survey of Juno magnetic field observations." *Journal of Geophysical Research: Space Physics* 125.3 (2020): e2019JA027486.

Wonders, M. A., Johnsen, A. M., Davison, C. C., Cheng, S., Chichester, D. L., & Flaska, M. (2018, November). Assessment of Modern Silicon Photomultiplier Radiation Hardness in a Nuclear Security Context. In *2018 IEEE Nuclear Science Symposium and Medical Imaging Conference Proceedings (NSS/MIC)* (pp. 1-8). IEEE.

Woodfield, Emma E., et al. "The origin of Jupiter's outer radiation belt." *Journal of Geophysical Research: Space Physics* 119.5 (2014): 3490-3502.

Wu, X., Ambrosi, G., Azzarello, P., Bergmann, B., Bertucci, B., Cadoux, F., ... & Tykhonov, A. (2019). Penetrating particle ANalyzer (PAN). *Advances in Space Research*, *63*(8), 2672-2682.

Young, S. L. , R. E. Denton , B. J. Anderson , and M. K. Hudson (2008), Magnetic field line curvature induced pitch angle diffusion in the inner magnetosphere , *J. Geophys. Res.* , **113** , A03210 , doi:10.1029/2006JA012133 .